

UNIVERSITÀ DEGLI STUDI DI PADOVA

Dipartimento di Fisica e Astronomia "Galileo Galilei"

Master Degree in Astrophysics and Cosmology

Final dissertation

Characterisation of a new Laser Guide Star

Wavefront Sensor

Thesis supervisor

Prof. Roberto Ragazzoni

Thesis co-supervisor

Dr. Kalyan Kumar Radhakrishnan Santhakumari

Dr. Simone Di Filippo

Candidate

Tânia Sofia Gomes Machado

Academic Year 2022/23

Às pêras que ficaram nas árvores por apanhar

Às memórias que ficaram por criar

A ti, avô

Acknowledgments

First and foremost, I extend my heartfelt gratitude to my co-supervisors, Simone and Kalyan, for their unwavering support and availability over the past six months. Your guidance, advice, and encouragement are what many master's students can only dream of, and for that, I am immensely thankful. A thank you is also due to my supervisor Prof. Roberto Ragazzoni for in a few quick meetings providing me with ideas to solve problems that had been bothering me for two months.

This thesis marks not only the culmination of a two-year master's degree at the University of Padova but also the end of a six-year journey that began at Lancaster University and continued at Instituto Superior Técnico (IST), where I earned my bachelor's degree in Engineering Physics. I didn't have the opportunity to write a thesis during those earlier years, and so this thesis is dedicated to all the people who supported me relentlessly.

I owe my gratitude to David Sobral for providing me with my first opportunity to engage in real astronomy research. Christopher Harrison, Jöel Vernet, and Anita Zanella followed suit, exponentially fueling my interest in Astronomy. If Anita is not already aware, I would like to remind her that she was an inspiration that led me to Padova. At the end of this incredible journey, a heartfelt thank you is certainly in order.

Throughout this work, I was warmly embraced by the Adaptive Optics group at the INAF-Osservatorio Astronomico di Padova. Your strong sense of community and vibrant spirit motivated me to give my best every day.

Special thanks are due to Davide Greggio for his valuable suggestions and insights during numerous Ingot meetings, and to Carmelo Arcidiacono for reviewing sections of this thesis and offering suggestions for improvement.

I want to extend my deepest appreciation to the friends who walked this journey with me: my fellow "Insetes Maldites probably Australianos" (you know who you are, Patos), Rita Silva, Diogo Ribeiro, Beatriz Silva, Inês Moreira, Patrícia Curado. To the Physics student club (NFIST) and the Astronomy Section (ASTRO) at IST: we laughed, we cried, we shouted, and it was all worth it. A special note of gratitude goes to my trainer and friend, Filipa Velloso, for providing the much-needed hours free of concerns, and on that same page, to all the horses that accompanied me during those hours. Finally, to all my friends in Padova who never once made me doubt my decision to move out from my home again.

However, the last sentence doesn't entirely hold true, as there remain some individuals I am yet to thank that actively change its veracity. My family in Portugal - grandparents, uncles and cousins - both on the one hand causing me to question the path that took me far from them, and on the other hand, providing me with the strength to persevere. Lastly, my core support system: Mom, Dad, Diogo, and Carolina. I love you all deeply.

Resumo

A Ótica Adaptativa (OA) é uma tecnologia que aprimora a resolução de telescópios, corrigindo as aberrações introduzidas pela atmosfera terrestre e permitindo a obtenção de imagens astronômicas mais nítidas. A técnica de OA tradicional tira partido de estrelas brilhantes próximas do objeto em estudo, para serem usadas como referência. Isto restringe o uso de correções com OA a áreas específicas e reduzidas do céu. Para contornar esta limitação, o conceito de Laser Guide Stars (LGS), das quais as LGS de Sódio são um exemplo, foi criado. Estas estrelas artificiais são criadas com lasers disparados na proximidade do telescópio e estendem-se no céu, ao longo da extensão da camada de sódio da atmosfera. A natureza alongada das LGS de Sódio apresenta desafios para os sensores de frente de onda já existentes e frequentemente usados em sistemas com OA.

A nossa pesquisa está centrada no Sensor de Frente de Onda Ingot, um conceito inovador inicialmente proposto por Ragazzoni e aperfeiçoado pelo grupo de OA do INAF-Osservatorio Astronomico di Padova. O sensor Ingot foi projetado para enfrentar os desafios apresentados pelas LGS de Sódio e outras estrelas guia laser. O conceito baseia-se no princípio de Scheimpflug para capturar uma imagem totalmente focada da LGS alongada ao longo de toda a sua extensão. Este sensor inovador é adequado para uso em grandes telescópios. Atualmente está projetado para atender às especificações do European Extremely Large Telescope (E-ELT).

O meu trabalho incluiu o desenvolvimento de algoritmos avançados para manipular a simulação da LGS num ecrã OLED, aprimorar procedimentos de alinhamento e corrigir erros sistemáticos. Além disso, implementámos um algoritmo *Quasi Closed-Loop* para monitorização e realinhamento autónomo do sensor. Testes ainda em curso envolvem o desenvolvimento de um algoritmo de busca e a integração de perfis de sódio reais usando um novo ecrã OLED. O nosso objetivo final é obter uma compreensão mais abrangente do desempenho do sensor Ingot e as suas potenciais aplicações em futuros telescópios extremamente grandes equipados com OA.

Palavras-chave:

Ótica Adaptativa; Sensor de Frente de Onda; Astronomia; Instrumentação; Estrelas Guia Laser de Sódio; Extremely Large Telescopes

Abstract

Adaptive Optics (AO) is a technology that improves the resolution of large telescopes by correcting aberrations introduced by the Earth's atmosphere, enabling them to capture sharper astronomical images. Traditional AO relies on bright natural stars close to the science target for reference, limiting its use to specific areas of the sky. To overcome this limitation, scientists introduced the concept of Laser Guide Stars (LGS), such as sodium LGS. These artificial stars are created using lasers fired from the telescope position to excite the atomic sodium atmospheric layer, creating an elongated source in the sky. This unique nature of sodium LGS presented challenges for existing wavefront sensors used in AO systems.

This thesis focuses on the Ingot Wavefront Sensor (I-WFS), a novel concept initially proposed by Ragazzoni and refined by the Adaptive Optics Group at the INAF-Osservatorio Astronomico di Padova. The I-WFS is designed to address the challenges posed by Sodium LGS and other LGS. It leverages the Scheimpflug principle to sense the full 3D volume of the elongated LGS. This innovative sensor is suitable for use in large telescopes. Currently it is designed to match the specifications of the European Extremely Large Telescope (E-ELT).

My work has included the development of advanced algorithms for manipulating the LGS source on a screen, improving alignment procedures, and correcting systematic errors. I have also implemented a quasi closed-loop algorithm for autonomous monitoring and realignment. Ongoing research includes the development of a search algorithm and the integration of real sodium profiles using a new OLED screen. Our ultimate goal is to gain a comprehensive understanding of the I-WFS's performance and its potential implementation in future Extremely Large Telescopes (ELTs) equipped with AO.

Keywords: Adaptive Optics ; Wavefront Sensor ; Astronomy; Instrumentation; Sodium Laser Guide Stars; Extremely Large Telescopes

Contents

| | |
|---------------------------------------------------------------------------|-----------|
| Acknowledgments | iii |
| Resumo | v |
| Abstract | vii |
| List of Tables | xi |
| List of Figures | xiii |
| Glossary | xxiii |
| 1 Introduction | 1 |
| 1.1 The Development of Ground-based Telescopes | 1 |
| 1.2 Adaptive Optics: a solution with limitations | 2 |
| 1.3 Laser Guide Stars | 3 |
| 1.4 Goals of this work | 4 |
| 1.5 Thesis Outline | 4 |
| 2 Atmospheric Turbulence | 7 |
| 2.1 Diffraction Limit: in the Absence of Atmospheric Turbulence | 7 |
| 2.2 Observing through the Atmosphere | 9 |
| 2.3 Kolmogorov Theory of Turbulence | 10 |
| 2.4 Seeing Parameters | 13 |
| 2.5 How can Adaptive Optics be helpful? | 15 |
| 3 Adaptive Optics | 19 |
| 3.0.1 Reference Star | 20 |
| 3.0.2 Wavefront Sensor | 21 |
| 3.0.3 Real Time Computer: Wavefront Reconstruction | 24 |
| 3.0.4 Wavefront Corrector | 25 |
| 3.1 Adaptive Optics Limitations | 26 |
| 3.1.1 Laser Guide Stars | 28 |
| 3.1.2 Multi-Conjugate Adaptive Optics | 32 |
| 3.2 Ingot WFS: a Novel Concept for Elongated LGS | 32 |
| 4 Adaptive Optics at the European Extremely Large Telescope | 41 |
| 4.1 E-ELT: Project Description | 41 |
| 4.2 Adaptive Optics Modes and Systems | 43 |
| 4.3 Wavefront Sensors for the E-ELT | 47 |
| 4.4 Science Cases aided by LGS AO systems | 48 |
| 4.4.1 Star Forming Clumps in High-Redshift Galaxies | 50 |
| 5 Laboratory Testing of Ingot Wavefront Sensor | 55 |

| | | |
|----------|-------------------------------------------------------------|------------|
| 5.1 | Experimental Set-up: Test Bench | 55 |
| 5.2 | OLED Screen: Simulating the LGS | 61 |
| 5.2.1 | Trial Alignments | 64 |
| 5.3 | New Alignment Procedure | 74 |
| 5.3.1 | Continuation: Robustness of the Alignment | 80 |
| 5.4 | Quasi Closed-Loop Situation: Control Loop | 87 |
| 5.5 | Search Algorithm | 90 |
| 5.5.1 | First step: from Zero to One Illuminated Pupil | 91 |
| 5.5.2 | Second step: from One to Three Illuminated Pupils | 92 |
| 5.5.3 | Insights for Prototyping | 96 |
| 5.6 | New OLED Screen | 96 |
| 5.7 | Future Work | 98 |
| 6 | Conclusions | 101 |
| A | Sodium Layer Profiles | 111 |

List of Tables

| | | |
|-----|-------------------------------------------------------------------------------------------------------------------------------------------------------------------------------------------------------------------------------------------------------------------------------------------------------------------------------------------------------------------------------------------------------------|----|
| 4.1 | Comparison of expected/simulated AO performances for the first generation E-ELT instruments across their AO modes: MCAO, SCAO, LTAO or no AO mode NOAO. The values of SR correspond to the peak performance under median seeing and wind conditions for the specified magnitude and wavelength band. The SC is about the diffraction-limit, for SCAO, and for the mentioned SR ratios, for the other modes. | 46 |
| 5.1 | Target values of each of the six observables, measured with the pupil data, that define the aligned position of the I-WFS. | 60 |
| 5.2 | Parameters a and b obtained from the linear fits of the current section, together with the standard deviation σ of the fit. The values of these parameters before and after the OLED screen was covered with tape are displayed side by side for easier comparison. | 74 |
| 5.3 | Parameters μ and σ obtained from the gaussian fits of histograms in Figures 5.23. The limits defined to rule out outliers are specified, together with the new parameters μ_{new} and σ_{new} obtained from the gaussian fits of histograms in Figures 5.24. The final boundaries of each observable that define the aligned range are here also specified. | 78 |
| 5.4 | The best fit parameters resultant from the plots of Figures 5.27, 5.28, 5.29 (for vertical movements) and Figures 5.30, 5.31, 5.32 (for horizontal movements) are displayed. | 86 |

List of Figures

| | | |
|-----|---------------------------------------------------------------------------------------------------------------------------------------------------------------------------------------------------------------------------------------------------------------------------------------------------------------------------------------------------------------------------------------------------------------------------------------------------------------------------------------------------------------------------------------------------------------------------------------------------------------------------------------------------------------------------------------------------------------------------------------------------|----|
| 2.1 | The resolution of astronomical images depends on the turbulence encountered by the flat wavefronts as they cross the atmosphere. Left: In the absence of turbulence, the wavefronts arrive still flattened at the telescope aperture. This situation forms diffraction limited images with a characteristic Airy pattern of resolution λ/D . Right: In the presence of atmosphere, the flat wavefronts are perturbed by turbulent cells of average size r_0 . D/r_0 Speckles of size λ/D are seen on short exposures ($t < t_0$). In long exposures the speckle pattern gets blurred over an area of λ/r_0 . This blurred image is said to be seeing limited. Image adapted from Parenti [1]. | 8 |
| 2.2 | The atmosphere's transparency varies as a function of the wavelength. To some wavelength ranges it is completely opaque such as the shorter UV limit ($\lambda < 0.3 \mu\text{m}$), the microwave range and radio. Instead, complete transparency takes place in the optical and shorter wavelength radio window (1cm-10m). Absorption in the IR is characterised by a series of shorter transparent windows and large absorption bands. Image adapted from Hardy [2]. | 9 |
| 2.3 | Kolmogorov's theory of turbulence describes the energy cascade of turbulent eddies since energy is injected in the atmosphere at the outer scales until it dissipates into heat by viscous friction. The one-dimensional energy spectrum, valid for eddies within the inertial sub range ($l < l_k < L$) follows the law $\log(E_k) = -\frac{5}{3} \log(k)$, $k = 2\pi/l$. Image taken from Wikipedia | 12 |
| 2.4 | The $C_N^2(h)$ profile as a function of height h is plotted, measured with a SCIDAR at Mt. Graham which is at a height of 3.3 km above mean sea level. The profile is plotted with the height h above the telescope along the y-axis, and the strength of the turbulence along the x-axis in logarithmic scale. The surface layer, which consists of the first few metres above the telescope where the atmosphere is the most turbulent, shows a maximum of C_N^2 . Another weak layer is seen at $h \sim 3$ km. At $h \sim 9$ km, so altitude of 12 km above sea level, there is weak but extended peak of C_N^2 . Image from Sebastian Egner's PhD thesis [3]. | 13 |
| 2.5 | As flat wavefronts cross the atmosphere and encounter turbulent cells of different sizes, they get perturbed. The deformations caused can be decomposed in two components: the mean wavefront tip-tilt and higher order aberrations. Image from Maria Bergomi's PhD thesis [4]. | 16 |
| 2.6 | The difference in image resolution with and without AO corrections is shown in a plot of the image angular diameter as a function of wavelength (μm). Across all wavelengths, AO has the ability to reduce the seeing of seeing limited images and reach resolutions closer to the diffraction limit. However higher wavelengths are not so greatly affected by seeing such that even uncompensated telescopes are close to the diffraction Limit. Hence, at shorter wavelengths, where seeing largely decreases the resolution, the potential usefulness of AO systems is higher. Image adapted from Hardy [2]. | 17 |

| | | |
|-----|----------------------------------------------------------------------------------------------------------------------------------------------------------------------------------------------------------------------------------------------------------------------------------------------------------------------------------------------------------------------------------------------------------------------------------------------------------------------------------------------------------------------------------------------------------------------------------------------------------------------------------------------------------------------------------------------------|----|
| 3.1 | The components of an AO System are shown, in a closed-loop configuration. As distorted wavefronts enter the telescope optics, they encounter the deformable mirror (DM), which corrects the wavefronts. Then, part of the light is diverted towards the wavefront sensor (WFS) to measure the residual aberrations, while the rest continues to the science camera. The WFS senses the wavefronts and sends the information to the real-time computer (RTC) who computes the necessary adjustments to be sent to the DM. Image from Sebastian Egner's PhD thesis [3]. | 20 |
| 3.2 | The quad-cell concept is illustrated. The image spot is focused onto a four quadrant detector, that splits the light into four signals A,B,C,D. proportional to the area of the spot covering each quadrant. Then, using Equations 3.1 the shifts along the x and y axis are computed and the local tip-tilt is retrieved. Image from Maria Bergomi's PhD thesis | 22 |
| 3.3 | The Shack-Hartmann WFS concept is illustrated. A lenslet array is placed on the pupil plane to sample the incoming wavefront. From each subaperture thus created, an image spot is focused onto a detector on the focal plane. Using the quad-cell concept the mean tip-tilt is retrieved to reconstruct higher order aberrations. Image from Valentina Viotto's Phd Thesis [5]. | 23 |
| 3.4 | The Pyramid WFS concept is illustrated. The tip of the pyramid is placed on the focal plane, where the light of the guide star is focused. The four faces split the light into four beams which are imaged onto a detector placed on the pupil plane by a relay lens. The light distribution across the four pupil images is used to calculate both the tip-tilt and the higher order aberrations, if the operations are performed pixel wise. Image taken from Sebastian Egner's PhD thesis [3]. | 23 |
| 3.5 | The wavefront reconstruction process is described, using the zonal mode. The WFS measures the local tip-tilt in smaller apertures, dividing the original wavefront. In this process, the relative phases between contiguous zones is lost. These are retrieved to obtain a continuous reconstructed wave profile. Then, the RTC computes the voltages that the DM actuators must have to correct for this wavefront profile. Image adapted from Hardy [2]. | 24 |
| 3.6 | Left: Image shows the anisoplanatism effect leading to a degradation of the correction, in a SCAO system. The turbulence sensed by the WFS doesn't match the turbulence corrected by the DM. The highest SR is achieved inside the θ_0 , close to the reference star. The further away from it the worse is the SR. Right: Image shows another degrading effect: the so-called cone effect or focal anisoplanatism. It takes place, again, due to a mismatch between the volume of atmosphere sensed with the LGS and the volume corrected for the science target. The lower the altitude of the LGS, the bigger is the impact of this effect. Images taken from ESO. | 27 |
| 3.7 | An object with an extended nature will result in an image only partially in focus on a plane orthogonal to the chief ray. Right: Only the central part of the source will be actually in focus while its edges will be defocused. Left: There is a plane where the light coming from different pots of laser beacon can be equally in focus. Image taken from Simone Di Filippo's PhD thesis [6]. | 30 |
| 3.8 | The LGS spots appear elongated in subapertures far from the Laser Launcher Telescopes (LLT). For a LLT on the edge of the telescope's aperture, at positionn (x_l, y_l) , the elongation ϵ at a subaperture (x_r, y_r) is given by Equation 3.10. It depends on r , ΔH , H and $\cos(\xi)$, respectively the distance from the subaperture to the LLT, the width and height of the LGS on sky, and ξ the zenith angle. Image taken from Lombini et al. 2021 [7]. | 31 |

| | | |
|------|-------------------------------------------------------------------------------------------------------------------------------------------------------------------------------------------------------------------------------------------------------------------------------------------------------------------------------------------------------------------------------------------------------------------------------------------------------------------------------------------------------------------------------------------------------------------------------------------------------------------------------------------------------------------------------------------------------------------------------------------------------------------------------------------------------------------------------------------------|----|
| 3.9 | A sodium LGS elongated imaged as seen from the Jacobus Kapteyn Telescope. Image taken from Isaac Newton Group of Telescopes. | 33 |
| 3.10 | Left: An image composed of points f to i tilted with respect to the optical system's aperture, will come into focus at different parallel planes behind the aperture. Each point at distance d from the aperture focuses in a plane at a distance d' after the aperture. Right: An image composed of points f to i is position along a plane tilted by θ with respect to the optical system's aperture. According to Scheimpflug, there is a conjugate plane tilted by ϕ with respect to the aperture plane, where the image plane spots $f-i$ can be in focus simultaneously, at positions $f'-i'$. This is called the optimal focal plane. The distances of the image points and focus points to the centre of the aperture are d and d' respectively. The three planes intersect at s | 34 |
| 3.11 | The initial design of the I-WFS consisted of a six-faced prism. This prism is placed on the best focal plane, behind the telescope aperture, where its six faces are illuminated by the LGS image, originating six pupils. Different sized prisms must be used to match the Na layer size variation so that enough light hits each surface and all the signals can be retrieved from the six pupils. Image taken from Simone Di Filippo PhD's thesis [6]. | 35 |
| 3.12 | Schematic representation of the ingot solid shape and the parameters used to describe its geometry [8]. $\alpha = 83.63^\circ$, $\beta = 28^\circ$, $W_{ingot} = 10\text{mm}$, $L_{ingot} = 110\text{mm}$ | 35 |
| 3.13 | Conceptual layout of the ingot prism. Part of the LGS is focused by the reflecting ingot roof and forms two pupils, B and C (left), while the remaining part of the LGS is focused after the ingot (right) and is transmitted directly to the pupil re-imaging optics forming the third pupil. | 36 |
| 3.14 | Scheimpflug's principle applied for different configurations of a telescope's optics, for a LLT perpendicular to the entrance pupil ($\theta = 90^\circ$). Illustrative schemes of how the LGS's light cones are intercepted by a I-WFS placed on the optical focal plane, as the LLT position changes with respect to the telescope's entrance pupil Left: LLT on the centre of the entrance pupil. Centre: LLT on the edge of the entrance pupil. Right: LLT outside the entrance pupil. A Sodium LGS is represented by its edges as points f and i , with respective focused image points f' and i' . Only when the LLT is positioned just outside the entrance pupil the I-WFS can be used properly, as the light cones of the LGS are no longer embedded onto each other. | 37 |
| 3.15 | The Scheimpflug principle applied for the optical layout of the E-ELT, with the LLT placed outside the telescope's entrance pupil at a distance 21.5 m from its centre. A Sodium LGS is represented by its edges as points f and i , with respective focused image points f' and i' . The LGS image is tilted with respect to a focal plane perpendicular to the optical axis by angle $\phi = 83.67^\circ$. The light cones of the final and initial points of the LGS are shown, as they are focused onto a I-WFS placed on the optimal focal plane. In reality, the I-WFS is tilted by $\omega = 0.3^\circ$ from the optimal plane. | 38 |
| 3.16 | The Scheimpflug principle applied for the optical layout of the E-ELT, with the LLT placed outside the telescope's entrance pupil at a distance 21.5 m from its centre. A Sodium LGS is represented by its edges as points f and i , with respective focused image points f' and i' . The LGS image is tilted with respect to a focal plane perpendicular to the optical axis by angle $\phi = 83.67^\circ$. The distances s and s' of the image and focus points from the optical axis, and the distances h and h' from the entrance pupil are drawn. Additionally, the distances d and d' from the centre of the pupil are represented. | 39 |

| | | |
|-----|------------------------------------------------------------------------------------------------------------------------------------------------------------------------------------------------------------------------------------------------------------------------------------------------------------------------------------------------------------------------------------------------------------------------------------------------------------------------------------------------------------------------------------------------------------------------------------------------------------------------------------------------------------------------------------------------------------------------------------------|----|
| 4.1 | This diagram shows the novel 5-mirror optical system of ESO's E-ELT. Light is collected by the primary mirror M1 and before reaching the science instruments the light it is reflected by four other mirrors, M2, M3, M4 and M5. The final two mirrors (M4 and M5) form the built-in AO system. Image taken from ESO. | 42 |
| 4.2 | LTAO principle is illustrated. Taking advantage of more than one LGS on the FoV, the data from the WFS can be used by the RTC to reconstruct tomographically the atmospheric turbulence layer by layer. The cone effect can be controlled with this technique. Only one DM is used to apply AO corrections. Image from ESO. | 44 |
| 4.3 | High-redshift $z = 2.2405$ galaxy ZC400569 imaged with current cutting edge instruments. Left: Space based observations (HST) [9] Middle: Ground based observations without AO corrections (SINFONI at VLT) [9] Right: Ground based observations with AO corrections (SINFONI at VLT). Respectively, these observations reached spatial resolutions of 1 kpc, 5 kpc and 2 kpc. Circles on the left bottom side of each image indicate the size of the PSF. Set of images from Mancini et al. 2011 [9] and Forster-Schreiber et al. 2018 [10]. | 51 |
| 4.4 | SNR maps of a model clumpy galaxy $z = 2.07$ for varying SFRs observed at 20×20 mas (top row) and 10×10 mas (bottom row). SFR increases from left to right and is denoted in the top left of each panel. The size of the LTAO PSF is shown in the bottom left of the each map in the top row. The total exposure time is 10 h. The three star-forming clumps detected are highlighted with yellow-dashed circles in the central panel of the top row. For comparison, we also show the input morphology (10 mas sampling) in the right-hand subplot. Image from Zieleniewski et al. 2015 [11]. | 52 |
| 4.5 | Left: Map of $\log[NII]/H\alpha$ emission line ratio of a kinematic component of the SDSSJ165202.64+172852.3 $z = 2.94$ galaxy associated with high star formation rates. White ellipse in the lower left corner shows the size of the Near-Infrared Spectrograph Integral Field Unit PSF. White circle on the top left highlights the region where star forming clumps of size ~ 1 kpc were detected. Individual clumps couldn't be resolved. Right: Extinction corrected $H\alpha$ derived star formation rate $SFR(H\alpha)$ map in the same galaxy. Black circle on the top left highlights the region where star forming clumps of size ~ 1 kpc were detected. Images from Vayner et al. 2023 [12]. | 53 |
| 4.6 | Histograms showing the distribution of values of the PSF FWHM of the observations of 35 star-forming galaxies. The AO modes varied between NGS and LGS. In general, the mean of the distribution of NGS and LGS FWHM is very similar. It is important to highlight that LGS allowed the galaxy sample to duplicate in size. | 54 |
| 5.1 | Top view of the optical bench setup used to test the ingot alignment procedure. Detailed images of the OLED Screen (seen face on and from the pupil) and of the Ingot (seen face on and from the pupil). | 56 |
| 5.2 | Left: Detector image of the three pupils' illumination on an aligned configuration, with the reference axis x and y depicted. Right: Identification of the A, B and C pupils and the three observables related to pixel distances: distance $A - B$, distance $A - C$ and vertical distance $Y_B - Y_C$. Images adapted from Kalyan et al. 2020 [13]. | 58 |
| 5.3 | Signals S_x and S_y are calculated from the pupils using Equations 3.11 and are here displayed, for an aligned configuration. From the S_x signals, the observable $\overline{S_{x1}} - \overline{S_{x2}}$ is obtained using the two regions identified here. Moreover, the non uniform pattern of these signals is evident. Images adapted from Kalyan et al. 2020 [13]. | 58 |

| | | |
|------|-------------------------------------------------------------------------------------------------------------------------------------------------------------------------------------------------------------------------------------------------------------------------------------------------------------------------------------------------------------------------------------------------------------------------------------------------------------------------------------------------------------------------------------------------------------------------------------------------------------------|----|
| 5.4 | The ingot prism is held by a 3D printed structure, placed on an hexapod stage with 6 degrees of freedom. The coordinate axis (x, y, z) used to measure the positions of the hexapod throughout the rest of this thesis are depicted, with the origin defined internally on the hexapod program. The orientation of the three pupils of the image formed on the camera is clarified (the re-imaging optics is omitted for clearance). | 59 |
| 5.5 | Schematic representation of the SSD1306 bitmap. It is a matrix of 16×64 entries, to illuminate the 128×64 pixels of the screen. Each entry consists of a hexadecimal number that controls the illumination of each group of eight adjacent pixels. | 61 |
| 5.6 | Each entry of the screen's bitmap is a hexadecimal number that controls the illumination of each group of eight adjacent pixels. To individually light up each of the 8 pixels, a byte 00000000 with its 8 bits representing the 8 pixels from left to right needs to be converted to hexadecimal value as illustrated here. The example of 8 pixels illuminated as 10001110 results in the entry 0x8E. | 62 |
| 5.7 | Representation of the settings required to define a LGS source on the OLED Screen. Top: Start with defining the vertical shift VS and horizontal shift HS of the centre of the LGS with respect to the centre of the screen. Bottom: Choose the length in columns to be added to the left LE and right LR, the thickness in rows to be added to the top TU and bottom TD and the number of vertical discontinuities $\#D$ to be added across the length of the LGS. | 63 |
| 5.8 | Plot depicts the progression of the Z position of the hexapod/ingot during the alignment process when different sources are placed on the screen. The y-axis represents the position on the Z axis of the hexapod, in mm, while the x-axis displays the iteration when that position was achieved. Each colour represents a source with different values of VS: positive VS are shown with continuous lines and triangular scatter points, while negative VS are represented with dashed lines and circular scatter points. The final position of the standard source $Z_{standard}$ ($VS = 0$) is highlighted. | 65 |
| 5.9 | The data from Figure 5.8 is used. The x-axis displays the VS of the LGS source. The y-axis represents the Z axis position of the hexapod, in mm, at the end of the alignment with each source, relative to $Z_{standard}$. Top: Linear fit performed to the data with best fit parameters $a = -0.172\text{mm}$ and $b = -0.012\text{mm}$. Bottom: The residuals of the fit have a standard deviation of $\sigma = 0.018\text{mm}$. | 65 |
| 5.10 | Plot depicts the progression of the Y position of the hexapod/ingot during the alignment process when different sources are placed on the screen. The y-axis represents the position on the Y axis of the hexapod, in mm, while the x-axis displays the iteration when that position was achieved. Each colour represents a source with different values of VS: positive VS are shown with continuous lines and triangular scatter points, while negative VS are represented with dashed lines and circular scatter points. The final position of the standard source $Y_{standard}$ ($VS = 0$) is highlighted. | 66 |
| 5.11 | The data from Figure 5.10 is used. The x-axis displays the VS of the LGS source. The y-axis represents the Y axis position of the hexapod, in mm, at the end of the alignment with each source, relative to $Y_{standard}$. Top: Linear fit performed to the data with best fit parameters $a = -0.509\text{ mm}$ and $b = -1.943\text{ mm}$. Bottom: The residuals of the fit have a standard deviation of $\sigma = 1.457\text{ mm}$. | 67 |

| | | |
|------|---------------------------------------------------------------------------------------------------------------------------------------------------------------------------------------------------------------------------------------------------------------------------------------------------------------------------------------------------------------------------------------------------------------------------------------------------------------------------------------------------------------------------------------------------------------------------------------------------------------------------|----|
| 5.12 | Plot depicts the progression of the X position of the hexapod/ingot during the alignment process when different sources are placed on the screen. The y-axis represents the position on the X axis of the hexapod, in mm, while the x-axis displays the iteration when that position was achieved. Each colour represents a source with different values of VS: positive VS are shown with continuous lines and triangular scatter points, while negative VS are represented with dashed lines and circular scatter points. The final position of the standard source $X_{standard}$ ($VS = 0$) is highlighted. | 68 |
| 5.13 | The data from Figure 5.12 is used. The x-axis displays the VS of the LGS source. The y-axis represents the X axis position of the hexapod, in mm, at the end of the alignment with each source, relative to $X_{standard}$. Top: Linear fit performed to the data with best fit parameters $a = -0.030$ mm and $b = -0.060$ mm. Bottom: The residuals of the fit have a standard deviation of $\sigma = 0.049$ mm. | 68 |
| 5.14 | Left: OLED screen side as seen from the pupil. The side of the screen is covered with a black material in a non uniform way. Different rows of the screen reveal different side profiles, as highlighted by the red boxes. Right: A black non-reflective tape was applied to cover most of the screen's side. Different rows of the screen now reveal similar and very thin side profiles, as highlighted by the red boxes. Arrows indicate the front face of the screen. | 69 |
| 5.15 | Plot depicts the progression of the Z position of the hexapod/ingot during the alignment process when different sources are placed on the screen. The y-axis represents the position on the Z axis of the hexapod, in mm, while the x-axis displays the iteration when that position was achieved. Each colour represents a source with different values of VS: positive VS are shown with continuous lines and triangular scatter points, while negative VS are represented with dashed lines and circular scatter points. The final position of the standard source $Z_{standard}$ ($VS = 0$) is highlighted. | 70 |
| 5.16 | The data from Figure 5.15 is used. The x-axis displays the VS of the LGS source. The y-axis represents the Z axis position of the hexapod, in mm, at the end of the alignment with each source, relative to $Z_{standard}$. Top: Linear fit performed to the data with best fit parameters $a = -0.176$ mm and $b = 0.571$ mm. Bottom: The residuals of the fit have a standard deviation of $\sigma = 0.043$ mm. | 70 |
| 5.17 | Plot depicts the progression of the Y position of the hexapod/ingot during the alignment process when different sources are placed on the screen. The y-axis represents the position on the Y axis of the hexapod, in mm, while the x-axis displays the iteration when that position was achieved. Each colour represents a source with different values of VS: positive VS are shown with continuous lines and triangular scatter points, while negative VS are represented with dashed lines and circular scatter points. The final position of the standard source $Y_{standard}$ ($VS = 0$) is highlighted. | 71 |
| 5.18 | The data from Figure 5.17 is used. The x-axis displays the VS of the LGS source. The y-axis represents the Y axis position of the hexapod, in mm, at the end of the alignment with each source, relative to $Y_{standard}$. Top: Linear fit performed to the data with best fit parameters $a = 0.028$ mm and $b = -0.339$ mm. Bottom: The residuals of the fit have a standard deviation of $\sigma = 0.314$ mm. | 71 |

| | | |
|------|--------------------------------------------------------------------------------------------------------------------------------------------------------------------------------------------------------------------------------------------------------------------------------------------------------------------------------------------------------------------------------------------------------------------------------------------------------------------------------------------------------------------------------------------------------------------------------------------------------------------------------------------------------------------------------------------------------------------------------------------------------------------------------------------|----|
| 5.19 | Plot depicts the progression of the X position of the hexapod/ingot during the alignment process when different sources are placed on the screen. The y-axis represents the position on the X axis of the hexapod in millimetres, while the x-axis displays the iteration when that position was achieved. Each colour represents a source with different values of VS: positive VS are shown with continuous lines and triangular scatter points, while negative VS are represented with dashed lines and circular scatter points. The final position of the standard source ($VS = 0$) is highlighted. | 72 |
| 5.20 | The data from Figure 5.19 is used. The x-axis displays the VS of the LGS source. The y-axis represents the X axis position of the hexapod, in mm, at the end of the alignment with each source, relative to $X_{standard}$. Top: Linear fit performed to the data with best fit parameters $a = 0.005$ mm and $b = -0.042$ mm. Bottom: The residuals of the fit have a standard deviation of $\sigma = 0.022$ mm. | 73 |
| 5.21 | Steps of the alignment performed with a "for" loop are detailed. | 75 |
| 5.22 | Steps of the alignment performed with a "while" loop are detailed. | 76 |
| 5.23 | The final values of the observables obtained at the end of each of the 194 alignments (with "for" loop, $I_{max} = 10$) are displayed in six histograms. Each histogram shows the distribution of values around the target value of each observable. The gaussian function 5.7 is fitted to the histograms and the best fit parameters are shown both here and on Table 5.3. | 77 |
| 5.24 | After defining limits to each observable and removing some outliers, the study of the distribution of aligned values can be repeated. Each histogram shows the distribution of values around the target value of each observable, which can now be compared to the boundaries of the aligned range. The gaussian function 5.7 is fitted to the histograms and the best fit parameters are shown both here and on Table 5.3. | 78 |
| 5.25 | The duration of the two alignment cycles is compared by registering the time interval between iterations. Each iteration is further divided in four operations: Take Frame, Detect Pupils, Get Observables, Calculate Movements and Move Hexapod. To each operation corresponds a step with a height that carries no meaning other than to aid visualisation. | 79 |
| 5.26 | The two important coordinate axis are illustrated in this schematic representation. The source position is specified by $(X, Y, X)_{source}$, and it can be changed by altering the parameters of the OLED Screen bitmap or by physically moving the screen stage with the horizontal and vertical scales here shown. On the other end, the ingot, attached to the hexapod, has a position defined by $(X, Y, Z)_{ingot}$. For simplicity, the Scheimpflug plane inclinations aren't displayed here. | 80 |
| 5.27 | Results from two sets of alignments performed with "while" loop are plotted, for sources with different vertical shifts. Vertical shifts of the source, corresponding to a Z_{source} , were achieved by moving the screen vertically (purple dots) or by illuminating different rows of the screen (orange dots), now kept fixed. The x-axis displays the Z_{source} , in mm. The y-axis represents the final Z axis position of the ingot, in mm. Top: Linear fits performed to both sets of data, with best fit parameters $a = -1.001$ and $b = 13.762$ mm (moving screen) and $a = -1.024$ and $b = 14.184$ mm (changing source). Bottom: The residuals of the fits have a standard deviation of $\sigma = 0.024$ mm and $\sigma = 0.024$ mm, respectively. | 81 |

- 5.28 Results from two sets of alignments performed with "while" loop are plotted, for sources with different vertical shifts. Vertical shifts of the source, corresponding to a z_{source} , were achieved by moving the screen vertically (purple dots) or by illuminating different rows of the screen (orange dots), now kept fixed. The x-axis displays the z_{source} , in mm. The y-axis represents the final Y axis position of the ingot, in mm. **Top:** Quadratic fit performed to the moving screen data, with best fit parameters $a = 0.105 \text{ mm}^{-1}$, $b = -2.881$ and $c = 20.955$ mm. **Bottom:** The residuals of the fit have a standard deviation of $\sigma = 0.019$ mm. 82
- 5.29 Results from two sets of alignments performed with "while" loop are plotted, for sources with different vertical shifts. Vertical shifts of the source, corresponding to a z_{source} , were achieved by moving the screen vertically (purple dots) or by illuminating different rows of the screen (orange dots), now kept fixed. The x-axis displays the z_{source} , in mm. The y-axis represents the final X axis position of the ingot, in mm. **Top:** Linear fits performed to both sets of data, with best fit parameters $a = 0.031$ and $b = -0.457$ mm (moving screen) and $a = 0.016$ and $b = -0.223$ mm (changing source). **Bottom:** The residuals of the fits have a standard deviation of $\sigma = 0.008$ mm and $\sigma = 0.033$ mm, respectively. 83
- 5.30 Results from two sets of alignments performed with "while" loop are plotted, for sources with different horizontal shifts. Horizontal shifts of the source, corresponding to a y_{source} , were achieved with movements the screen parallel to the optical axis (purple dots) or by illuminating different columns of the screen (orange dots), now kept fixed. The x-axis displays the y_{source} , in mm. The y-axis represents the final Z axis position of the ingot, in mm. **Top:** Linear fits performed to both sets of data, with best fit parameters $a = -0.001$ and $b = -0.008$ mm (moving screen) and $a = 0.010$ and $b = -0.055$ mm (changing source). **Bottom:** The residuals of the fits have a standard deviation of $\sigma = 0.001$ mm and $\sigma = 0.002$ mm, respectively. 84
- 5.31 Results from two sets of alignments performed with "while" loop are plotted, for sources with different horizontal shifts. Horizontal shifts of the source, corresponding to a y_{source} , were achieved with movements the screen parallel to the optical axis (purple dots) or by illuminating different columns of the screen (orange dots), now kept fixed. The x-axis displays the y_{source} , in mm. The y-axis represents the final Y axis position of the ingot, in mm. **Top:** Linear fits performed to both sets of data, with best fit parameters $a = 0.932$ and $b = 0.899$ mm (moving screen) and $a = 0.899$ and $b = 0.720$ mm (changing source). **Bottom:** The residuals of the fits have a standard deviation of $\sigma = 0.131$ mm and $\sigma = 0.105$ mm, respectively. 85
- 5.32 Results from two sets of alignments performed with "while" loop are plotted, for sources with different horizontal shifts. Horizontal shifts of the source, corresponding to a y_{source} , were achieved with movements the screen parallel to the optical axis (purple dots) or by illuminating different columns of the screen (orange dots), now kept fixed. The x-axis displays the y_{source} , in mm. The y-axis represents the final X axis position of the ingot, in mm. **Top:** Linear fits performed to both sets of data, with best fit parameters $a = 0.015$ and $b = 0.122$ mm (moving screen) and $a = 0.034$ and $b = -0.050$ mm (changing source). **Bottom:** The residuals of the fits have a standard deviation of $\sigma = 0.022$ mm and $\sigma = 0.016$ mm, respectively. 85
- 5.33 The inclination of the screen relative to the (X,Y,X) reference system is illustrated. Black arrows indicate the front face of the OLED Screen. **Left:** Tilt of screen plane by $\alpha = 0.92^\circ$. **Middle:** Tilt of the screen plane by $\beta = 1.94^\circ$. **Right:** Tilt of the screen by $\gamma = 0.57^\circ$ 86

| | | |
|------|------------------------------------------------------------------------------------------------------------------------------------------------------------------------------------------------------------------------------------------------------------------------------------------------------------------------------------------------------------------------------------------------------------------------------------------------------------------------------------------------------------------------------------------------------------------------------------------------------------------------------------------------------------------------------------------------------------------|----|
| 5.34 | To monitor the alignment of the system, plots of the time evolution of each observable can be created. On the y-axis the values of the relative difference of each observable from the target value are shown: $O - O_{targetvalue}/\sigma$, where σ is the width of the alignment range. Here only the Flux $[C - B]$ is displayed as example. Top: Red crosses to mark the instants where the OLED Screen is changed, with respective LGS characteristics. Middle: Colored dots with the observables at the end of the alignment. Bottom: Black dots spaced by 1.5 seconds in between to control the alignment status. | 88 |
| 5.35 | Top: All the data relative to the control of the alignment of the system, as a function of time, for Flux $[C - B](\sigma)$. $ \sigma > 1 $ corresponds to misalignment. Bottom: Y-axis restricted to the 1σ boundary, for better visualisation. | 88 |
| 5.36 | Control Loop example run, lasting for a total of 6000 seconds, as random variations of the source were introduced. Black dots and source labels were omitted. Here, the observables Flux $[C - B]$, Flux $[A - [B + C]]$ and Distance $A - B$ evolution is registered, measured in σ | 89 |
| 5.37 | Control Loop example run, lasting for a total of 6000 seconds, as random variations of the source were introduced. Black dots and source labels were omitted. Here, the observables Distance $A - C$, $[Y_B - Y_B]$ and $\overline{S_{x1}} - \overline{S_{x2}}$ evolution is registered, measured in σ | 90 |
| 5.38 | The search algorithm scan follows a specific direction on the x-z plane, taking steps of size X_{step} and Z_{step} . The light intensity of the pupils at each location is recorded. At each level of the scan, the systems looks to maximise the search criterion. If on the first level (continuous arrows) no maximum is found, it moves on to the second level expanding the search radius (dotted arrows), and so on. | 91 |
| 5.39 | Contour plots show the scan performed on the x-z plane, with a resolution of 0.1 mm, revealing the logarithmic counts of the following quantities: Top Left: Total counts on pupil A; Top Right: Total counts on pupil B; Middle Left: Total counts on pupil C; Middle Right: Total counts on the three pupils A+B+C; Bottom Left: Total counts on the reflected pupils B+C; Bottom Right: Absolute value of the normalised flux difference between reflected pupils $ B - C /(A + B + C)$ | 93 |
| 5.40 | (a) The structure holding the ingot prism was vignetting the image at certain positions, revealing unexpected secondary maxima of the flux in pupil A; (b) The space between the ingot and the structure was covered with tape to remove the irregular vignetting, blocking light from passing in between; (c) The top and bottom surfaces of the ingot prism have a reflective nature that is not predicted on the ingot design. Hence, unexpected flux on the reflected pupils B and C was giving rise to secondary maxima on the B+C counts at certain positions; (d) The ingot's top and bottom faces were covered with tape, leaving only the two side faces uncovered. | 94 |
| 5.41 | Contour plots show the scan performed on the x-z plane, with a resolution of 0.1 mm, revealing the logarithmic counts of the following quantities: Top Left: Total counts on pupil A; Top Right: Total counts on pupil B; Middle Left: Total counts on pupil C; Middle Right: Total counts on the three pupils A+B+C; Bottom Left: Total counts on the reflected pupils B+C; Bottom Right: Absolute value of the normalised flux difference between reflected pupils $ B - C /(A + B + C)$ | 95 |
| 5.42 | Scan of the x-z plane showing the counts in pupil A and the values of $ B - C /(A + B + C)$. Due to the hexapod's limited range of motion and the observable's degeneracy (mainly the Y overshoot), the alignment of the I-WFS can only be successful if it starts on the area covered with red dots. | 96 |

| | | |
|------|-------------------------------------------------------------------------------------------------------------------------------------------------------------------------------------------------------------------------------------------------------------------------------------------------------------------------------------------------------------------------------------|-----|
| 5.43 | Schematic representation of the SSD1327 bitmap. It is a matrix of 64×128 entries, to illuminate the 128×128 pixels of the screen. Each entry consists of an hexadecimal number that controls the brightness level (0 – 16) of each pair of adjacent pixels. | 97 |
| 5.44 | Each entry of the screen's bitmap is an hexadecimal number that controls the brightness level of each pair of adjacent pixels. To choose the brightness of each pair, a hexadecimal value equivalent to the two grey scale levels is written on the bitmap, as illustrated here. The example of two pixels with 15 and 14 grey scale level results in the entry <i>0xED</i> | 98 |
| A.1 | Taken on 28 July 2010 and identified as an unusual shape, this profile shows a secondary sodium layer (relatively strong). The y axis shows the photon counts per altitude bin (with 126.5 metres width) at median altitude (in km) represented on the x axis. | 111 |
| A.2 | Taken on 16 July 2010, this profile was described as having a narrow peak on the upper half and a top hat on the lower. The y axis shows the photon counts per altitude bin (with 126.5 metres width) at median altitude (in km) represented on the x axis. | 112 |
| A.3 | Taken on 16 July 2010, this profile was classified as a typical wavy pattern. The y axis shows the photon counts per altitude bin (with 126.5 metres width) at median altitude (in km) represented on the x axis. | 112 |

Glossary

2D Two Dimensions.

3D Three Dimensions.

AO Adaptive optics.

CCD Charge-Coupled Device.

DL Deformable Lens.

DM Deformable Mirror.

dof Degrees of freedom.

ELT Extremely Large Telescope.

ELTs Extremely large telescopes.

ESO European Southern Observatory.

FIR Far Infrared.

FoV Field of View.

FWHM Full Width at Half Maximum.

GeMS Gemini Multi-Conjugate Adaptive.

GLAO Ground Layer Adaptive Optics.

HST Hubble Space Telescope.

IR Infrared.

I-WFS Ingot Wavefront Sensor.

JWST James Webb Space Telescope.

LGS Laser Guide Star.

LIDAR Laser Imaging Detection and Ranging.

LLT Laser Launcher Telescope.

LTAO Laser Tomography Adaptive Optics.

MAD Multi-Conjugate Adaptive Optics Demonstrator.

MCAO Multi-Conjugated Adaptive Optics.

MIR Mid Infrared.

MSL Mean Sea Level.

NCPA Non-Common Path Aberration.

NGS Natural Guide Star.

NIR Near-Infrared.

NOAO No Adaptive Optics.

OLED Organic Light-Emitting Diode.

PSF Point Spread Function.

P-WFS Pyramid Wavefront Sensor.

rms Root Mean Square.

RTC Real Time Computer.

SC Sky coverage.

SCAO Single Conjugated Adaptive Optics.

SCIDAR SCIntillation Detection And Ranging.

SFR Star Formation Rate.

SH-WFS Shack-Hartmann Wavefront Sensor.

SNR Signal-to-Noise Ratio.

SR Strehl Ratio.

UV Ultraviolet.

WFS Wavefront Sensor.

WLGS SO Wendelstein Laser Guide Star Unit.

XAO eXtreme Adaptive Optics.

Chapter 1

Introduction

"I much prefer the sharpest and clearest eyesight, accompanied by a very moderate intelligence, over the very best intelligence accompanied by dull eyesight; and I am astonished how anyone can doubt the truth of the telescope, for the very construction of the telescope proves that the eyes see from a distance and do not touch the objects seen."

In "Dioptrice" [14], Johannes Kepler emphasised the revolutionary potential of telescopes, instruments that surpass the boundaries of what the human eye can see and allow astronomers to study celestial objects from vast distances. The invention of the telescope by Galileo Galilei ushered in a series of groundbreaking scientific discoveries, sparking both revolutionary advancements and conflicts that challenged humanity's perception of its place in the cosmos.

Despite initial resistance to change, the telescope emerged as a tool that seeks truth in realms beyond our physical reach, rendering its observations inherently unbiased. This pivotal discovery propelled Astronomy from laborious naked eye measurements to swift instrument-aided observations, compressing what once took hours into a matter of minutes. This evolution facilitated a deeper understanding of the natural world and enabled explorations of the profound depths of the universe.

1.1 The Development of Ground-based Telescopes

In the first centuries after Galileo's discovery, other astronomers sought to build telescopes with bigger primary mirrors, while at the same time different shapes and configurations were experimented with, and new polishing and engineering techniques were developed. Christian Huygens, Isaac Newton, James Gregory, Laurent Cassegrain, William Hershell, and others all contributed to the development of astronomical instrumentation, but all came across the same limitation to the optical quality of the images. The "perpetual tremor" [15] previously observed in twinkling stars was joined by blurred images of planets and nebulae, even from the best telescopes being developed, and the common cause of this evil was atmospheric turbulence.

Gradually, the value of operating a large telescope at a site with excellent seeing became evident in order to take full advantage of each telescope's capabilities. At the beginning of the twentieth century, at the top of Mount Wilson, George Ellery Hale built several 100-inch class reflector telescopes [16] and was able to record 1" diameter star images of 20th magnitude,

in 4-hour long exposure images [17]. For comparison, Galileo's telescopes had a resolving power of only 10" - 15". With the same telescopes, Hubble determined the first clues to the expansion of the universe. This period in Astronomy was marked by a multitude of groundbreaking discoveries. Together with the invention of photography, faint nebulae, invisible to the human eye, were discovered, followed by the successes of spectrography in measuring compositions of stars and planets.

But by 1980, the design of the astronomical telescope had reached a new plateau. Although great light-gathering power had been achieved, the performance of large telescopes encountered a barrier set by atmospheric turbulence. Even the most optimal observation sites struggled with seeing conditions that hindered the potential improvement in angular resolution of these telescopes. The astronomical community was in need of a novel technology capable of mitigating the impact of atmospheric turbulence and the solution came from Horace W. Babcock.

1.2 Adaptive Optics: a solution with limitations

Babcock became familiar with the turbulent elements in the atmosphere, how they behave in size and as time passes, and by 1953 he published the first design of a system combining a seeing sensor and a wavefront corrector - it was the first Adaptive Optics (AO) system [18]. A full description of the principle of AO and the components of an AO System is provided in Chapter 3.

In the following decades, when the need for wavefront corrections became evident, Babcock, Linnick, Leighton, and other researchers were able to come up with innovative concepts for systems that could increasingly counteract atmospheric turbulence. Scientists' minds were bursting with ideas as they sought to find improvements to the first simple AO systems, but the cost of production posed an obstacle to further developing them. Only after the invention of the laser in 1960, AO saw an exponential increase in interest, as its potential uses for defence purposes became attractive to the US Military Departments. When their technological advances finally became available to the scientific community, astronomical research institutes started implementing and further developing AO systems. They became more and more aware of the main two limitations of seeing compensation: the need for a bright reference star and the small isoplanatic angle limiting the field of view.

Today, AO is recognised as an essential component of large ground-based astronomical telescopes (with diameters bigger than one metre). Other methods have been suggested to reduce the seeing effects e.g. speckle interferometry and lucky imaging. However, the former method is limited to only a few scientific applications and the latter is limited to small telescopes up to ≈ 2 m and wavelengths longer than $0.8 \mu\text{m}$ [3]. Alternatively, the reader may think immediately that to overcome atmospheric turbulence limitations it is as simple as investing more in space-based telescopes. The downside of this approach is that space-based telescopes are much more expensive, limited in size, weight, and materials, and have lower overall performance compared to ground-based telescopes. Maintenance and upgrade routines are more challenging, if not impossible, and active thermal and altitude control add to the complexity of the systems. Although they are necessary to obtain images at certain spectral windows to which the atmosphere is opaque, ground-based telescopes will always be larger than space-based telescopes. Hence, in the near-IR and IR ranges, ground-based telescopes with AO have an advantage in both resolution and light gathering

power. In Chapter 4, the potential of an Extremely Large Telescope (ELT) with AO incorporated is explored, and the anticipated performance is expected to be significantly improved relative to the most advanced space-based telescopes, such as the James Webb Space Telescope (JWST).

Overall, integrating AO in large ground-based telescopes brings improvements in angular resolution and an increase in Signal-to-Noise Ratio (SNR) for faint sources, which consequently increases limiting magnitudes and decreases exposure times. However, the higher resolution achieved is only over a much smaller Field of View (FoV). As example, ESO's Very Large Telescope (VLT) AO system can achieve resolution of $\sim 0.015''$ over a FoV of a few arcseconds in the visible and up to $\sim 0.5' - 1'$ in the infrared bands (K band, $\lambda \sim 2.2 \mu\text{m}$). These values can be compared to Hubble Space Telescope (HST), capable of achieving resolutions of $0.05''$ in visible light (at wavelengths near 500 nm) over a field of $2.6'$. This phenomenon called anisoplanatism is one of the biggest challenges that current AO researchers are trying to overcome. It derives from AO's basic working principle: the wavefront of a point reference source located close to the scientific target is measured by a wavefront sensor. The angle around the point source at which the mean square wavefront error after corrections is 1 rad^2 is typically very small at visible wavelengths, sometimes $< 10''$. Furthermore, the need for bright reference sources close to the target only increases the impact of this on the sky coverage, which for limiting magnitudes of $m_v = 10$ is $1/100000$ of the hemisphere.

Undoubtedly, AO is a tool with great potential to bring astronomical imaging to the next level, but having such a limited sky coverage is still a factor against incorporating it on every telescope and applying it in all astronomy research fields. It appears that still some further adjustments need to be made to solve the biggest AO limitations.

1.3 Laser Guide Stars

A (partial) solution to this problem is to create beacons in the atmosphere by lasers fired close to the aperture of the telescope, allowing one to place a bright reference star at any position in the sky. Already mentioned a few paragraphs ago, Linnik [19], in 1957, was the first to mention this as a possible solution, but only in more recent decades astronomical institutes started incorporating Laser Launcher facilities in the telescopes. The sources created in this way are called Laser Guide Stars (LGS) and they give the telescope the capability to enlarge the sky coverage. The collaboration between the U.S. Air Force researchers and the Astronomical community to explore the potential of LGS has brought about remarkable advancements. There are mainly two types of LGS: Rayleigh and Sodium. They originate from different physical processes and have different characteristics (altitude and extension in the atmosphere). Recently, the Sodium LGS appear to be the preferred approach for astronomical AO.

However, Sodium LGS are not point-like sources but rather reveal an elongated shape in the sky. The intrinsic elongated nature of these artificial stars impacts the performance of usual wavefront sensors used in AO, which were designed to achieve peak performance with point-like sources. This effect becomes more significant as the diameter of the telescopes increases, so in future epochs dominated by ELTs, it cannot be ignored. New technologies are required to take full advantage of LGS and maximise the performance of AO in future large telescopes.

1.4 Goals of this work

In this work, I focus on a new wavefront sensor designed to cope with this typical elongation of LGS, in the framework of the European Extremely Large Telescope (E-ELT) project. The Ingot Wavefront Sensor (I-WFS), whose concept was introduced by Ragazzoni et al 2017 [20], is a pupil plane Wavefront Sensor (WFS) and consists of a combination of refractive and reflective surfaces arranged onto a complex prismatic shape that extends in three dimensions. Its three-dimensionality matches the geometric characteristics of the LGS image and allows the reference beacon to be sensed along its entire length.

It is an ambitious project set out to develop a new sensor that allows to optimise the performance of the AO systems of the new generation of telescopes, overcoming some well-known limits related to the use of LGS. The project's feasibility and expected performance is being studied by the Adaptive Optics Group of INAF-OAPd ¹. So far, it accounts for studies of the sensor's optical design, numerical simulations set out to investigate the performance of the sensor on an ELT-like telescope, assembly of a test bench with a first prototype of the I-WFS, and laboratory tests aimed at studying the response and the sensitivity of the sensor. In this thesis, the continuation of the experiments is picked off from a point where fully automated calibration and alignment procedures were already developed.

My master thesis focuses on deepening the understanding and more precisely characterising the I-WFS performance, as it deals with extended sources. To achieve that, I undertook the necessary steps to comprehend the experimental setup and existing prototype restrictions.

1.5 Thesis Outline

Chapter 2 serves as a pedagogical introduction to the statistical characterisation of atmospheric turbulence and imaging, whose understanding is of utmost importance to a clear exposition of the fundamental working principle of AO.

Following, Chapter 3 dives into describing to a bigger extend AO systems, their composition and functioning. Section 3.1.1 is dedicated to LGSs, where their advantages and limitations are highlighted. The most used wavefront sensors are summarised and a description of the new I-WFS is provided. The potential improvements that the I-WFS can bring when extended sources are used for wavefront sensing are detailed in Section 3.2.

On Chapter 4, E-ELT current designs and AO performance prospects are presented, along with example science case studies that will benefit from AO performed with LGS.

Finally, the experimental results on a test bench with a prototype of the I-WFS are presented on Chapter 5. This includes a brief summary of work previously performed, followed by the work in which I contributed the most.

One of the first contributions was the design of an algorithm capable of implementing changes to the simulated LGS in a fast and versatile way, described in Section 5.2. This innovation brings the simulation closer to replicating real LGS characteristics. After tackling the main limitations and implementing necessary modifications to the test bench elements and existing scripts, I developed and tested an improved alignment procedure, described in Section 5.3. These alignment tests, described in Section 5.3.1, provided further insight into the adequacy and sensitivity of the current observables used to manipulate the degrees of

¹Istituto Nazionale di Astrofisica - Osservatorio Astronomico di Padova

freedom of the sensor. Additionally, they allowed us to understand the impact of optical aberrations and identify previously unaccounted-for setup anomalies.

Meanwhile, during attempts to simulate a closed-loop AO system, detailed in Section 5.4, I developed a routine capable of controlling and maintaining the alignment of the WFS. This routine leads the I-WFS to adapt itself to sporadic LGS changes and recover the aligned configuration. Later on, because we aimed to prepare this sensor for the scale and requirements of the ELT, the need arose to start developing a search algorithm, detailed in Section 5.5. This algorithm can locate the image focus and bring the system closer to an aligned position, starting from highly misaligned configurations.

Throughout the six months, there was an awareness of the necessity to incorporate real sodium layer profiles with brightness variations at different altitudes. To address this, we sought a new display element capable of accommodating such complexity. As a result, on Section 5.6 we present this newly found element and briefly discuss the steps that follow the sodium layer profile discretisation and its replication on the LGS.

The conclusions of this work can be found on Chapter 6.

Chapter 2

Atmospheric Turbulence

Astronomers take advantage of telescopes to study celestial objects, hoping to gather as much information as possible about them by catching the photons they emit. These little quanta of energy are one of the only sources of information about what lies outside our planet, travelling huge distances across the universe until they reach our instruments. In the last kilometres of their journey, they cross the Earth's atmosphere which, unfortunately, is far from being a perfect window to gaze through. There they are diverted from their course, similar to how a straw appears to be bent as it enters the water when viewed from the side of the glass. This limits our ability to make accurate scientific measurements with ground-based telescopes.

In the following sections, a summary of the current knowledge of atmospheric turbulence is given, based mostly on Kolmogorov's model of turbulence. Then, a statistical description of the effects of atmospheric seeing is presented, together with the most relevant seeing parameters, whose understanding is very important to adequate the AO system to the telescope optics, at the particular observing site and local seeing conditions. Finally, a quantitative model of wavefront aberrations is described. The upcoming analysis seeks to elucidate the capabilities of an AO system in terms of mitigating atmospheric distortions and achieving images with diffraction-limited quality in real-time.

2.1 Diffraction Limit: in the Absence of Atmospheric Turbulence

A telescope collects a part of the incoming spherical wavefronts emitted by a celestial source, which can be treated as plane wavefronts by the time they reach Earth, in the absence of atmospheric turbulence. Then, optical systems curve the wavefronts and focus them onto the focal plane of the detectors, as shown on Figure 2.1. Hence, the aperture of the telescope behaves as an obstacle in the path of the wavefront which, as explained by the Huygens principle, leads to the phenomenon of diffraction. Therefore, even before including atmospheric effects onto this analysis, a perfect optical system cannot obtain a perfect point image of a point source at infinity. The resulting enlargement of the point-like source can be further explained by Heisenberg's uncertainty principle: the aperture or stop of the telescope introduces an uncertainty in the direction of motion of the photons.

Herschel [21] was already aware of this lower limit to the angular size of a point source, but George B. Airy [22] was the first to provide a mathematical description of the phenomenon. The pattern formed, named "Airy pattern" after him, describes the image of a point-like

2.1. DIFFRACTION LIMIT: IN THE ABSENCE OF ATMOSPHERIC TURBULENCE

source, e.g. a star, formed by a circular aperture of diameter D as a bright disk surrounded by a series of faint rings of rapidly diminishing brightness. For a perfect optical system, the angular radius of the first dark ring of the Airy pattern is given by:

$$\theta_{Airy} = 1.22 \frac{\lambda}{D} \quad (2.1)$$

where λ is the wavelength of the light. This is the most simple diffraction pattern caused by a circular aperture. When obstructions are included in the light path, such as a central obstruction or spiders holding secondary mirrors, the pattern becomes more complicated. Generally, the response of an imaging system to a point source is called the Point Spread Function (PSF). θ_{Airy} is also used to define the Rayleigh criterion of resolution: two sources are said to be just resolved when the principal maximum of the diffraction pattern of one lies at the first minimum of the other.

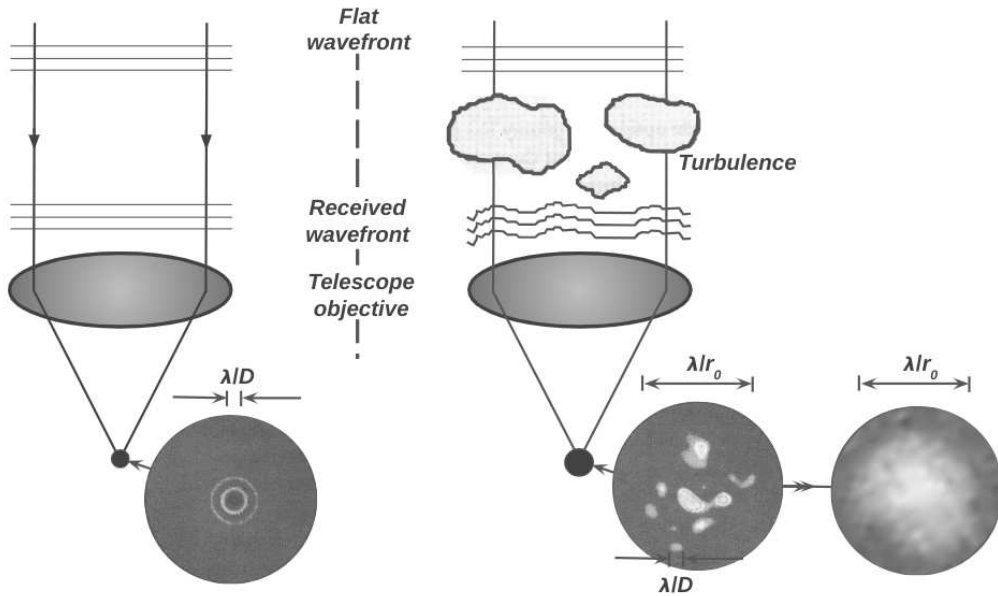


Figure 2.1: The resolution of astronomical images depends on the turbulence encountered by the flat wavefronts as they cross the atmosphere. **Left:** In the absence of turbulence, the wavefronts arrive still flattened at the telescope aperture. This situation forms diffraction limited images with a characteristic Airy pattern of resolution λ/D . **Right:** In the presence of atmosphere, the flat wavefronts are perturbed by turbulent cells of average size r_0 . D/r_0 Speckles of size λ/D are seen on short exposures ($t < t_0$). In long exposures the speckle pattern gets blurred over an area of λ/r_0 . This blurred image is said to be seeing limited. Image adapted from Parenti [1].

In summary, without atmosphere, the angular resolution of a telescope would be limited by diffraction and increases linearly with D , while the SNR of a point source grows with D^2 . Images where θ_{Airy} is actually the minimum angular separation of two near-by point sources are called *diffraction limited*.

Unfortunately, we cannot ignore the distortions caused by atmospheric turbulence when using large ground-based instruments (with diameters larger than one metre). These occur near the end of the journey across Earth's atmosphere, nor can we ignore the ones added by the telescope itself, related to mechanical distortions, flexures and stresses arising from temperature variations. All these aberrations contribute to the spread of the light of a star

into a "seeing disk", which may be 10 - 100 times larger than the diffraction limit of the telescope itself, degrading the angular resolution and greatly reducing the peak intensity, bringing the SNR down. Increasing further the diameter D of the telescope will not improve the spatial resolution because of the other contributors to the total width of the image.

In the following section we go into more detail about the effects caused by the Earth's atmosphere.

2.2 Observing through the Atmosphere

The atmosphere has three main characteristics that on the one hand, allow Life to thrive on the Earth, and on the other hand, restrict astronomical observations:

- Opacity to certain wavelengths, due to absorption of light.

The molecular and atomic composition of the atmosphere makes the interactions between light and matter complex. Absorption, which occurs at discrete wavelengths, sometimes blends into an extended absorption region of the spectrum because of the proximity of vibrational and rotational energy levels of molecules. Consequently, the atmosphere is opaque to the spectral ranges below $0.3 \mu\text{m}$, where absorption is mainly caused by O_2 , N_2 and O_3 molecules, and above $30 \mu\text{m}$ up until 1 m , in the microwave domain. In the long-wavelength radio limit, above 10 m , radiation is reflected off the top of the atmosphere due to the high concentration of free electrons and ions in the ionosphere. On the IR domain, absorption is instead characterised by a series of narrow transparent windows and large absorption bands due to oxygen, carbon dioxide and water vapour. Figure 2.2 summarises the different windows.

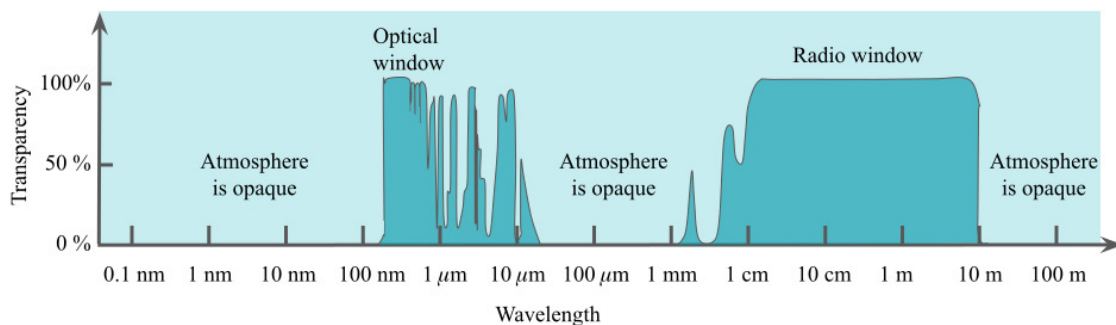


Figure 2.2: The atmosphere's transparency varies as a function of the wavelength. To some wavelength ranges it is completely opaque such as the shorter UV limit ($\lambda < 0.3 \mu\text{m}$), the microwave range and radio. Instead, complete transparency takes place in the optical and shorter wavelength radio window (1cm-10m). Absorption in the IR is characterised by a series of shorter transparent windows and large absorption bands. Image adapted from Hardy [2].

Of interest for ground-observations are the visible regions, $0.38 - 0.8 \mu\text{m}$, the near-IR (NIR), $0.8 - 2.5 \mu\text{m}$, the mid-IR (MIR), $2.5 - 25 \mu\text{m}$, the far-IR (FIR), $25 - 350 \mu\text{m}$, and the radio, $1 \text{ cm} - 10 \text{ m}$, to which the atmosphere is transparent. Moreover, it may be of interest to the reader to become familiar with some NIR bands which are extremely relevant to AO: $1.25 \mu\text{m}$ (J band), $1.6 \mu\text{m}$ (H band), $2.2 \mu\text{m}$ (K band) and $3.4 \mu\text{m}$ (L band). To study other regions of the spectrum, observations must be made

at higher altitudes either with balloon experiments, airplanes or space-based telescopes, depending on the wavelength.

- Intrinsic luminosity, due to scattered light:

Scattered sunlight is the largest source of sky radiation during the day and on moonlit nights, but on moonless nights most of the atmospheric radiation between $0.5 \mu\text{m}$ and $2.5 \mu\text{m}$ is due to airglow emissions from hydroxyl (OH) molecules. Background radiation from the sky sets a practical limit to the detection of faint objects from Earth's surface.

- Turbulence, due to the heat exchanges of the atmosphere with the Sun and the Earth:

The energy input of solar heating at the top of the atmosphere throughout the day leads to a diurnal cycle of heating and cooling of Earth's surface. The transfer of energy between the top and bottom layers of the atmosphere results in large spatial scale motions of air masses. As the large-scale motions break down into smaller-scale motions, small turbulent eddies distribute themselves along the atmosphere, each with different properties. The result is an atmosphere which is not optically homogeneous, characterised by temporal and spatial variations of pressure, density and temperature.

The refraction of the optical rays as they cross layers and pockets of air with slightly different refractive indices (n) leads to distortions of the wavefront crossing the atmosphere. According to Snell's law, the angular deviation in the trajectory of a light ray as it encounters a surface boundary depends on the ratio of the refractive indices of the medium of the incident ray n_i and of the refracted ray n_r . The refractive index of air itself, n_{air} , depends on the temperature T , the pressure P of the medium, and the water vapour pressure p in mbars. A full treatment on the dependencies of refractive index of air can be found at [23], but for the purpose of this thesis I would like to point out the expression for optical wavelengths named the Gladstone-Dale equation, where p is neglected [24]:

$$n_{\text{air}} - 1 = 7.7 \times 10^{-5} \frac{P}{T} \quad (2.2)$$

Imagining the atmosphere to be composed of several layers with a refraction index that continuously increases as the height of the Earth's surface decreases, each wave coming from an astronomical object will always bend toward the Earth's surface normal. However, due to the complexity of the gradients of temperature not only vertically but also horizontally, on a continuous spatial and temporal horizontal manner, the plane waves that arrive are continuously bent and the individual phases of parallel light rays are thus shifted with respect to each other. The net result is wavefront perturbation.

In the following chapter, turbulence is discussed from a statistical point of view, as it is a random phenomenon. This is necessary in order to characterise the air refractive index and the wavefront distortions that result from it.

2.3 Kolmogorov Theory of Turbulence

To understand the fluid behaviour of the atmosphere, fluid dynamics, i.e, the Navier–Stokes equations that govern the velocity and pressure of a fluid flow, must be taken into consideration.

A very short summary of the physics of fluid dynamics is that there are two distinct states associated to fluid motion: laminar or turbulent, depending on the relative importance of the inertial and viscous forces within the fluid. The distinction between the two regimes was clarified by Reynolds [25], who realised that the criterion for the transition depended on a quantity he named Reynolds number, given by:

$$R_e = \frac{V_0 L_0}{\nu} \quad (2.3)$$

where V_0 is the characteristic flow velocity, L_0 is the characteristic size of the flow and ν is the kinematic viscosity of the fluid (a ratio between the fluids viscosity and density $\nu = \mu/\rho$). Laminar flow occurs at low R_e (< 500), where viscous forces are dominant and the fluid motion is smooth and constant, without mixing of layers. Turbulent flow occurs at high R_e , where inertial forces dominate and tend to produce eddies¹ and vortices. When R_e exceeds the critical value of 2000, the flow is turbulent. Plugging in the average values of our atmosphere: $V_0 \sim 10\text{ms}^{-1}$, $L_0 > 15\text{ m}$ and $\nu = 15 \times 10^{-6}\text{m}^2\text{s}^{-1}$ we get $R_e \approx 10^7 \gg 2000$. This implies that Earth's atmosphere is in fully-developed turbulent motion.

The velocity field of a turbulent fluid fluctuates randomly about its mean value. This implies that it has a random nature, each point in space and time within the flow the velocity may be represented by a random variable and therefore it can only be described statistically, using estimates such as variances, mean values and standard deviations.

Kolmogorov, in his theory of turbulence, defined a set of hypothesis about the velocity random variable and together with the principal equations of fluid dynamics, aimed at describing both atmospheric turbulence and its effects on optical systems. He stated that the velocity field at small-scales is, to a first approximation, statistically homogeneous, isotropic and independent of the large-scale structure [28]. With these hypothesis, Kolmogorov was able to describe the pattern of the energy spectrum for different sized turbulent eddies, since energy is injected in the atmosphere until it dissipates into heat.

The ultimate source of energy in Earth is solar heating, which during the day strikes the surface during the day and generates convection cells. At night, wind mixes air masses of different temperatures and altitudes. Consequently, large-scale eddies of size L_0 (the "outer scale") with high Reynolds numbers are generated. They are unstable but because viscosity is unimportant in their motion they cannot dissipate energy into heat. Instead, they break up and their kinetic energy is transferred successively to smaller scales, forming an energy cascade [29], [30]. This cascade, illustrated in Figure 2.3 continues until R_e is sufficiently small, at scales of size l_0 (the "inner scale"), such that the eddy motion is stable and kinetic energy is converted into heat by viscous friction. The one-dimensional turbulence energy spectrum, valid for eddies with sizes between l_0 and L_0 can be deduced from dimensional considerations:

$$E_k \propto k^{-5/3}, \quad k = \frac{2\pi}{L} \quad (2.4)$$

The three-dimensional spectrum follows a $-11/3$ power law.

Tatarski [31] extended Kolmogorov's statistics of turbulent velocity to 3D to make them

¹The concept of an eddy is a complex one to define [26], but following Kolmogorov's work we'll assume for now that it is a patch of fluid conceptually separated from the rest of the flow, with a size l , and a characteristic internal velocity difference [27]. An eddy of wave number k may be thought of as some disturbance containing energy.

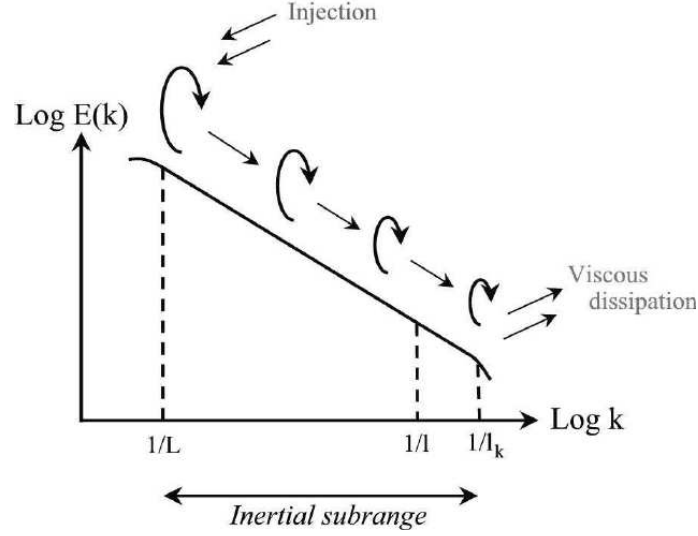


Figure 2.3: Kolmogorov's theory of turbulence describes the energy cascade of turbulent eddies since energy is injected in the atmosphere at the outer scales until it dissipates into heat by viscous friction. The one-dimensional energy spectrum, valid for eddies within the inertial sub range ($l < l_k < L$) follows the law $\log(E_k) = -\frac{5}{3} \log(k)$, $k = 2\pi/l$. Image taken from [Wikipedia](#)

applicable to describe the distribution of the refractive index and, to do so, he used structure functions. A structure function $D_f(\vec{r})$ is a measure of the intensity of the local fluctuations of a random function f around a point \vec{r} . Kolmogorov found the expression of the velocity structure function, but we are more interested in the temperature and the refractive index structure functions, as these two parameters are the ones that affect optical propagation, not the velocity of the fluid.

$$D_T(\vec{r}) = \langle |T(\vec{r}) - T(\vec{r} + \vec{\rho})|^2 \rangle = C_T^2 r^{2/3} \quad (2.5)$$

$$D_n(\vec{r}) = \langle |n(\vec{r}) - n(\vec{r} + \vec{\rho})|^2 \rangle = C_n^2 \rho^{2/3} \quad (2.6)$$

where $|\vec{\rho}| = \rho$ is the size of the vicinity of \vec{r} where the average $\langle \rangle$ is being calculated. C_T^2 is the temperature structure coefficient and C_n^2 is called index structure coefficient and are a measure of the total amount of inhomogeneities in temperature and n , respectively. C_n^2 can be directly estimated through various techniques such as SCIDAR (SCIntillation Detection And Ranging) or, indirectly, measuring C_T^2 using aerostatic balloons. Then, C_n^2 and C_T^2 can be related by the Gladstone Equation 2.2.

On average, C_n^2 decreases with altitude but does show peaks at some specific heights due to the shear of two air masses, where turbulence is higher, or regions where there is a large vertical thermal gradient, such as the thermal inversion of the tropopause at 10 km or at half troposphere (~ 5 km). A schematic representation of the altitude dependence of C_n^2 is shown in Figure 2.4.

Usually, a division of the atmosphere in 3 different regions is made: surface layer, planetary boundary layer and free atmosphere layer. The surface layer is the most turbulent layer, and extends up to a few tens of metres from the ground. Here direct thermal exchanges with the ground create large convection currents. The planetary boundary layer can be found next, until around 1 km above sea level. Here the C_n^2 increases by several orders of magnitudes at

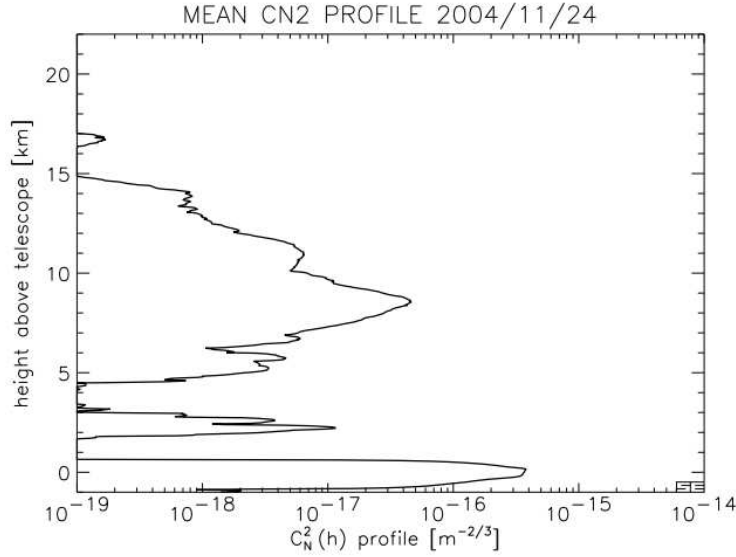


Figure 2.4: The $C_N^2(h)$ profile as a function of height h is plotted, measured with a SCIDAR at Mt. Graham which is at a height of 3.3 km above mean sea level. The profile is plotted with the height h above the telescope along the y-axis, and the strength of the turbulence along the x-axis in logarithmic scale. The surface layer, which consists of the first few metres above the telescope where the atmosphere is the most turbulent, shows a maximum of C_N^2 . Another weak layer is seen at $h \sim 3$ km. At $h \sim 9$ km, so altitude of 12 km above sea level, there is weak but extended peak of C_N^2 . Image from Sebastian Egner's PhD thesis [3].

thin layers a few hundred metres thick. At the tropopause, around 10 km, there is often a peak in turbulence due to wind shear caused by the thermal inversion [2]. Finally, in the free atmosphere, which extends from 1 km upwards, the turbulence is generated by meteorological events and continuing to higher heights, C_n^2 decreases until it can be neglected, for $h > 25000$ m [4].

These statistical considerations and precise knowledge of the C_n^2 profiles are relevant to describe the statistics of the wavefront aberrations and obtain the spatial power spectral density of the refractive index n , denoted by $\Phi_n(k)$. This is a measure of the statistical distribution of the size and number of turbulent eddies of wavenumber k . The complete mathematical treatment, related to the fourier inversion of the structure function can be found in [31], but the main result is:

$$\Phi_N(k) = 0.033C_N^2k^{-11/3} \quad (2.7)$$

This is called the Kolmogorov spectrum, which, as stated, is only useful between the outer and inner scales of turbulence. The following step is to find the effect of a thin turbulent layer on an incident plane wave, and quantify the deformation.

2.4 Seeing Parameters

In this section, we'll try to characterise seeing, the degradation of the Airy disk of a point-like source, taking advantage of Kolmogorov's theory.

Inside the atmosphere, flat wavefronts get deformed depending on the refractive index fluctuations along the optical path (which for us corresponds to the line of sight). The

consequent wavefront phase fluctuation follows the following relation:

$$\phi = k \int n(z) dz \quad (2.8)$$

where k is the wave number, which varies as $k = 2\pi/\lambda$. Again, we are interested in a statistical treatment of the wavefront phase fluctuations inside the telescope aperture. Therefore, recurring to the structure function of phase $D_\phi(\xi)$, where ξ is the size of the region where the averages are calculated, we get:

$$D_\phi(\xi) = 2.91k^2(\cos\gamma)^{-1} \int C_N^2(h) dh \xi^{5/3} \quad (2.9)$$

where coordinate z along the line of sight was replaced by h , the height above the ground, with the airmass relationship ² [32]. This equation is often seen in a simplified way by defining a quantity r_0 , the Fried parameter.

$$r_0 = \left[0.423k^2(\cos\gamma)^{-1} \int C_N^2(h) dh \right]^{-3/5} \propto \lambda^{6/5} \quad (2.10)$$

$$D_\phi(\xi) = 6.88 \left(\frac{\xi}{r_0} \right)^{5/3} \quad (2.11)$$

The **Fried parameter** r_0 , which has dimensions of a length, characterises the effect of atmospheric turbulence at a particular wavelength [33, 34]. It can be interpreted as the average size of a turbulent cell. An important property of r_0 is that the root mean square phase distortion over a circular area of diameter r_0 is about 1 radian. A phase error of 1 rad ($\lambda/2\pi$) is the threshold above which the image quality deteriorates rapidly. Hence, small values of r_0 correspond to strong turbulence and poor seeing. Furthermore, r_0 varies with the $6/5$ power of wavelength and with $-3/5$ power of the air mass. Typical values for astronomical observations range from less than 5 cm in strong daytime turbulence to over 20 cm in good sites at night, at $\lambda = 0.5 \mu\text{m}$.

If r_0 represents the length scale, in the wavefront plane, after which the wavefront phase varies statistically by more than one radian, similarly we can define the **isoplanatic angle** θ_0 , which is the angle on-sky within which the wavefront phase varies by less than one radian. Inside a FoV defined by this size and centered on a reference source, all sources are affected by the same aberrations as the center reference source.

$$\theta_0 = 0.314 \frac{r_0}{H} \propto \lambda^{6/5} \quad (2.12)$$

with H the turbulence layer average height.

The **coherence time** τ_0 is the last important parameter, related to the typical timescale into which the wavefront phase changes by one radian and hence the wavefront can be considered roughly constant. So far we have dealt with spatial structure functions but it is also useful to consider the temporal changes of the structure functions. The Taylor hypothesis is a convenient approximation, which assumes that the time scale for these changes is much longer than the time it takes the wind to blow the turbulence across the telescope aperture. Considering each layer as made of a frozen pattern, that is transported by wind across the aperture, the temporal behaviour will mostly add a dependence on the wind speed of the

² $z = h/\cos(\gamma)$, where γ is the angular distance of the source from the zenith

considered layer, v .

$$\tau_0 = 0.36 \frac{r_0}{v} \propto \lambda^{6/5} \quad (2.13)$$

Typical values for wind speeds are 20 ms^{-1} , giving $\tau_0 \approx 10^{-2} \text{ s}$ in good seeing conditions ($r_0 = 20 \text{ cm}$). The inverse of τ_0 corresponds to the **Greenwood frequency** $f_G = \tau_0^{-1}$. Independent measurements taken at Mount Wilson have given estimated of f_G to be of the order of $20 - 40 \text{ Hz}$

2.5 How can Adaptive Optics be helpful?

The effects of turbulence on the image produced by an uncompensated telescope depend both on its aperture D and on the Fried Parameter r_0 . If, on the one hand, a telescope is said to be diffraction-limited if it achieves a resolution $\theta = \theta_{Airy} \sim \lambda/D$, on the other hand, atmospheric turbulence reduces the resolution of the images down to $\theta = \lambda/r_0$, where the telescope is said to be seeing-limited. Let's take some numbers to see the degrading effect of turbulence. A diffraction-limited 4 metre telescope is capable of having a resolution of $0.03''$ at $0.5 \mu\text{m}$ (FWHM of the airy disk). If being used to observe from a local site of relatively good seeing, e.g. Mauna Kea [35], its been observed that the median seeing disk has a FWHM of $0.5''$, almost 10 times worse.

The deformations caused by seeing can be decomposed in two components, illustrated in Figure 2.5:

- The mean wavefront tip-tilt: the turbulence at the outer scales produces a time-varying wavefront tilt which randomly displace the centre of the image. These movements result in larger blurred images for long exposures.
- High-order aberrations of the wavefront: higher spatial frequency fluctuations of the refractive index translate into a phase difference between the various parts of r_0 size of the same wavefront, causing a differential delay in the wavefront phase. Consequently, a large number of speckles of diameter λ/D appear on the focal plane.

Additionally, the images look differently if taken with short or long exposures, as depicted on Figure 2.1. Short-exposures consist of the speckle structure, which is usually masqueraded by the image motion in long-exposures. For the latter, the turbulence randomly displaces the speckles, producing the seeing-disk of size λ/r_0 . Another consequence of this blurring is that the light which is usually 84% concentrated on the principal maximum of the diffraction-limited pattern, will be spread over a bigger central core, thus reducing the peak intensity of the PSF.

When a telescope has a diameter larger than the Fried's parameter, $D \gg r_0$, the higher order perturbations dominate. Telescopes with $D < r_0$, on the contrary, are dominated by tip-tilt as the portion of the wavefront intercepted is smaller than the average size of the unperturbed wavefront (perturbation smaller than 1 radian).

This is where the potential of using AO systems becomes evident: full compensation of atmospheric turbulence should improve the angular resolution from its seeing-limited value to its diffraction-limited value. The FWHM of the PSF is a good measurement of the improvement in resolution. Additionally, light is transferred from the seeing disk to the central core of the image.

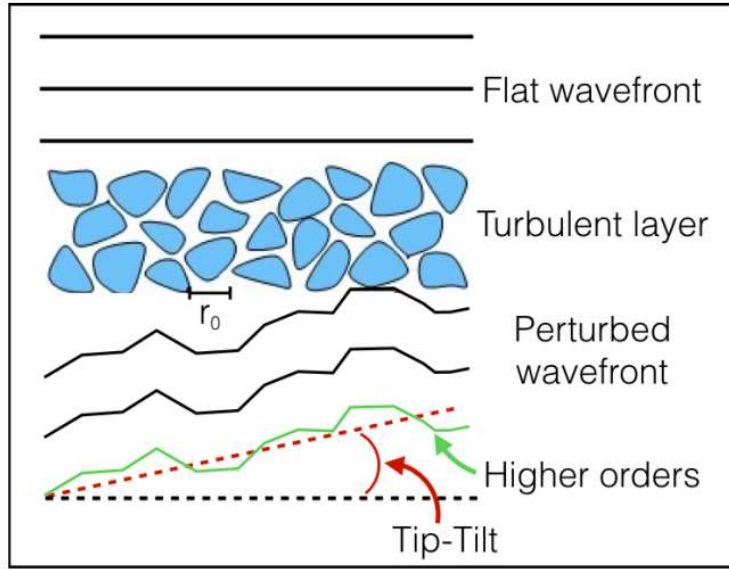


Figure 2.5: As flat wavefronts cross the atmosphere and encounter turbulent cells of different sizes, they get perturbed. The deformations caused can be decomposed in two components: the mean wavefront tip-tilt and higher order aberrations. Image from Maria Bergomi’s PhD thesis [4].

A quantity called Strehl Ratio SR is defined, to quantify the image distortions and later, corrections. It is given by the peak intensity of the seeing affected PSF core normalised to that of an ideally unaberrated PSF (based on theoretical considerations), obtained with the same instrument [36]. It describes which fraction of the light is concentrated in the diffraction-limited core and which fraction is spread into the seeing-limited halo, varying between 0 and 1. Logically, it equals 1 for an image not affected by seeing and the lower SR the lower the SR the poorer the image quality.

$$SR = \frac{PSF_{seeing}(0, 0)}{PSF_{airy}(0, 0)} \quad (2.14)$$

In the K band ($\lambda = 2.0 - 2.4 \mu\text{m}$), the Strehl ratio of astronomical images is typically less than one percent under seeing-limited conditions and can be increased up to $\approx 70\%$ with the use of a classical AO system or even up to 99% for eXtreme Adaptive Optics (XAO). It will depend largely on a number of parameters, such as the brightness of the reference star and the AO type.

Additionally, another quantity is defined to indicate the signal quality on the detector: SNR. The source radiation is considered as the “signal”. The “noise” is a radiation flux which only partially depends on the astronomical source, but it mingles with the signal, reducing the image quality which can be obtained with an optical system. The biggest contributors to noise are the Poissons’s noise, a contribution typical of photon nature, sky background, airglow, or thermal noise intrinsic to the optical system and detector associated noises: read-out-noise, dark current, spatial non-uniformity pattern noise.

As a final note, it is important to understand the distinction of AO performance at different wavelengths. As stated in the above mentioned equations, most seeing parameters depend on $\lambda^{6/5}$. The seeing disk has a size $\lambda/r_0 \propto \lambda^{-1/5}$ while the diffraction-limited disk has a size $\propto \lambda/D$. Figure 2.6 illustrates the following point.

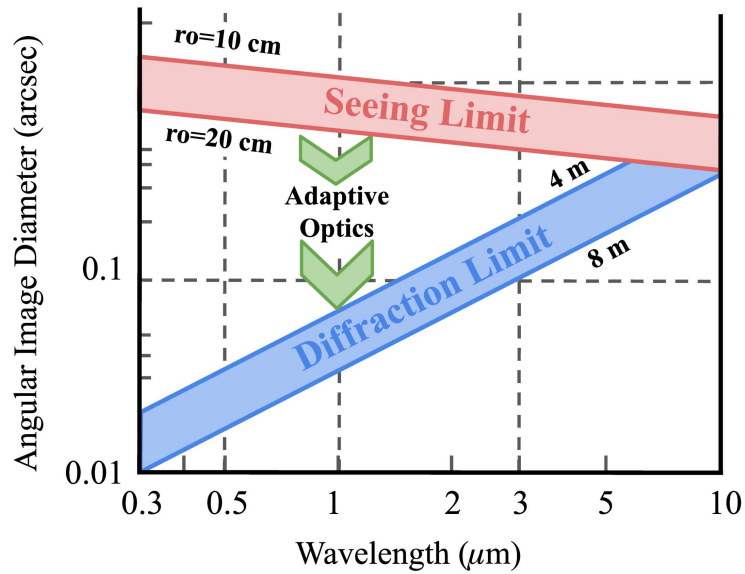


Figure 2.6: The difference in image resolution with and without AO corrections is shown in a plot of the image angular diameter as a function of wavelength (μm). Across all wavelengths, AO has the ability to reduce the seeing of seeing limited images and reach resolutions closer to the diffraction limit. However higher wavelengths are not so greatly affected by seeing such that even uncompensated telescopes are close to the diffraction Limit. Hence, at shorter wavelengths, where seeing largely decreases the resolution, the potential usefulness of AO systems is higher. Image adapted from Hardy [2].

At visible wavelengths, there is larger gap between seeing limit and diffraction limit than for $\lambda \sim 10 \mu\text{m}$, where even large uncompensated telescopes are close to diffraction limited as they are not immensely affected by turbulence. The potential improvement and usefulness of AO is much greater at short wavelengths, but, coincidentally, it is also more difficult to implement in those ranges.

This is true due to several factors. First of all, shorter wavelengths lead to smaller isoplanatic angles and also to a reduced sky coverage (which can be about 20 times larger in the NIR). Secondly, the corrective optics needs to be more segmented and operate on faster timescales. Analogously, the wavefront sensor needs to sense the incoming signals at a finer angular scale, which can become very expensive and unpractical very quickly. Finally, the quality of the optical surfaces for a visible needs to be much higher.

Chapter 3

Adaptive Optics

The primary goal of adaptive optics (AO), as previously mentioned, is to mitigate the impact of atmospheric turbulence on data captured by large ground-based telescopes. This is achieved by correcting the incoming wavefront for the aberrations introduced in the optical path between a celestial object and the detector, resulting in a narrower, sharper, closer to diffraction-limited image. In practice, AO systems are often referred to as "seeing reducers" since complete elimination of atmospheric-induced aberrations is rarely attainable.

To do this, an AO system must fulfill three main steps:

1. Measure the wavefront disturbances of the signal of a Guide Source GS, using a Wavefront Sensor WFS;
2. Compute the corrections needed to compensate for the aberrations measured by the WFS, in real time. This is done using a very fast computing unit, called Real Time Computer (RTC), in which an intermediate step regarding wavefront reconstruction is embedded;
3. Insert a path length correction in the optical path of the incoming light to compensate in real time for the aberrations, using an element called wavefront corrector (usually a Deformable Mirror DM).

The working principle of an AO system is illustrated in Figure 3.1. This configuration was first used in the RTAC (Real Time Atmospheric Compensation) system [37] and is now still used in most systems and is referred to as Single Conjugated Adaptive Optics (SCAO).

There are two different ways in which corrections can be performed in AO: open-loop and closed-loop. In an open-loop, the perturbed wavefront reaches the WFS before the DM. The received wavefront is measured in its uncorrected state, corrections are then computed and fed to the DM. A more efficient configuration is the closed-loop, where instead light reaches first the DM and then part of the light is diverted toward the WFS to estimate the residual aberrations which remain to be compensated. This increases the efficiency of the adaptive optics system and reduces at each iteration the correction residuals. In both configurations, corrections have to be made in a time frame faster than the Greenwood frequency, so that they are made at least at the same timescale as the evolution of the turbulence.

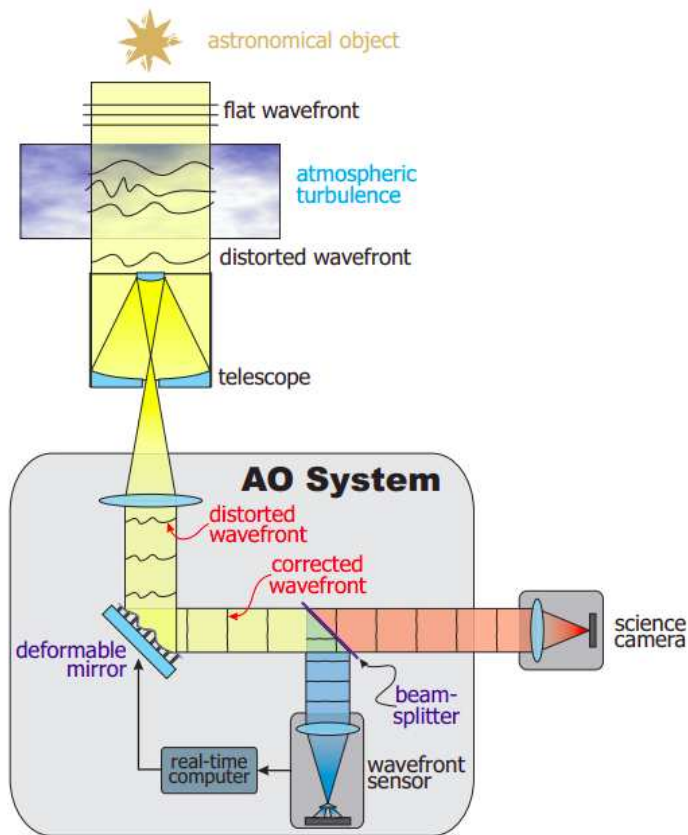


Figure 3.1: The components of an AO System are shown, in a closed-loop configuration. As distorted wavefronts enter the telescope optics, they encounter the deformable mirror (DM), which corrects the wavefronts. Then, part of the light is diverted towards the wavefront sensor (WFS) to measure the residual aberrations, while the rest continues to the science camera. The WFS senses the wavefronts and sends the information to the real-time computer (RTC) who computes the necessary adjustments to be sent to the DM. Image from Sebastian Egner's PhD thesis [3].

3.0.1 Reference Star

A key aspect of AO is the need for a reference or guide source to sense wavefront aberrations, light that traverses the same optical path as that of the object being observed. Hence, bright point sources close to the scientific target are required to achieve optimal corrections. Naturally, stars are possible references, from now on named Natural Guide Stars NGS for obvious reasons. These references limit observations to the vicinity of the brightest stars, that is, a few percent of the sky. Wavefront sensing is also possible with extended sources, but preferably small sources, provided they are bright enough. An alternative to NGS has been developed in AO research, which is the use of artificial stars. Lasers positioned close to the telescope are employed to stimulate a portion of the upper atmosphere and create an artificial guide star on the side of the scientific object. References created in such a way are called Laser Guide Stars.

3.0.2 Wavefront Sensor

Consider a wavefront $W(x,y)$ which has crossed a turbulent atmospheric layer and which we want to characterise. Some WFS will sense the wavefront gradient ∇W , such as the Shack-Hartmann WFS (SH-WFS) and Pyramid WFS (P-WFS), while others sense the curvature $\nabla^2 W$, such as the curvature WFS. Generally, the wavefront that enters through the telescope aperture is divided in smaller regions of the order of r_0 , called subapertures, in order to identify high order aberrations and reconstruct the tilt of each section of the entire wavefront. In theory, we can recover the entire profile of $W(x,y)$ by accurately sampling the aperture; however, there are limitations imposed to the number of subapertures by:

1. The seeing conditions, dictated by r_0 : the optimal number of subapertures for spatial sampling system will be $N \approx D/r_0$, because at finer scalar than r_0 the wavefront can be considered unperturbed;
2. The signal to noise ratio SNR of each sub-aperture: since telescopes operate in photon-starving mode most often, the number of incident photons for each sub-aperture can become too low, if the pupil plane sampling is too high;
3. The number of available actuators M to perform correction: typically AO systems will have 1 actuator per sub-aperture, there is no point in having $N \gg M$ if there aren't enough actuators to apply the corrections. In order to take advantage of sampling at high spatial frequencies, $N \approx M$.

Wavefront variations at scales smaller than the subaperture size are lost in this process. To estimate the inclination/tilt in each sub-aperture a simple concept is used: tilts in the pupil-plane correspond to displacements in the focal-plane. Typically, the displacement is calculated by measuring light intensity differences or the center of mass shifts of the focal-plane image of each sub-aperture. Let's illustrate this concept by taking the most simple WFS, the Quad-Cell WFS.

Quad-Cell WFS

A Quad-cell WFS consists of four adjacent quadrants such that the centre where they meet corresponds to the position in the optical path where the centre of the image should lie in the absence of tip-tilt. Each quadrant measures the intensity of light it receives, A, B, C and D , which corresponds to a fraction of the entire image spot, depending on its displacement and size. If the imaged spot is centred, all quadrants receive $1/4$ of the total light and $A = B = C = D$. Shifts along the x axis and y axis are quantified through the signals S_x and S_y :

$$S_x = \frac{(B + D) - (A + C)}{A + B + C + D} \quad S_y = \frac{(A + B) - (C + D)}{A + B + C + D} \quad (3.1)$$

These signals are proportional to the wavefront slope ∇W . The range in which S_x and S_y increase linearly is the most useful for determining tip-tilt. This range is achieved when the spot illuminates all four quadrants. If this is not the case, saturation will occur. The S_x signal behaviour as a function of the shift of the spot along x axis is plotted on the right side of Figure 3.2. In the y direction there is an analogous behaviour. The linear range and the saturation range are identified there. It is important to note that the sensor sensitivity

increases as the spot size decreases. This is because, for the same amount of centre of mass shift, the signal will vary by a greater percentage when the spot is smaller.

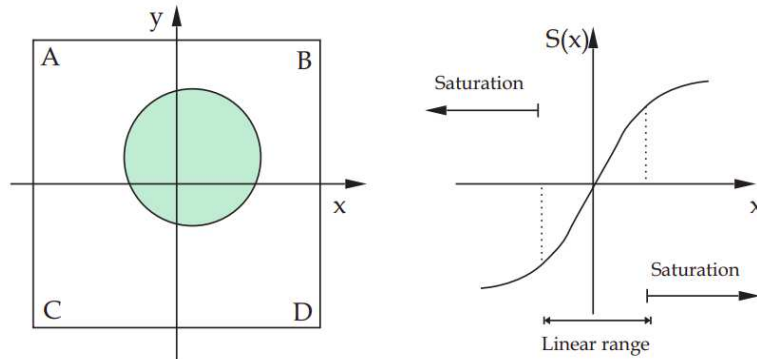


Figure 3.2: The quad-cell concept is illustrated. The image spot is focused onto a four quadrant detector, that splits the light into four signals A,B,C,D. proportional to the area of the spot covering each quadrant. Then, using Equations 3.1 the shifts along the x and y axis are computed and the local tip-tilt is retrieved. Image from Maria Bergomi's PhD thesis

This concept can be used to sense the tip-tilt of the wavefront passing through the telescope aperture D or for sensing higher-order aberrations inside the subapertures, and thus is incorporated in the SH-WFS and the P-WFS.

Shack-Hartmann WFS

This sensor is based on the Quad-Cell concept to measure tip-tilt but applied locally to measure high-order aberrations. The telescope exit pupil image goes through a collimator and is projected on an array of identical small lenses (lenslets), located in a plane conjugated to the pupil one [38]. These lenses, placed adjacently and covering the entire aperture, divide the wavefront to obtain the required spatial sampling. The light of a single reference source is divided in more parts which are focused separately by each lens as shown in Figure 3.3, producing an array of images on the focal plane. There, a detector, typically a CCD, records images in order to reconstruct the centre of mass shift of each subaperture, following the Quad-Cell concept. As many Quad-Cell WFSs as the total number of spots (corresponding to the lenslet number in the array) are positioned in the focal plane. If the wavefront is perfectly flat and its inclination is zero, each spot's barycenter will be focused on the optical axis of the corresponding lens, but if, on the contrary, the wavefront is perturbed, the image focused by each lens will move on the focal plane, accordingly to the local inclination of the wavefront itself.

Pyramid WFS

The concept of the P-WFS was proposed by Roberto Ragazzoni in 1996 [39]. In a pyramid sensor, the light of the guide star is focused onto the tip of a glass square-based pyramid placed in a focal plane of the system. The four facets of the pyramid split the light into four beams, like the four areas of the Quad-Cell WFS, but due to refraction these four beams spread apart. The beams are then imaged onto a detector placed on the pupil plane with a relay lens, as shown in Figure 3.4, creating 4 pupil images that are divided in subapertures depending on the pixel-separation of the detector.

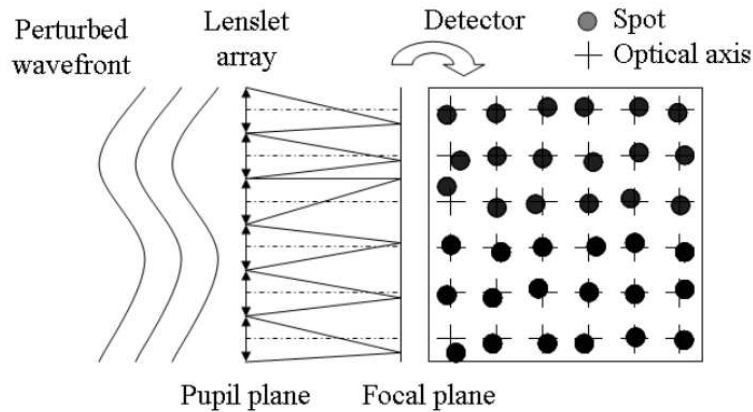


Figure 3.3: The Shack-Hartmann WFS concept is illustrated. A lenslet array is placed on the pupil plane to sample the incoming wavefront. From each subaperture thus created, an image spot is focused onto a detector on the focal plane. Using the quad-cell concept the mean tip-tilt is retrieved to reconstruct higher order aberrations. Image from Valentina Viotto's Phd Thesis [5].

If the wavefront is flat, then the light is split into four beams with equal amounts of light in each corresponding sub-aperture, and also globally in every pupil. In the presence of wavefront aberrations, however, the shape of the PSF on the tip of the pyramid is changed, and thus the distribution of the light into the four beams changes. In the simple case of a pure tilt, the focus of the light is shifted onto one facet of the pyramid, and hence each beam yields an intensity proportional to the number of photons that hit the respective face of the pyramid.

The average slopes of the wavefront $W(x, y)$ over the subaperture at position (x, y) can then be calculated from the intensity distribution $I_i(x, y), i \in \{1, 4\}$, in the corresponding pixels in the four pupil images. One of the main advantages of the P-WFS is that the subapertures are defined at the level of the CCD. Therefore, by changing the binning of the CCD, the observer can change the spatial sampling, without changing any optics.

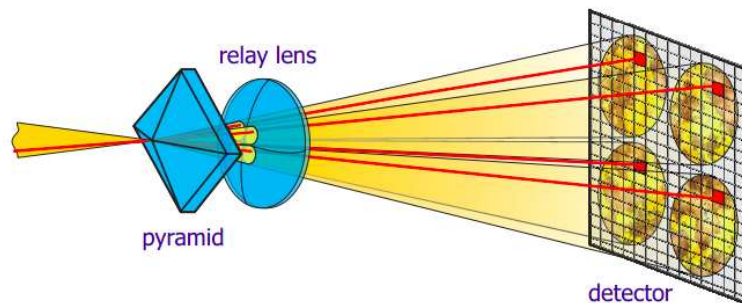


Figure 3.4: The Pyramid WFS concept is illustrated. The tip of the pyramid is placed on the focal plane, where the light of the guide star is focused. The four faces split the light into four beams which are imaged onto a detector placed on the pupil plane by a relay lens. The light distribution across the four pupil images is used to calculate both the tip-tilt and the higher order aberrations, if the operations are performed pixel wise. Image taken from Sebastian Egner's PhD thesis [3].

3.0.3 Real Time Computer: Wavefront Reconstruction

The WFS measures the local tilt of the wavefront in each subaperture, but this divides the sensed wavefront into contiguous zones where the relative phase between each is lost. The role of the reconstructor, schematised in Figure 3.5, is to stitch the individual slopes together, retrieving the relative phase over the full aperture and having a continuous 2D function of the sensed wavefront $W(x,y)$.

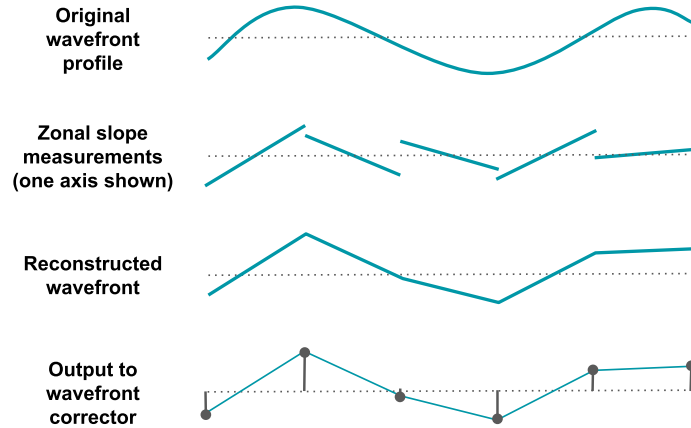


Figure 3.5: The wavefront reconstruction process is described, using the zonal mode. The WFS measures the local tip-tilt in smaller apertures, dividing the original wavefront. In this process, the relative phases between contiguous zones is lost. These are retrieved to obtain a continuous reconstructed wave profile. Then, the RTC computes the voltages that the DM actuators must have to correct for this wavefront profile. Image adapted from Hardy [2].

Wavefront reconstruction involves a heavy data processing load, as it is a two-dimensional process. For an aperture containing N local tilt samples, there are approximately N x-gradient measurements and N y-gradient measurements. To obtain each reconstructed point, all $2N$ gradient values are weighted and summed. The reconstruction process, similar to a matrix inversion algorithm, involves a total of $2N^2$ multiplication / addition operations, which must be performed in a small fraction of the turbulence change time, usually less than $1ms$ [2]. Afterwards, commands are sent to the DM to apply the necessary corrections.

There are two methods of specifying the wavefront reconstruction function in a two-dimensional aperture: zonal or modal mode. When the wavefront is expressed in terms of the gradients over small spatial areas, or zones, that divide the aperture, the approach is called zonal. The zonal mode has been described thus far. When the wavefront is expressed in terms of coefficients of the modes of a polynomial expansion over the entire pupil, it is said to be modal. The modal mode treats the wavefront as a superposition of suitable basis functions $Z_i(x, y)$, weighted with coefficients c_i :

$$W(x, y) = \sum_i c_i Z_i(x, y) \quad (3.2)$$

For the description of the atmospheric turbulence, the most commonly used functions in optics are the Zernike polynomials for circular apertures. A review of the properties of the Zernike polynomials relevant to the purpose of describing an atmospherically distorted wavefront can be found in a paper by Noll [40]. They form an orthogonal basis for the

functions defined on a unit circle, and can be mathematically represented in polar coordinates (r, θ) in the following way:

$$W(r, \theta) = \sum_n C_n^m Z_n^m(r, \theta) \quad Z_n^m(r, \theta) = r^n \cos(m\theta) \quad (3.3)$$

where the Z_n^m are the Zernike polynomial terms of radial order n and azimuthal frequency m and C_n^m are the respective linear combination coefficients. An advantage of using the Zernike polynomials is that each of them describes a known optical Seidel aberration. The model reconstruction approach has been shown to be superior in terms of error propagation and computational time [41].

In summary, the RTC receives from the wavefront sensor the local gradient of the wavefront calculated on subapertures conjugated with the pupil of the telescope. One of the processes performed by the RTC is the reconstruction of the wavefront profile. The RTC converts the WFS measurements, that are the spatial derivatives of the wavefront, in a matrix of coefficients of Zernike polynomials C which maps the wavefront. This is the modal reconstruction approach: the wavefront is now defined by a proper polynomial expansion on Zernike polynomials with the appropriate coefficients. Once the wavefront map is constructed, it is necessary to compute how to correctly shape the wavefront corrector to reduce the present aberrations.

3.0.4 Wavefront Corrector

The wavefront corrector is typically composed of two parts: a flat mirror that is mounted on a stage that can tilt in two perpendicular directions to eliminate tip-tilt, and a deformable mirror DM, which is an optical surface that can be adjusted locally by pushing and pulling M actuators beneath the mirror, thus correcting for higher-order aberrations.

The desired shape of the DM (equal and opposite to $W(x, y)$) that will apply the necessary corrections is $S_{DM}(x, y)$ and is generated by applying the proper amplitude A_i to M actuators. The effect of each actuator on the surface $P_i(x, y)$ is its influence function. Then,

$$S_{DM}(x, y) = \sum_{i=1}^M A_i P_i(x, y) \quad (3.4)$$

is the set of linear equations that can define the desired mirror shape. The actuator commands V , a vector of M voltage values, are then derived from the actuator amplitude A_i , by relating it to the suitable gain factors and voltage conversions [42].

To correct the wavefront shape in the modal approach, it's necessary to precisely know which actuators have to push and pull to reproduce each aberration shape at the level of the DM. In general, acting on one actuator modifies all the WFS signals (N measurements) and hence a calibration phase is required, to obtain an $M \times N$ interaction matrix I translating the reconstructed wavefront signal S_{DM} to the signal V to be sent to the deformable mirror actuators. This computation is part of the RTC routine calculations.

$$V = I \times S_{DM} \quad (3.5)$$

As mentioned in the beginning of the chapter, in closed-loop systems the WFS senses the residual aberrations on the wavefront after passing through a corrective element. In fact, a closed-loop system aims to minimise the residual aberrations of the wavefront, S_{res} , resulting

from the current DM disposition, given by

$$S_{res}(x, y) = W(x, y) - S_{DM}(x, y)$$

Therefore, in reality, the WFS will measure S_{res} and the RTC will compute the voltage vector of adjustments to apply to the DM.

3.1 Adaptive Optics Limitations

Up to now we have implied that adaptive optics system can reduce the seeing and bring images closer to the diffraction-limit of the parent optical system, but this depends on the quality of the phase conjugation applied to the beam (among other factors). Hence, the performance of an AO system will depend on the quality of the wavefront measurement, speed and robustness of the reconstruction process and the ability to reproduce the wavefront corrective surface. The main errors that negatively affect the corrections are:

- Sampling error

As briefly mentioned, aberrations on a spatial scale smaller than the subaperture sampling of the telescope pupil will go unnoticed. The precise compensation at all spatial frequencies is very difficult to obtain, and the decision on the number of samplers and actuators must be made according to each system specific requirements. It has been demonstrated by Beckers [43] that the sampling error for a starting turbulence with a Kolmogorov spectral distribution is:

$$\sigma_{spatial}^2 \approx 0.34 \left(\frac{r_e}{r_0} \right)^{5/3} \quad (3.6)$$

where r_e is the distance between actuators. This variance is often also referred to as wavefront fitting error.

- Timing or latency error

This error is due to the time delay between the measurements of the WFS and its effective correction by the DM and we take a simple form to express it:

$$\sigma_{time}^2 = \left(\frac{\tau}{\tau_0} \right)^{5/3} \quad (3.7)$$

where τ_0 is the coherence time and τ is the "dwell time" defined as the time elapsed between the wavefront measurement and its correction [43, 1] To obtain an efficient correction, the system should work at higher frequencies than the frequency of the evolution of the aberrations.

- Anisoplanatism

Having defined the isoplanatic angle θ_0 as the angular size of the portion on the sky around the guide star where the atmospheric aberrations vary less than 1 rad, outside this area atmospheric turbulence is considered decorrelated. The light cylinders corresponding to the science target and the guide star pass through different parts of

the atmosphere that distort the two beams in different manners, as depicted on Figure 3.6. The consequence is that the wavefront corrections achieve the highest SR for angles smaller than θ_0 and as the angle increases, SR decreases. In order not to excessively degrade the SR, it is necessary that the scientific object and the guide star be separated by less than θ_0 , which is of the order of a few arc seconds for IR and visible ranges. According to Fried [44],

$$\sigma_{aniso}^2 = \left(\frac{\theta}{\theta_0} \right)^{5/3} \quad (3.8)$$

As an example, Roddier [32] treats the case for a source on the edge of the isoplanatic patch, $\theta = \theta_0$, for which the SR decreases by 62% at $\lambda = 0.5 \mu\text{m}$ for $D/r_0 = 10$.

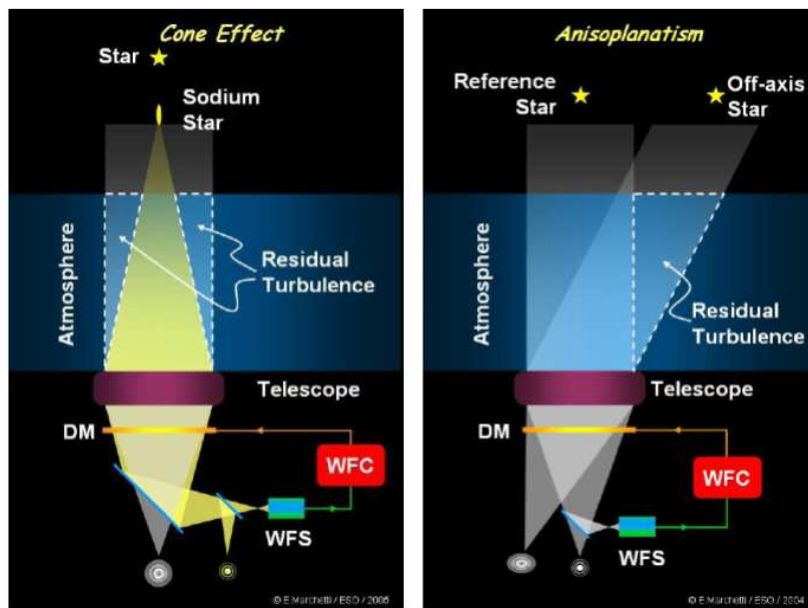


Figure 3.6: **Left:** Image shows the anisoplanatism effect leading to a degradation of the correction, in a SCAO system. The turbulence sensed by the WFS doesn't match the turbulence corrected by the DM. The highest SR is achieved inside the θ_0 , close to the reference star. The further away from it the worse is the SR. **Right:** Image shows another degrading effect: the so-called cone effect or focal anisoplanatism. It takes place, again, due to a mismatch between the volume of atmosphere sensed with the LGS and the volume corrected for the science target. The lower the altitude of the LGS, the bigger is the impact of this effect. Images taken from ESO.

- Limited sky coverage

As a consequence of anisoplanatism, the limited separation between guide star and science target reduces the sky region where sufficiently bright natural stars can be found. The limiting magnitude stars that makes them potential guide star varies from 14 to 17 magnitudes in the V band. Obviously, the sky coverage changes in different areas of the sky, since the probability to find a suitable reference depends on the galactic coordinates of the region. In particular, the lowest sky coverage occurs at the galactic poles (0.1% in the V band and 0.5% in the K band), since the statistical density of stars is lower than in all the other directions. On the other hand, the maximum

sky coverage will be given for the galactic equatorial areas (1% in V band and 4% in K band). Generally speaking, for efficient correction at visible wavelengths, this sky coverage has been found to be lower than 1 percent, reducing drastically the potential application of AO [45].

These severe limitations lead, in the last couple of decades, to the idea of using a laser to create an artificial reference star in the direction of the observed object, hence increasing the sky coverage. Additionally, the idea of designing a system with more reference stars and more DMs was also developed. Such AO system is named Multi-Conjugate Adaptive Optics and aims at reducing the impact of anisoplanatism.

3.1.1 Laser Guide Stars

Since the early 1980s, researchers within the U.S Air Force [46], in parallel with the astronomy community, namely Foy and Labeyrie [47], have investigated the use of artificial guide star techniques to sample the atmosphere. Lasers positioned closed to the telescope are employed to stimulate a portion of the upper atmosphere and create an artificial guide star on the side of the scientific object. References created in such a way are called Laser Guide Stars (LGS) and at the moment two main types have been widely studied and implemented:

- Rayleigh LGS [48]: Rayleigh scattering can create sources of light in the stratosphere at around 8-12 km altitude.
- Sodium LGS [49]: Resonant backscatter in the mesospheric sodium layer at ~ 92 km might be used to produce a guide star well above most of the turbulent atmosphere.

It was realised from the start that using a single low-altitude Rayleigh LGS was inefficient because turbulence below the beacon is sampled only in a cone-shaped volume, and above, where a lot of turbulence originates, it is not sampled at all. This disadvantage covers both types of LGS but is specially harmful for Rayleigh LGS. Using multiple beacons within the beam can improve sampling efficiency but a lot of work needs to be done to merge the information from multiple sources and tomographically reconstruct a three-dimensional map of the atmosphere.

The main advantage of sodium LGS is the reduction in the focal anisoplanatism (caused by the above mentioned cone-shaped volume, or cone effect) compared to that encountered with low-altitude Rayleigh LGS. Focal anisoplanatism is one of the main drawbacks of LGS and it is due to the fact that the wavefront of a star and of a LGS do not cross the same atmospheric turbulence, as illustrated on Figure 3.6. A real star has a flat wavefront that covers a cylindrical volume of the atmosphere but an artificial star has spherical wavefronts and span a conic volume all the way down to the telescope diameter. The atmospheric volume that is not sampled by the conic volume grows as the altitude H of the LGS decreases. The mean square focal anisoplanatism error is given by [32]:

$$\sigma_{FA} = 0.172 \left(\frac{D}{\theta_0 H} \right)^{5/3} \quad (3.9)$$

We can see that for a site with $\theta_0 = 3''$ at $\lambda = 0.5 \mu\text{m}$,

$$\frac{\sigma_{FA}^2(\text{Rayleigh beacon}, H = 20 \text{ km})}{\sigma_{FA}^2(\text{Sodium beacon}, H = 90 \text{ km})} = 12.7$$

This translates to the fact that for large telescopes, sodium beacons have a considerable advantage over Rayleigh beacons. Although the laser requirements for sodium are more stringent in terms of wavelength and pulse width (to avoid saturation ¹), sodium beacons appear to be the preferred approach for astronomical adaptive optics. For the purpose of this thesis, Sodium LGS will be further detailed.

Sodium LGS

Atomic sodium resultant of meteoric disintegration remains at an altitude between 89 km and 92 km, since at this altitude the conditions prevent molecular reactions. By exciting a small volume of sodium, a luminous source can be created, using radiation of $\lambda = 589.2$ nm, corresponding to the D_2 transition from the $3^2S_{1/2}$ state to the $3^2P_{3/2}$ [50]. A single guide star is limited to a flux of about 1.9×10^8 photons per second but the detected sodium photon flux will depend on the sodium column density characteristics which can vary on a seasonal or diurnal or a short 10 minutes scale. A full treatment regarding the photon flux can be found at Tyson et al. 1998 [42]. Studies by Gardner et al. [51],[52] have revealed important characteristics of the sodium layer: the layer centroid average height has been measured to be approximately 92 km above mean sea level (MSL) and the average thickness of the layer about 10 km FWHM. In addition, variations of over 200% in abundance, 2 km in centroid height and 1 km in root-mean-square (rms) width have been observed within the time span of a few hours during the night. In general, these LGS have magnitudes ranging from +5 to +12 [2].

Sodium LGS aren't a flawless solution. Due to their intrinsic nature and geometry, a few drawbacks can be pointed out:

- The turbulence on atmospheric layers above the LGS cannot be sensed. For this matter, Sodium LGS are already an improvement relative to Rayleigh LGS.
- The above mentioned cone effect cannot be fully eliminated and is specially harmful for the AO performance as the telescopes get bigger.
- LGS do not allow to determine the tip-tilt because the beam in its travel forth and back from the laser source to the detector, passes twice through the same atmosphere portion, in a time interval which is lower than the mean time scale of the variation of mean inclination introduced by the atmosphere to the wavefronts. The resulting tip-tilt is close to zero. To solve this problem WFSs coupled with NGS need to be used together with LGSs, to measure absolute tip-tilt [45]. This brings back to the original problem of NGS, the anisoplanatism. Fortunately, the guide stars used for tip-tilt correction do not have to be as bright as the guide stars used for correction of higher order effects.
- These sources are located at a finite height and usually telescopes are designed to focus sources at infinity. This fact introduces large static aberrations which, even if they can

¹Pumping of sodium atoms by the laser from the ground state into an excited state can lead to a population inversion, if the population of excited atoms is large. In that case, the incident light produces stimulated emission in the forward direction and such emission is lost to the telescope. This condition is known as saturation and it limits the laser power that can be used efficiently.

be characterised and removed from the retrieved wavefront shape, can saturate the WFS.

- The height, density, and thickness of the sodium layer vary seasonally and also during the same night, causing a defocus problem on WFSs designed to sense NGSs [53].
- Due to the thickness of the atmospheric sodium (about 10 km), the artificial source cannot be considered as a point-like source but more as an object extended in a 3D volume. When seen from different telescope's apertures, the LGS spot is differently elongated. This problem, known as "spot elongation", will be even more evident for future ELT-class telescopes.

The importance of the last two restrictions to this dissertation is such that we will now delve deeper into the extended nature of the Sodium LGS.

For the reasons mentioned above, the LGS is an extended elongated object with a given orientation in the sky, and also with a certain light density profile along its extension. A focal plane WFS like the SH-WFS or a pupil plane one like the P-WFS is prepared to sense a single focused spot of the GS. Instead with a LGS, the spot will be only partially in focus, since the source extension along the optical axis is not negligible with respect to the LGS altitude [54]. In particular, when trying to select the best focal plane orthogonal to the chief ray, only the central part of the source will be actually in focus, while its edges will be defocused [54], as shown in Figure 3.7.

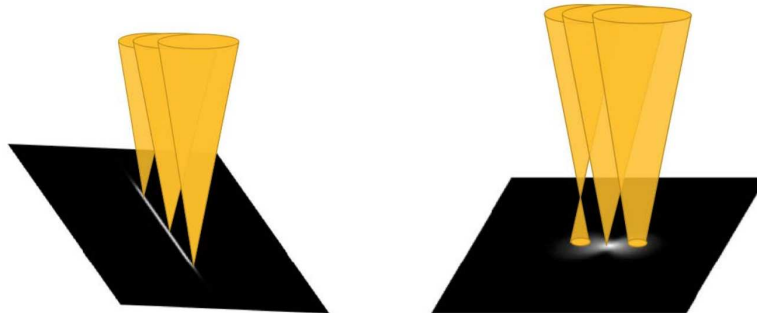


Figure 3.7: An object with an extended nature will result in an image only partially in focus on a plane orthogonal to the chief ray. **Right:** Only the central part of the source will be actually in focus while its edges will be defocused. **Left:** There is a plane where the light coming from different pots of laser beacon can be equally in focus. Image taken from Simone Di Filippo's PhD thesis [6].

For example, on a 40 m telescope every meter of change of the sodium layer mean altitude translates into ~ 7 nm of defocus (wavefront error rms) [55]. For the above mentioned variation of 2 km in altitude, a $14 \mu\text{m}$ defocus should be expected, which is a non negligible value to take into account.

Let's continue with the comparison with the SH-WFS, that for instance is the current baseline for the LGS WFS for the future ELT AO instruments. The LGS spots appear elongated in the subapertures located far away in the limit of the pupil with respect to the laser launcher position. This issue named spot elongation translates into a decrease in the sensitivity of the signal of the local wavefront first order derivative on classical WFS, which will then be dependent on the sub-aperture position on the pupil and on the LGS orientation. The differential elongation along the telescope pupil is illustrated on Figure 3.8.

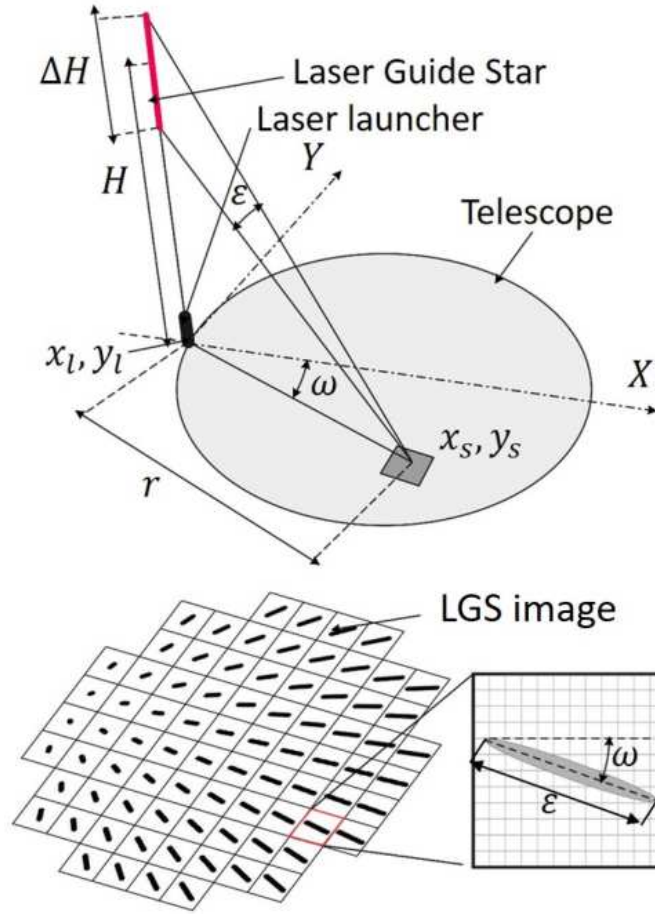


Figure 3.8: The LGS spots appear elongated in subapertures far from the Laser Launcher Telescopes (LLT). For a LLT on the edge of the telescope's aperture, at position (x_l, y_l) , the elongation ϵ at a subaperture (x_s, y_s) is given by Equation 3.10. It depends on r , ΔH , H and $\cos(\xi)$, respectively the distance from the subaperture to the LLT, the width and height of the LGS on sky, and ξ the zenith angle. Image taken from Lombini et al. 2021 [7].

The elongation points at the laser launch location and its extension ϵ increases with the distance r from the launcher itself. Depending on the Sodium layer mean altitude H , vertical extension ΔH and zenith angle ξ , ϵ can be approximated by [7]:

$$\epsilon \approx r \frac{\Delta H}{H^2} \cos(\xi) \quad (3.10)$$

On a 40 m diameter telescope, assuming a mean height $H = 92$ km and $\Delta H = 10$ km, the spot elongation may be 6.5" for a LGS launcher located at the center of the telescope aperture (e.g. behind the secondary mirror). The elongation is doubled in case of laser beams projected from the edge of the telescope aperture [56]. In the worst case scenario, i.e. in the furthest sub-aperture from the laser launch telescope, the elongation ratio between the long axis and the short axis of the spot is so high that the photon noise variance is ~ 600 times larger along the long axis, resulting in a differential SNR.

Moreover, beyond a degraded SNR, the spot elongation yields a bias in the reconstructed

wavefront when the spots are truncated and not properly sampled. In recent studies of WFS suitable for the ELT, the available cameras do not seem to have enough pixels to provide good sampling of the most elongated spots without truncation [57].

Evidently, LGS have the possibility of improving sky coverage of scientific observations, enabling different astronomical targets to benefit from AO corrections. However, the limited isoplanatic angle is still an obstacle to achieve AO corrections over a wide FoV, which is of interest to many other scientific applications. For that purpose, Multi-Conjugate Adaptive Optics Systems have been developed and are already showing prominent results. The next section is dedicated to them.

3.1.2 Multi-Conjugate Adaptive Optics

Multi-Conjugate Adaptive Optics (MCAO) technique was initially introduced by Beckers in 1998 [58] and it is based on the concept of using more than one guide star as a reference. It was thought as a means to increase the area of useful correction, which greatly limits several scientific cases. MCAO systems use multiple guide stars to measure the distortions induced by the individual turbulent atmospheric layers, as opposed to SCAO where a single guide star (let's say, for example, a NGS) gives a depth of focus which is infinite. In fact, if more references are used, the FoV increases, the depth of focus decreases and because of this an WFS allows to focus at a given altitude and sense the turbulence inside a specific turbulent layer. Naturally, more than one DM must be introduced if the number of atmospheric layers to be corrected increases (ideally one DM for each layer). The choice of the layers to be correct can be tuned to the site's seeing characteristics, by identifying the heights where strong turbulent layers are present. Usually, these are seen as peaks in the C_n^2 profile. Generally speaking, however, the ground layer is the strongest source of turbulence.

It has been shown that the ground layer correction alone (MCAO removing only the ground layer is called the Ground Layer Adaptive Optics (GLAO) correction) can improve the FWHM of the PSF by a factor up to 2.5 in K band, reaching 0.2'' in a FoV up to 10' [59].

The complexity of building such a system is unimaginable but it is not an impossible feat. The first-ever MCAO system in the world was the Multi-Conjugate Adaptive Optics Demonstrator (MAD) [60], which was installed at the ESO's VLT facility in Chile. MAD was a pioneering instrument that aimed to demonstrate and test the capabilities of MCAO technology. It used multiple guide stars, including LGS. Later, in 2012, the first telescope equipped with MCAO system started science operations. The Gemini Multi-conjugate Adaptive Optics System (GeMS) at the Gemini South telescope in Cerro Pachon is the only currently working sodium-based multi-LGS AO system [61]. GeMS works with a LGS constellation of 5 stars. The MCAO module uses DMs conjugated to 0 km and 9 km. In the first year of operations, it was observed that, in 50% of the time, GeMS was delivering a FWHM of 75 mas (or better) in H band across a 85'' × 85'' FoV.

3.2 Ingot WFS: a Novel Concept for Elongated LGS

A Sodium Laser Guide Star (referred to as LGS hereafter) is not, in fact, a point-like star, as previously explained. Instead, it takes on a cylindrical form when observed in the sky. A more accurate description would depict it as a complex, time-varying 3D column. However, it's often colloquially referred to as "cigar-shaped" in literature.

Another consequence already mentioned is that when the LGS is viewed from different apertures within a telescope's pupil, it extends both angularly and radially from the observer. An example of the obtained image is shown on Figure 3.9. The elongation of the spot, as seen in WFS systems like the SH-WFS (or the P-WFS) causes a reduction in sensitivity to the local wavefront's first-order derivative. This reduction is dependent on the sub-aperture's position on the pupil and the LGS orientation. Trying to employ a conventional WFS, initially designed for unresolved stellar sources, with such a reference is a risky proposition, and claiming the solution is optimal becomes uncertain. In the following paragraphs we aim at better explaining the complexity of the situation.

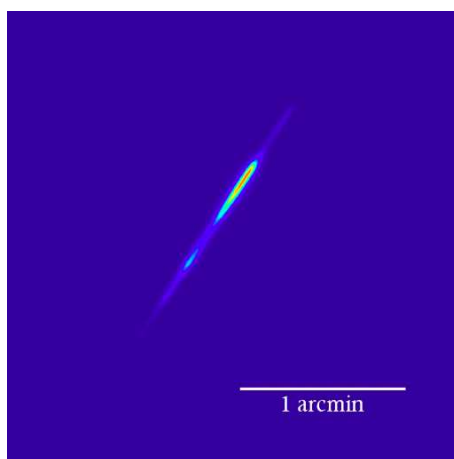


Figure 3.9: A sodium LGS elongated imaged as seen from the Jacobus Kapteyn Telescope. Image taken from Isaac Newton Group of Telescopes.

The *Scheimpflug Principle*, named after Scheimpflug T. [62] but introduced by Carpentier [63], defines the geometric relationship between the plane of focus, the image plane, and the aperture plane in an optical system when these planes aren't parallel. This principle is crucial to consider when dealing with optical systems involving non-parallel image and aperture planes, such as the case of the sodium laser guide beacon, which extends along a plane or line that is not aligned with the telescope's aperture.

Due to this, the resulting image formed by the optical system will also be projected onto a plane or line that is tilted relative to the telescope's usual focal plane. When a WFS is positioned along the nominal focal plane, it will intersect the image plane at a single point. However, only that specific point will be in focus, and everything else will appear defocused.

Figure 3.10 depicts on the left side the usual configuration of a telescope's image and respective conjugate plane of focus. The points \mathbf{i} and \mathbf{f} represent the initial and final edge of the sodium beacon on sky, while the remaining LGS extends in between them. The edges focus behind the aperture on points \mathbf{i}' and \mathbf{f}' . A classical focal plane WFS would be placed on either the plane passing through \mathbf{i}' or \mathbf{f}' but due to the LGS extension, the remaining image would be out of focus.

On the right side of Figure 3.10, the orientation of the planes according to Scheimpflug's principle are illustrated. An extended line from the image plane and another extended from the aperture plane meet at a line (in the 2D figure, only a point \mathbf{s} is shown, whereas the mentioned line is orthogonal to the page passing through \mathbf{s}) through which the optimal focus plane also passes. The LGS extends from \mathbf{i} to \mathbf{f} along the object plane and its focus is located along the optimal focal plane from \mathbf{i}' to \mathbf{f}' . In other words, the elongated cylindrical shape

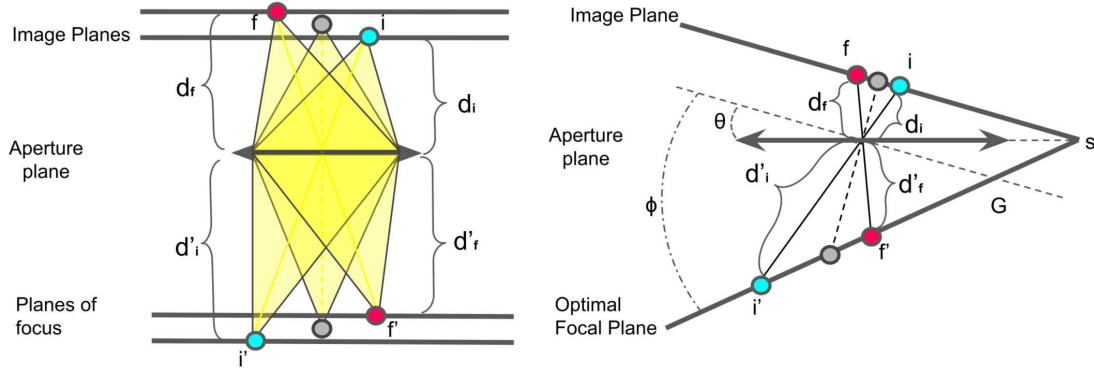


Figure 3.10: **Left:** An image composed of points f to i tilted with respect to the optical system's aperture, will come into focus at different parallel planes behind the aperture. Each point at distance d from the aperture focuses in a plane at a distance d' after the aperture. **Right:** An image composed of points f to i is position along a plane tilted by θ with respect to the optical system's aperture. According to Scheimpflug, there is a conjugate plane tilted by ϕ with respect to the aperture plane, where the image plane spots f - i can be in focus simultaneously, at positions f' - i' . This is called the optimal focal plane. The distances of the image points and focus points to the centre of the aperture are d and d' respectively. The three planes intersect at s .

of the sodium beacon has a corresponding three-dimensional focus on a plane tilted with a specific angle.

Taking advantage of this phenomenon, a new "z-invariant" WFS was proposed by Ragazzoni [20]. This concept involves a combination of refractive and reflective surfaces configured in a complex prismatic shape ("ingot") that extends through the focal volume. This design ensures a 1:1 correspondence between the source and the WFS, since the WFS is placed on the optimal focal plane given by the Scheimpflug principle. By utilising the 3D shape of the beacon, light fully focused along the prism can be split to select light from various parts of it. Each portion is directed onto a pupil image, potentially onto a common location for detection. This approach introduces a novel class of WFS based on the different possible ways of splitting the beacon.

Foreseen advantages of this WFS include efficient pixel occupation, significantly reducing the chance of spot truncation effects compared to the SH-WFS. Additionally, since the Ingot WFS operates in the pupil plane, it detects effects that wouldn't signal on subapertures, such as the "island effect". Finally, chromatic aberration issues related to the P-WFS are irrelevant due to the monochromatic nature of the sodium beam.

An initial design, illustrated on Figure 3.11, consists of a six-faced prism, each facing the incoming light with separate areas that deviate the incident beams through reflection and/or refraction. The six separate beams are then re-imaged into six corresponding pupils, similar to the P-WFS. Signals are obtained from the pupils in a manner akin to a 6-quadrant setup.

The drawback of this configuration is that when the sodium layer thickness changes and the source's actual size varies, the LGS image might no longer be able to align with the ingot prism geometry 3.11. Consequently, multiple ingot prisms would be necessary for a single I-WFS, selected based on sodium layer thickness, which is not practical.

To overcome this and other issues, further detailed in Ragazzoni 2019 [64], a possible different Ingot design has been investigated lately, and it will be described in the next section.

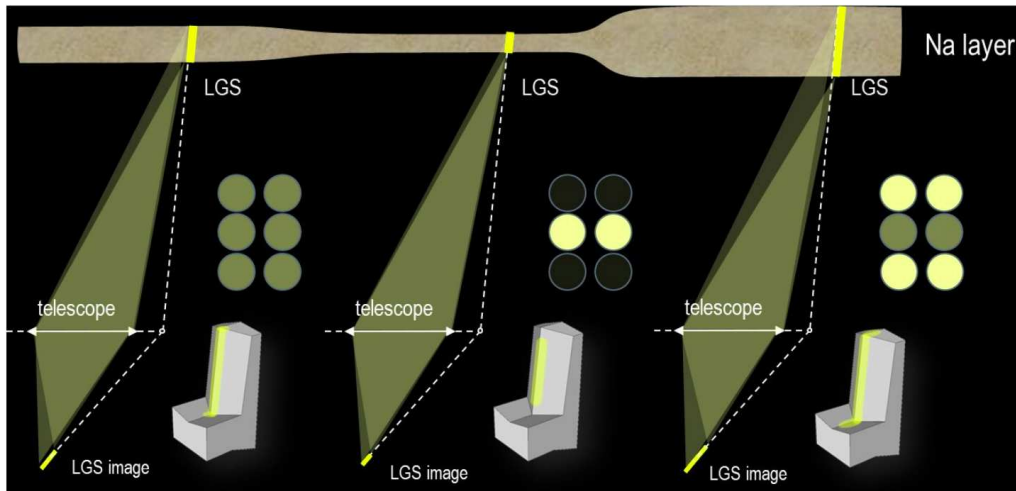


Figure 3.11: The initial design of the I-WFS consisted of a six-faced prism. This prism is placed on the best focal plane, behind the telescope aperture, where its six faces are illuminated by the LGS image, originating six pupils. Different sized prisms must be used to match the Na layer size variation so that enough light hits each surface and all the signals can be retrieved from the six pupils. Image taken from Simone Di Filippo PhD's thesis [6].

I-WFS Current Design

The new I-WFS design is composed of a reflecting roof with its edge positioned along the elongation axis of the LGS image, as shown in Figure 3.12. The roof is placed on the LGS image such that it can intercept only a portion of the LGS while the remaining portion of the LGS does not intercept the prism. This allows the splitting of the incoming LGS light into three beams, two reflected and the third which is passing unperturbed towards the following objective. These three separated beams are re-imaged in as many pupils at the conjugated plane, as shown in Figure 3.13. We call the transmitted pupil as A and the reflected ones as B and C, as shown in the same figure.

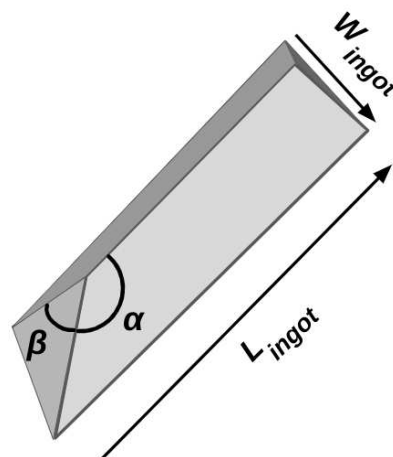


Figure 3.12: Schematic representation of the ingot solid shape and the parameters used to describe its geometry [8]. $\alpha = 83.63^\circ$, $\beta = 28^\circ$, $W_{ingot} = 10\text{mm}$, $L_{ingot} = 110\text{mm}$.

To take into account possible sodium layer thickness variations, which also result in a

sodium LGS beacon image extension variation, it is only necessary to have a roof prism long enough to accommodate the full length of the LGS image, even in the most elongated scenario.

Like in a P-WFS, the pupils are used to calculate signals proportional to the first derivative of the wavefront. In the following equation, we define the signals S_x and S_y along the x and y directions (x denotes movements orthogonal to the elongation direction, while y denotes movements along the elongation direction) as:

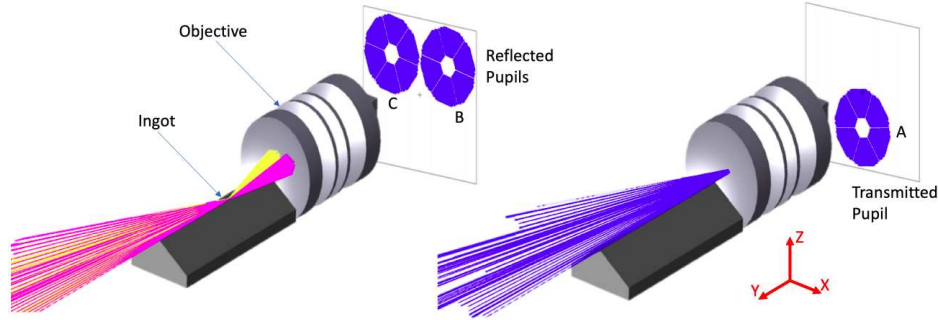


Figure 3.13: Conceptual layout of the ingot prism. Part of the LGS is focused by the reflecting ingot roof and forms two pupils, B and C (**left**), while the remaining part of the LGS is focused after the ingot (**right**) and is transmitted directly to the pupil re-imaging optics forming the third pupil.

$$\begin{aligned}
 S_x &= \frac{B - C}{A + B + C} - \frac{B_{ref} - C_{ref}}{A_{ref} + B_{ref} + C_{ref}} \\
 S_y &= \frac{A}{A + B + C} - \frac{A_{ref}}{A_{ref} + B_{ref} + C_{ref}}
 \end{aligned} \tag{3.11}$$

The operation is done pixel-wise such that a signal S_x and S_y is obtained for every pixel. Note that we subtract the reference signal (also called reference slope), which is the signal that we consider the zero point of our calibration. This "zero" reference condition accounts for any misalignment (starting position of the ingot for the LGS image) and any static aberration present in the optical path.

I-WFS specifications for the ELT

It is important to mention that by simple geometric considerations, the I-WFS concept is not suitable for a large telescope whose Laser Launcher Telescope (LLT) is located behind the secondary mirror [20]. As shown in Figure 3.14, when the LGS is projected along the line of sight of the telescope with the projector coaxial, the conjugated points are inbedded in each other's beams. However, as soon as the LGS is projected from aside the main aperture, the conjugation of the various points across the Sodium beacon are focused at independently located positions, without being embedded into adjacent ones.

The current prototype and design of the I-WFS was based on the ESO's ELT specifications. This includes the diameter of the telescope $D = 38.5$ m, the LTT distance from the center of the primary mirror of 21.5 m. According to these parameters and to the sodium layer characteristics, the LGS image is tilted with respect to a focal plane perpendicular to the optical axis by angle $\phi = 83.67^\circ$, as displayed on Figure 3.16. The new design was expected

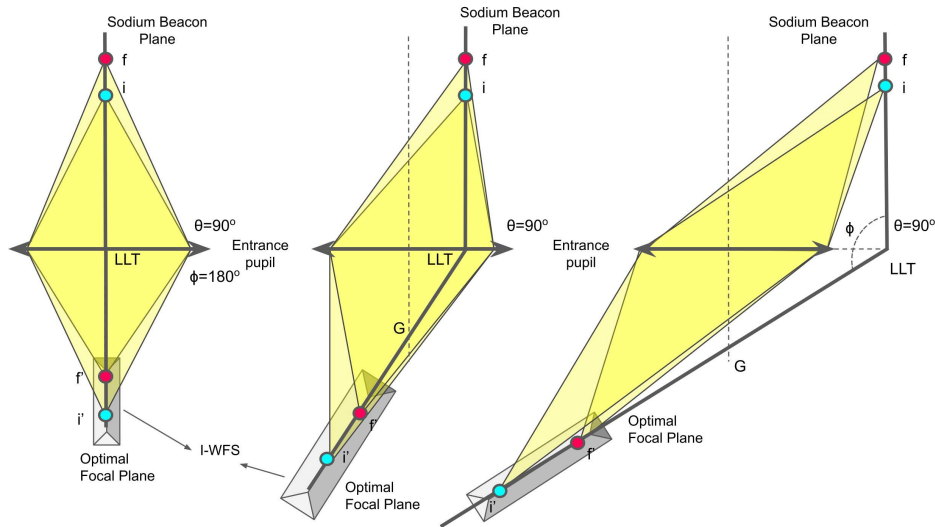


Figure 3.14: Scheimpflug's principle applied for different configurations of a telescope's optics, for a LLT perpendicular to the entrance pupil ($\theta = 90^\circ$). Illustrative schemes of how the LGS's light cones are intercepted by a I-WFS placed on the optical focal plane, as the LLT position changes with respect to the telescope's entrance pupil **Left**: LLT on the centre of the entrance pupil. **Centre**: LLT on the edge of the entrance pupil. **Right**: LLT outside the entrance pupil. A Sodium LGS is represented by its edges as points f and i , with respective focused image points f' and i' . Only when the LLT is positioned just outside the entrance pupil the I-WFS can be used properly, as the light cones of the LGS are no longer embedded onto each other.

to fulfil the following characteristics:

- Match the geometry of the LGS image and split the light at the level of the LGS focal plane into 3 beams, producing 3 images of the ELT entrance pupil
- Avoid overlapping of the output pupils
- Efficient light throughput

To achieve the proper separation of the three pupils, the roof prism has to be slightly tilted with respect to the LGS image plane, as illustrated by angle ω in Figure 3.15. Optical ray-tracing studies have confirmed that the overlap is solved when the prism is tilted by $\omega = 0.3^\circ$ from the perfect LGS focus position.

The size of the Ingot prism is chosen so as to accommodate the longest possible LGS image length. This happens when the sodium layer is the thickest, closest to the telescope, and the telescope is pointing at the zenith angle. Assuming a maximum sodium thickness layer of 20 km, a minimum height of 84 km and zenith pointing, the corresponding maximum LGS image length will be 107 mm using Equation 3.10. The expected maximum LGS spot size is 1.5", corresponding to an image width of 1.4 mm. Thus, using a prism roof 110 mm long and 4 mm wide should be enough to accommodate the biggest LGS image. The calculations performed to arrive to these parameters are based on the geometric relationships illustrated by Figure 3.16.

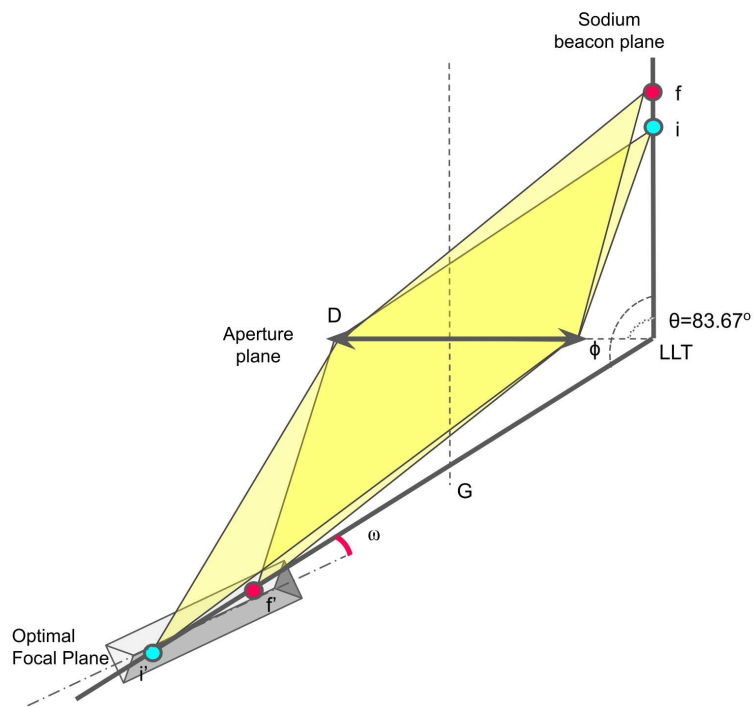


Figure 3.15: The Scheimpflug principle applied for the optical layout of the E-ELT, with the LLT placed outside the telescope's entrance pupil at a distance 21.5 m from its centre. A Sodium LGS is represented by its edges as points f and i , with respective focused image points f' and i' . The LGS image is tilted with respect to a focal plane perpendicular to the optical axis by angle $\phi = 83.67^\circ$. The light cones of the final and initial points of the LGS are shown, as they are focused onto a I-WFS placed on the optimal focal plane. In reality, the I-WFS is tilted by $\omega = 0.3^\circ$ from the optimal plane.

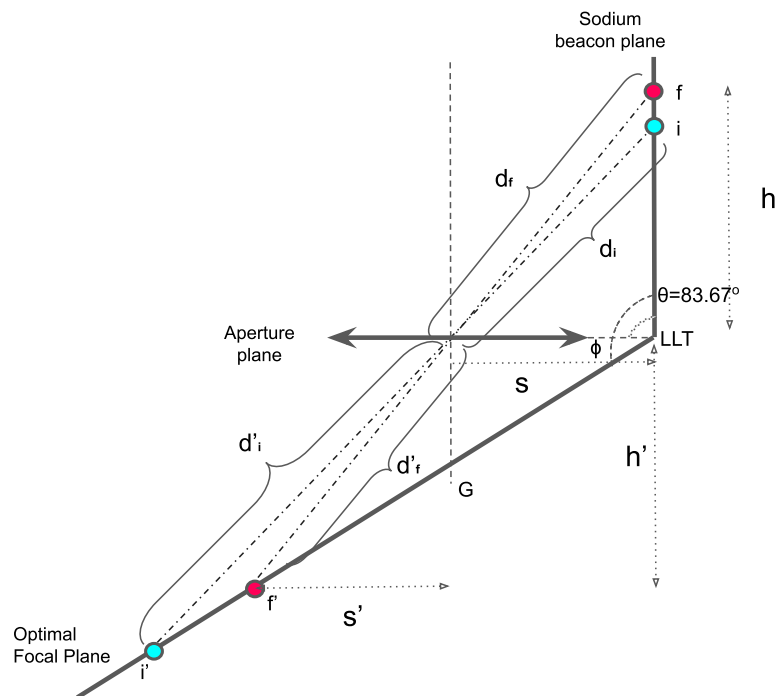


Figure 3.16: The Scheimpflug principle applied for the optical layout of the E-ELT, with the LLT placed outside the telescope's entrance pupil at a distance 21.5 m from its centre. A Sodium LGS is represented by its edges as points f and i , with respective focused image points f' and i' . The LGS image is tilted with respect to a focal plane perpendicular to the optical axis by angle $\phi = 83.67^\circ$. The distances s and s' of the image and focus points from the optical axis, and the distances h and h' from the entrance pupil are drawn. Additionally, the distances d and d' from the centre of the pupil are represented.

Chapter 4

Adaptive Optics at the European Extremely Large Telescope

Current AO systems on 8-metre class telescopes have recently demonstrated performance close to the theoretical diffraction limit. This resolution is enough to resolve large regions within galaxies (between 300 and 1000 pc in size) at redshifts $z \sim 1$. A new class of telescopes, Extremely Large Telescopes (ELTs), is foreseen to resolve structures of a few tens of parsecs in size, the approximate size of a major star forming region, at similar redshifts and higher. This new generation of telescopes includes projects already in development, such as the European Extremely Large Telescope (E-ELT), the Thirty Meter Telescope, and the Giant Magellan Telescope.

In addition, a many number of AO facilities have incorporated or are planning to incorporate LGS AO systems. The first implementation of an LGS AO on a large telescope was made on the Keck II telescope in 2006 [65] and later was extended to Keck I, in 2012. At the VLT, NAOS [66] (decommissioned in 2019) was the first AO system installed at the 8-metre telescopes and in 2004 it was upgraded to work with LGS. Also at the VLT, SINFONI [67] was an AO assisted near-infrared integral field spectrometer curvature sensor system, designed for operations with NGS or sodium LGS. Currently, almost all instruments at the VLT can incorporate LGS AO corrections. Gemini LGS facility, Subaru LGS AO facility and ARGOS at LBT are a few other examples outside the ESO telescopes.

Putting together the light-gathering capability of future ELTs and LGS AO systems can lead to groundbreaking discoveries that we simply cannot yet imagine. However, this is exactly the plan for the E-ELT, whose laser facilities are already in advanced development phases.

In this chapter we aim at describing the E-ELT project, together with its AO specifications. We will gather information regarding the current LGS WFS designs to be used in the different instruments and pinpoint their limitations to the quality of the images. Finally, we give examples of scientific cases which highly benefit from E-ELT's AO LGS wavefront sensing capabilities.

4.1 E-ELT: Project Description

The European Extremely Large Telescope, a project by the European Southern Observatory, is a groundbreaking astronomical observatory currently under construction. Designed to

observe in the visible and NIR bands, ESO's E-ELT record resolution will lead to observations of unprecedented quality, due to the incorporation of AO systems into the design of the telescope, that will offer the theoretical resolution of the telescope.

Its innovative optical design, based on a five-mirror configuration, is capable of collecting and focusing 20 times more light than a single VLT unit. The mirror specifications and positions are illustrated in Figure 4.1.

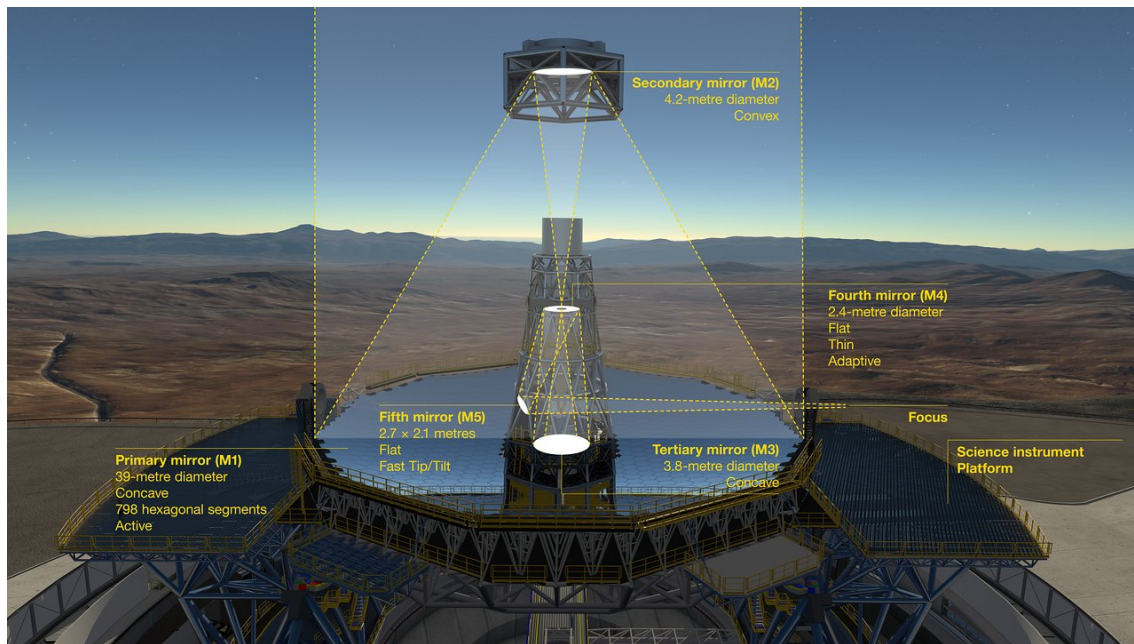


Figure 4.1: This diagram shows the novel 5-mirror optical system of ESO's E-ELT. Light is collected by the primary mirror M1 and before reaching the science instruments the light it is reflected by four other mirrors, M2, M3, M4 and M5. The final two mirrors (M4 and M5) form the built-in AO system. Image taken from ESO.

At the core of the E-ELT is a colossal segmented primary mirror (M1) with a diameter of 39.3 metres. Too large to be made from a single piece of glass, it will consist of 798 segments measuring close to 1.5 metres across. The segments will work together as a single mirror to collect the initial light. Once collected, the light's journey continues with the secondary mirror (M2), boasting a diameter of 4.25 metres. Positioned above the primary mirror, this convex secondary mirror reflects the collected light back downward, directing it to the next stage of the optical path. Nestled within the structure of the primary mirror is the concave tertiary mirror (M3) with 4 metre diameter. It plays a pivotal role in relaying the light to an adaptive, flat, 2.4 metre diameter mirror situated directly above it.

This adaptive mirror, the fourth in the sequence (M4), stands as a technological marvel as the largest DM ever made. It is capable of adjusting its more than 5000 actuators to change the shape of the mirror up to 1000 times per second. This rapid adjustment serves to correct for distortions induced by atmospheric turbulence. The journey of light culminates with the fifth mirror (M5). M5 will be a flat, elliptical mirror measuring 2.7×2.2 metres. The M5 unit folds the optical beams towards each Nasmyth focus, where the cameras and other sophisticated instruments can be found. In addition, M5 is hosted in a special cell that includes a fast tip-tilt system for image stabilisation, achieved by adjusting the mirror's tip and tilt angles to a few tens of miliarcseconds accuracy, within a 10 Hz bandwidth. This

intricate five-mirror design represents a remarkable engineering achievement.

One of the E-ELT's features that adds to its exceptionality is its AO system, capable of correcting for atmospheric turbulence and telescope vibrations caused by wind and movement, essential for reaching its diffraction limit. This limit is 8 mas in the J-band and 14 mas in the K-band, resulting in images 15 times sharper than those produced by the Hubble Space Telescope.

In the realm of AO, E-ELT faces challenges regarding the limited sky coverage (SC) when using a single NGS to provide AO corrections, as mentioned in Section 3.1. To obtain wide-field AO corrections with large SCs, E-ELT has integrated laser technology into their AO systems. E-ELT provides four sodium laser launchers to generate six to eight Sodium LGS, which can be placed around the scientific FoV. This strategic deployment effectively covers the turbulent volume of the atmosphere, enabling a tomographic reconstruction of atmospheric distortions and their correction along the optical axis, a technique known as laser tomography AO. This correction can also be extended to a wider FoV through MCAO.

The first generation instruments of E-ELT are MICADO, HARMONI, METIS and MORFEO and will start to operate at or shortly after E-ELT technical first light. Two instruments, ANDES and MOSAIC, will start operations at a later stage. Key characteristics of ELT first generation include:

- MICADO (Multi-Adaptive Optics Imaging Camera): Working in conjunction with the MORFEO AO system, MICADO provides diffraction-limited imaging over a wide FoV (about $1'$), in NIR ($0.8\text{-}2.4\ \mu\text{m}$). MICADO offers four observing modes: imaging mode, astrometry, long-slit spectroscopy and high contrast imaging.
- HARMONI (High Angular Resolution Monolithic Optical and Near-infrared Integral Field Spectrograph): Operating across a broad visible and NIR wavelength range ($450\ \text{nm}$ to $2450\ \text{nm}$), HARMONI enables 3D spectroscopy for studying a wide range of astronomical targets, from exoplanets to high-redshift galaxies.
- MORFEO (Multiconjugate Adaptive Optics RelaY for ELT Observations): MORFEO is a MCAO system that uses LGS to correct atmospheric turbulence, improving the E-ELT's imaging capabilities. However, MORFEO will not make scientific observations by itself. Instead, it will allow large field ($\sim 2'$) diffraction limited correction for MICADO and for a second instrument still to be defined.
- METIS (Mid-infrared E-ELT Imager and Spectrograph): METIS is designed for IR imaging and spectroscopy, covering various spectral bands. Observational capabilities include imaging and low/medium resolution spectroscopy at L/M band ($2.9 - 5.3\ \mu\text{m}$) and N/Q band ($7.0 - 19.0\ \mu\text{m}$), high resolution integral field spectroscopy at L/M band, and coronagraphy for high contrast imaging.

4.2 Adaptive Optics Modes and Systems

The success of the E-ELT in achieving its ambitious scientific objectives hinges on the optimal utilization of its diffraction-limited capabilities. To attain this, the telescope's instruments are equipped with a range of advanced AO systems, including SCAO, MCAO and Laser

Tomographic Adaptive Optics (LTAO). These AO systems are specifically designed to correct atmospheric distortions and enable observations across various resolutions, from conditions limited by atmospheric turbulence to those nearing the diffraction limit.

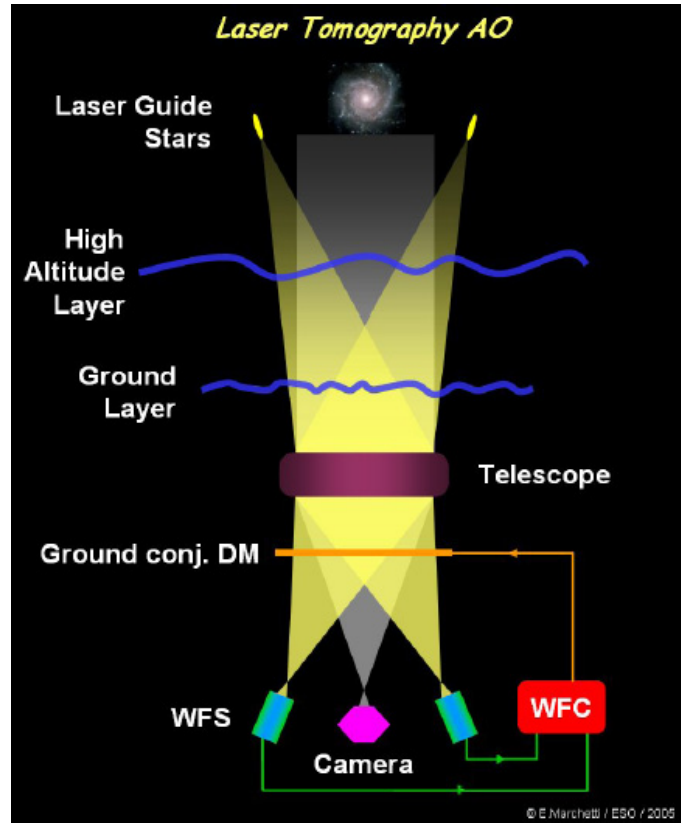


Figure 4.2: LTAO principle is illustrated. Taking advantage of more than one LGS on the FoV, the data from the WFS can be used by the RTC to reconstruct tomographically the atmospheric turbulence layer by layer. The cone effect can be controlled with this technique. Only one DM is used to apply AO corrections. Image from ESO.

SCAO and MCAO have been explained in Chapter 3. In LTAO, laser beacons are fired to provide wavefront sensing information in order to assess the turbulence distribution of the atmosphere, that is, dominant layers and respective amplitude of turbulence. Figure 4.2 illustrates the principle behind this type of AO system. This information is used to optimise the correction on-axis. It allows the AO system to reconstruct the turbulence above it layer by layer. Employed by HARMONI, it is a compromise between the SCAO and MCAO modes. It implements several off-axis WFS, but is optimised to analyse the centre of the FoV in detail. This way, the on-axis turbulence cylinder can be better sampled, almost as well as in the SCAO mode. The correction is applied using a single DM.

The E-ELT, with its primary goal of achieving the diffraction limit, introduces MICADO as its inaugural instrument. MICADO is engineered to operate in SCAO or MCAO mode. The MCAO correction will be provided by MORFEO and the SCAO correction at first light will be developed under MICADO's responsibility and jointly by MICADO and MORFEO thereafter. The AO performance of the SCAO mode is expected to reach $SR \sim 70\%$ nearby the AO reference source, in the K band [68].

With a point-source sensitivity that is comparable to JWST and a resolution about a factor 6 better, MICADO is well suited to numerous science cases.

As of 2022, MORFEO, previously known as MAORY, has undergone development. The design consists of an optical relay based in 7 mirrors, including 1 or 2 postfocal DMs, to deliver light from the focal plane of the telescope to the focal plane of the client instrument. By tilting one of those mirrors, it is possible to steer the light beam towards MICADO or the second client instrument. MORFEO drives the fourth mirror of the telescope, M4. M4, coupled with the M5, a tip-tilt mirror, provides the built-in wavefront correction system of the E-ELT.

MORFEO features an advanced tomographic sensing system, incorporating 12 WFS, 6 LGS, and 3 NGS. The 6 LGS constellation is projected on the edge of 1.5' diameter FoV while the 3 NGS will be observed within an 160" technical FoV beyond the MICADO area [69]. Only the stars brighter than magnitude $H = 21$ and $R = 24$ are valid references. Under typical conditions, MORFEO is anticipated to deliver a significant SR of approximately 35% in the K band, covering up to 50% of the sky at the galactic pole. In optimal conditions, MORFEO can achieve an impressive SR of 55% with minimal variations ($\leq 10\%$) over a 1' corrected field [70].

Within the E-ELT's instrument suite, HARMONI will be able to work in two different AO modes - SCAO that uses a bright reference star to provide high SR over a small fraction of the sky, and LTAO that combines 6 LGS with up to 2 fainter NGS to deliver diffraction-limited image quality in the JHK bands over a large fraction of the sky [71]. Moreover, it can also work without AO, a mode called NOAO. These two modes are applied by two AO systems fully integrated within HARMONI: one working with artificial LGS (LGSS) and the other working with NGS (NGSS). To implement the LTAO mode, the instrument will use the LGS sensors provided by the LGSS together with the appropriate NGS sensor, and the E-ELT corrective optical components M4 and M5 [72].

Under median seeing conditions the SCAO system shall deliver an on-axis SR 70% at the K band ($\sim 2 \mu\text{m}$ wavelength) for NGS brighter than mag $V = 12$ and median wind conditions [73]. SCAO will work up to 15" off-axis, optimal performance is achieved for stars down to $M_V = 12$, with a limiting magnitude of $M_V \sim 17$. The diffraction limit (10 mas) can be obtained in 1% of the sky. NGSS is able to operate with stars as faint as $H_{AB} = 19$, so that HARMONI's LTAO system can provide excellent SC: 75% of the sky at the south galactic pole with SR exceeding 30% at K band under median conditions [74].

Finally, HARMONI's NOAO mode can provide "seeing-limited" performance. NOAO utilises a faint ($I < 23$) NGS for slow (~ 0.1 Hz) secondary guiding, eliminating slow drifts of the instrument focal plane and ensuring accurate pointing.

Lastly, METIS is designed to achieve the diffraction-limited image quality of the E-ELT. It employs a SCAO system [75] where the AO guide star can be picked up anywhere within a circular FoV with a diameter of 27". All observing modes for METIS require AO. Future upgrades may incorporate a laser AO system utilizing a single LGS, further enhancing its capabilities [76]. For bright (mag $K \sim 10$) AO guide stars under median seeing conditions, METIS will achieve a $SR > 87\%$ at $3.7 \mu\text{m}$ ($> 95\%$ at $10 \mu\text{m}$), which drops to $\sim 62\%$ ($\sim 93\%$) for a $K \sim 12$ magnitude guide star [77].

In the following Table 4.1, we gather all the AO performance-related information of the four first light instruments to operate at the E-ELT. This information was separated according to the AO modes offered by each instrument. Important quantities to measure AO performance of SCAO include the peak SR obtained, at a specific band or wavelength, and the limiting magnitude of the NGS used. SCAO correction peaks on-axis and, in general, has a SC of 1% for diffraction-limited imaging [78]. MCAO performances are characterised by the average SR over a wider FoV at a specific band or wavelength whereas LTAO achieve higher SR on axis. Both of them achieve bigger SCs.

| | MORFEO/MICADO | HARMONI | METIS |
|------|--------------------------------------------------------------------------------------------------------------|--------------------------------------------------------------------------------------------------------|----------------------------------------------------------------------|
| MCAO | up to 6 LGS up to 3 NGS extra DMs: 2 SR: 35 – 55% (K band) FOV: 51" × 51" SC: 50% [69, 70] | | |
| SCAO | mag: $R \sim 10$ SR: 66% (K band) on axis SC: 1% [68, 79, 80] | mag: $V \sim 12$ SR: > 70% ($2 \mu\text{m}$) on axis SC: 1% [73] | mag: $K \sim 12$ SR: 62% ($3.7 \mu\text{m}$) on axis [77] |
| noAO | | NGS with $I < 23$ seeing limited [74] | |
| LTAO | | up to 6 LGS up to 2 NGS extra DMs: 0 SR: > 30% (K band) on axis SC: 50% [71, 72, 74] | |

Table 4.1: Comparison of expected/simulated AO performances for the first generation E-ELT instruments across their AO modes: MCAO, SCAO, LTAO or no AO mode NOAO. The values of SR correspond to the peak performance under median seeing and wind conditions for the specified magnitude and wavelength band. The SC is about the diffraction-limit, for SCAO, and for the mentioned SR ratios, for the other modes.

4.3 Wavefront Sensors for the E-ELT

Wavefront sensing is a critical aspect of the E-ELT instruments. Current WFS being incorporated into the instruments designs are SH-WFS and P-WFS.

MICADO's SCAO at first light:

The SCAO correction, available at first light, is developed by MICADO and the chosen SCAO WFS is a double pyramid WFS. With this sensor, the requirements of the instrument are fulfilled [80].

MORFEO's LGS Wavefront Sensors:

The MCAO mode in MORFEO is based on the use of two WFS modules: an LGS WFS module with 6 beacons (upgradable for 8) arranged in a 45" radius asterism, an NGS WFS module with 3 low order sensors and 3 reference sensors patrolling a technical FoV of 160".

The LGS WFS module contains 6 wavefront sensor units to measure wavefront distortion on the LGSs. The LGS WFSs employs a 68×68 subaperture Shack-Hartmann configuration with a FoV of approximately 16", minimizing truncation errors. Their pixel scale is set at 1.15" per pixel.

The second module is the Low Order and Reference (LOR) Module and implements the NGS wavefront sensing functionalities. It consists of three identical Low Order and Reference (LOR) sensor units to sense the aberrations in the direction of 3 NGSs chosen in a technical field. Each LOR unit contains two WFSs: a Low Order (LO) WFS for the H band and a Reference (R) WFS for the R+I band. They share the light coming from the same NGS. The LO-WFS has a 2 × 2 subaperture Shack-Hartmann configuration with a 1" FoV, 9 mas per pixel, to sense the atmospheric tip-tilt, focus and astigmatism. The R-WFS features a 10×10 Shack-Hartmann configuration with a larger FoV, which act as truth sensor to detrend LGS wavefront estimates and measure pseudo-static aberrations of the telescope and of the post focal relay optics, at a slower rate.

The MORFEO system incorporates a dichroic beam splitter that divides light into visible and NIR parts. The visible portion is directed to the LGS WFS, while the NIR segment is conveyed to the MICADO instrument. The LGS part may introduce Non-Common Path Aberrations (NCPAs) with respect to MICADO, which are meticulously compensated for with a secondary WFS loop for truth sensing.

MORFEO's Tomographic Truth Sensing:

MORFEO represents a significant advancement in wavefront sensing technology, introducing a tomographic truth sensing system through its R-WFS. This auxiliary control loop, based on visible NGS WFSs, is instrumental in detrending pseudo-static aberrations introduced by the AO loop in the DMs. It also corrects for NCPAs between LGS WFSs and the scientific focal plane, as well as other LGS sensing artifacts such as spot truncation.

MORFEO's R-WFS uses NGSs with minimal and calibrated NCPAs, although there may still be some discrepancies between the wavefront seen by the R-WFS and the scientific FoV due to the off-axis position of the NGSs and the off-axis aberrations of the MORFEO relay. To overcome this limitation, the NGS-MICADO NCPAs are subtracted from the signals of each R-WFS before wavefront reconstruction.

METIS SCAO Wavefront Sensor

A trade-off study resulted in the decision to change the baseline in favor of a P-WFS, operating in the near-IR and located inside the cryogenic environment of the METIS instrument. It shows a better performance in terms of SR with fainter stars.

HARMONI SCAO Wavefront Sensor

SCAO uses a dichroic that sends light in the 700–1000 nm range to a P-WFS operating at 500 Hz, with longer wavelengths (1000–2450 nm) available for spectroscopy with the integral field unit.

HARMONI Tomography LGS WFS

HARMONI faces challenges related to elongated LGS spots due to side launch configurations, requiring a large number of pixels per Shack-Hartmann subaperture. This presents a trade-off between pupil spatial sampling, subaperture field-of-view, and pixel sampling within each subaperture. The limitations of current WFS formats in handling LGS spot elongation are being addressed through new simulation-based methods.

For classical SH-WFS, which is the current baseline for all E-ELT LGS-assisted instruments, a trade-off between the pupil spatial sampling (number of subapertures), the subapertures' FoV and the pixel sampling within each subaperture is required. For E-ELT scales, this trade-off is also driven by strong technical constraints, especially concerning the available detectors and in particular their number of pixels. For a given number of available detector pixels, the subaperture FoV is competing with the proper sampling of the LGS spots, and/or the total number of subapertures. For SH-WFS, a larger FoV per subaperture allows to mitigate the LGS spot truncation, which represents a severe loss of performance due to measurement biases.

These challenges highlight the need for innovative solutions and ongoing research to optimize LGS WFS technologies for the E-ELT and its ambitious scientific goals. Indeed, the traditional WFS strategies will not be applicable for the E-ELT, because the available detector formats will not be adapted to the strong LGS spot elongation [73, 81, 82, 57]

4.4 Science Cases aided by LGS AO systems

Together, the science cases covered by the E-ELT address many of the major questions in astrophysics: *Planetary systems*, including cases in our own Solar System, exoplanets and the formation of planetary systems; *Nearby stellar systems*, comprising stars and stellar systems within our own Galaxy and its satellites; *The local Universe*, with science cases aimed at studying the stellar content and the structure of distant stellar systems that can be at least partially resolved into individual stars; *The high-redshift Universe* as well as high-energy phenomena over the range of cosmic distance and time made accessible by the E-ELT ¹.

A more interesting question we want to explore is what are unique science cases that will benefit from LGS WFS? As described in the previous sections, LGS WFSs will be incorporated into the MCAO and LTAO modules of the first light instruments. Here, we outline some of the most intriguing science cases [83]:

1. Accretion, Ejection, and Disks in Young Low and Intermediate Mass Stars

¹E-ELT Science Cases

Laser-assisted MCAO will extend our ability to study fainter T Tauri stars and even Herbig Ae/Be-type stars. This allows us to delve deeper into the mechanisms of accretion, ejection, and the connection between jets and disks. High-resolution imaging with MORFEO+MICADO/HARMONI is expected to improve angular resolution and sensitivity by an order of magnitude relative to what is possible to achieve with VLT and JWST.

2. Protoplanets and Protoplanetary Disks

MCAO will facilitate the search for protoplanets around young stars, even those with magnitudes in the visible of 13 – 14 (and lower), a task previously challenging with current AO instruments.

3. Minor Bodies of the Solar System

Laser WFS in MCAO or LTAO mode becomes crucial for resolving faint asteroids and Kuiper Belt Object with magnitudes below 15 in the H band. It ensures accurate observations where SCAO limitations come into play. MORFEO+MICADO provides non sidereal tracking both in SCAO (for bright objects) and MCAO.

4. Search for Population III stars

Gridale et al. 2021 [84] used simulations to show that HARMONI LTAO could confirm the presence of the first stars (Population III stars) in galaxies at very high redshifts ($z = 3 - 10$) by measuring the strength of the He II 164 nm line. These simulations recovered the line's strength with good SNR from a substantial fraction of $z > 6$ galaxies in a ~ 10 hour exposure [74].

5. Bulge Star Astrometry and Photometry

MORFEO+MICADO proves invaluable for obtaining precise astrometry and deep photometry of faint bulge stars. MCAO is the preferred mode for its larger FoV and uniform PSF.

6. Studying Young Star Clusters at the Large Magellanic Cloud

The young star cluster R136 is an ideal candidate for a birthplace on an intermediate mass black hole. Using N-body simulations, Fiorentino et al. 2020 [85] studied the dynamical detection of an intermediate mass black hole with mass $\sim 10^4 M_{\odot}$ on R136. With the H and K bands, faint stars down to $K = 22$ mag can be detected and their positions accurately measured, in the MCAO mode of MORFEO. These simulations served as confirmation for the fulfilment of the astrometric requirement of MORFEO of $50 \mu\text{as}$.

There is no doubt that extreme astrometric performance in a small FoV is needed and hence SCAO mode provides the best performance. However, it is also true that the presence of a bright star ($R \leq 15$) within the FoV (which is essential for SCAO mode) may severely limit the SC and decrease the photometric and astrometric quality of the measurements. Fiorentino et al. 2020 [85] concluded that for these scientific applications, observations with the MCAO mode may be the only way to observe some targets.

7. Searching for the First Galaxies

Lymann Break Galaxies at $z > 13$ are a candidate for being the oldest galaxies in the Universe. MCAO is the primary mode for searching for galaxies at redshifts beyond 13. Its larger FoV and SC at high galactic latitudes enhance the probability of discovering these ancient cosmic entities, through dedicated deep surveys.

In general, AO modes with LGS are the preferred choice when stable corrections across a large FoV or observations of candidates independently of a bright NGS are required.

Finally, we look at a specific case regarding the benefits of LGS WFS when studying star formation in high- z galaxies on various scales, including subclumps, giant HII regions, super-star clusters, and proto-globular clusters.

4.4.1 Star Forming Clumps in High-Redshift Galaxies

Galaxies are fundamental components of the observable Universe, composed of billions of stars varying in age and chemical composition. To gain a deeper understanding of galaxy formation and evolution, it's essential to analyze the structures, stellar populations and gas dynamics within distant galaxies. The E-ELT offers an unparalleled opportunity for such analysis.

The hierarchical assembly model, the prevailing theory of galaxy formation, suggests that galaxies evolve from smaller building blocks, potentially through mergers or secular processes like gravitational instabilities. The high-redshift universe, with its peak star formation rate (SFR) occurring around redshifts $z \sim 2$ [86], offers insights into the dominant mechanism of galaxy evolution. Galaxies at this redshift exhibit irregular morphologies characterized by bright knots with blue colors, often referred to as "clumps," which are star forming regions [87]. Local Universe and moderate redshift ($z < 2$) clumps have been extensively studied using various datasets, but contradictory explanations for their origin and evolution have emerged. It remains uncertain whether they are remnants of accreted satellites or star-forming complexes formed in-situ within gas-rich, turbulent, high-redshift disks. Further observational studies, incorporating both spatially-resolved imaging and spectroscopy, are essential for reaching more definitive conclusions.

The fate of clumps is also a subject of debate. They may be quickly disrupted by strong stellar feedback and tidal forces, leading to the removal of gas and the unbinding of the stellar system. Alternatively, models suggest that clumps, due to their high star formation efficiencies, could efficiently convert their molecular gas into stars over a short timescale and remain bound, surviving stellar feedback for over 500 million years. In this scenario, clumps might migrate inward, merge, and contribute to the growth of the galaxy's bulge, possibly fueling the central black hole.

Furthermore, investigating the formation and physical properties of clumps offers a promising avenue for understanding how galaxies accumulate mass, whether through mergers or secular evolution, and how star formation proceeds at high redshifts.

Here we summarise the physical quantities of the clumps studied so far:

- Clumps have typical stellar masses $M_* \sim 10^7$ - $10^9 M_\odot$
- Clumps have typically sizes of 1 kpc (limited by current instrument's resolution);
- Some high-redshift lensed galaxies have smaller clumps with sizes of ~ 100 – 500 pc (limited by current instrument's resolution).

- Clumps have stellar ages of ~ 300 Myr, depending on z .
- Clumps have velocity dispersions ranging from 40 to 50 km/s.
- High z galaxies can have 0 to 8 giant clumps each.

In order to deepen the knowledge related to galaxies, be either evolution, formation, or disruption, studying more clumpy high-redshift galaxies in more detail will be helpful. However, to do so, instruments must reach very high spatial and spectral resolutions. Figure 4.3 summarises current cutting edge images obtained with space based observations (HST), ground based observations without AO corrections (SINFONI at VLT) [9] and ground based observations with AO corrections (SINFONI at VLT)[10], of the high-redshift $z = 2.2405$ galaxy ZC400569. ZC400569 has a complex morphology characterized by a brighter northern source and a southern clumpy extension. Respectively, these three observations reached spatial resolutions of 1kpc, 5kpc and 2 kpc, which is not enough to sample the substructure of the clumpy structures that are less than 1 kpc wide. In this particular case, the AO mode chosen for SINFONI used NGS, using a star with mag $R_{Vega} = 15.2$ at a distance $20''$ from the target, achieving SR of 18%.

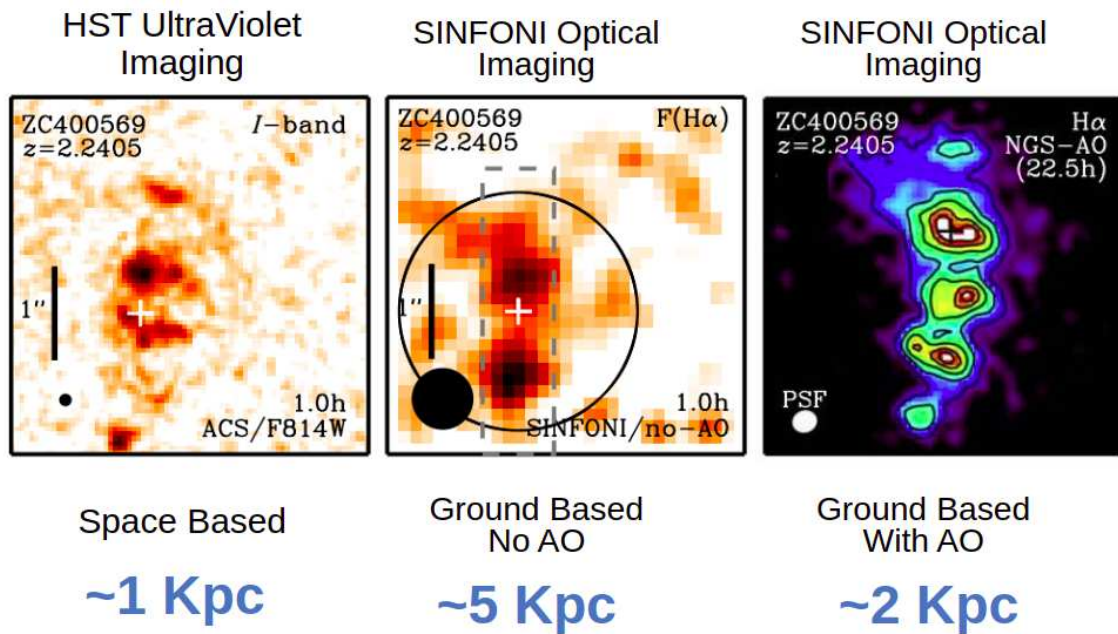


Figure 4.3: High-redshift $z = 2.2405$ galaxy ZC400569 imaged with current cutting edge instruments. **Left:** Space based observations (HST) [9] **Middle:** Ground based observations without AO corrections (SINFONI at VLT) [9] **Right:** Ground based observations with AO corrections (SINFONI at VLT). Respectively, these observations reached spatial resolutions of 1 kpc, 5 kpc and 2 kpc. Circles on the left bottom side of each image indicate the size of the PSF. Set of images from Mancini et al. 2011 [9] and Forster-Schreiber et al. 2018 [10].

A priori, HARMONI's characteristics seem to have enough potential to surpass these observations. With its diverse plate scales and spectral resolutions, it can resolve up to 180 pc under average AO performance and 130 km/s and 43 km/s spectral resolutions at $z \sim 2$, on the H+K and K bands.

In Zieleniewski et al. 2015 [11], a study was developed to evaluate the capabilities of HARMONI for studying high-redshift galaxies, particularly focusing on their substructures

and star-forming regions. Galaxies with $z = 2 - 3$ and $H\alpha$ emission were the focus, to have line emissions falling at the K band in the observations.

The study begins by generating a sample of input galaxy data cubes, encompassing various parameters such as redshift, SFR, gas fraction, morphology, and the inclusion of star-forming regions (clumps). Simulated observations of these galaxies using HARMONI's pipeline (developed by the same author [11]) in LTAO mode are conducted, under a seeing of $0.67''$. Parameters include a total exposure time of 10 hours and a resolving power of $R \sim 3500$ using the H+K grating, primarily focusing on the 20×20 mas scales, corresponding to ~ 200 pc at $z = 2 - 3$.

The results of these simulations revealed that HARMONI can accurately measure velocity profiles in galaxies, reaching down to Milky Way-like SFRs, with a spatial resolution of at least ~ 200 pc in the brightest/highest SNR regions during a 10-hour observation. To demonstrate HARMONI's ability to discern properties of individual star-forming regions, simulations with different SFRs are performed. For that, they focus on a galaxy with $z = 2.07$ and simulate it under different SFR, with a LTAO PSF of 40mas, corresponding to ~ 300 pc at this redshift.

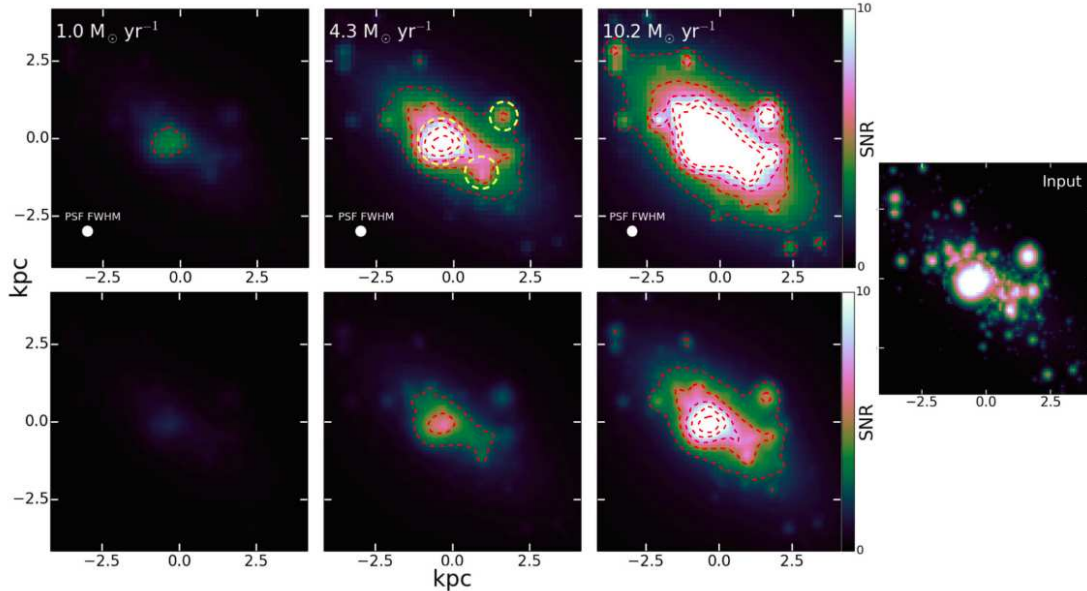


Figure 4.4: SNR maps of a model clumpy galaxy $z = 2.07$ for varying SFRs observed at 20×20 mas (top row) and 10×10 mas (bottom row). SFR increases from left to right and is denoted in the top left of each panel. The size of the LTAO PSF is shown in the bottom left of the each map in the top row. The total exposure time is 10 h. The three star-forming clumps detected are highlighted with yellow-dashed circles in the central panel of the top row. For comparison, we also show the input morphology (10 mas sampling) in the right-hand subplot. Image from Zieleniewski et al. 2015 [11].

Figure 4.4 shows the recovered $H\alpha$ SNR maps for a 10-hour observation at the 20×20 mas (top row) and 10×10 mas (bottom row) scales. Assuming circular symmetry of the clumps, clump radii were measured as 980 ± 150 pc, 500 ± 200 pc, and 520 ± 250 pc, respectively. These measurements closely match the input clump sizes of 1000 pc, 630 pc, and 500 pc, respectively. In fact, from the SNR map of this galaxy with $SFR = 10.2 M_{\odot} \text{yr}^{-1}$, (top right panel) Figure 4.4, we see there are clumps of three pixels diameter in the 20 mas scale with $SNR > 5$. This corresponds to ~ 250 pc scale clumps.

In conclusion, the simulations demonstrate that the E-ELT with HARMONI can obtain

velocity maps of $z \sim 2 - 3$ star-forming emission-line galaxies down to Milky Way SFRs of sizes ~ 250 pc at these redshifts. Importantly, this approach provides a significant improvement in spatial resolution (about $4\times$) compared to space based observations with HST.

In the present year, observations of the SDSSJ165202.64+172852.3 $z = 2.94$ galaxy, hosting a red quasar, were done by Vayner et al. 2023 [12] with the JWST Near-Infrared Spectrograph Integral Field Unit. Standard emission-line maps revealed a collection of 1 kpc scale clumps forming stars at a rate of at least $200M_{\odot}\text{yr}^{-1}$.

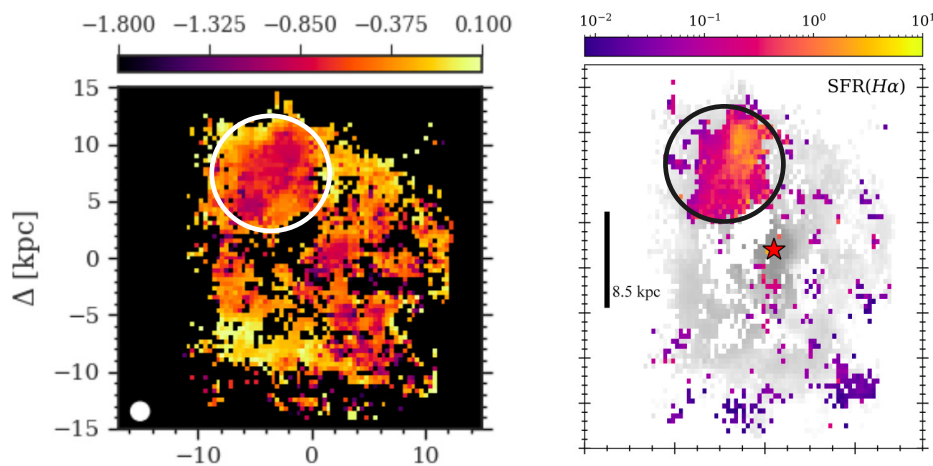


Figure 4.5: **Left:** Map of $\log[\text{NII}]/\text{H}\alpha$ emission line ratio of a kinematic component of the SDSSJ165202.64+172852.3 $z = 2.94$ galaxy associated with high star formation rates. White ellipse in the lower left corner shows the size of the Near-Infrared Spectrograph Integral Field Unit PSF. White circle on the top left highlights the region where star forming clumps of size ~ 1 kpc were detected. Individual clumps couldn't be resolved. **Right:** Extinction corrected $\text{H}\alpha$ derived star formation rate $\text{SFR}(\text{H}\alpha)$ map in the same galaxy. Black circle on the top left highlights the region where star forming clumps of size ~ 1 kpc were detected. Images from Vayner et al. 2023 [12].

However, the authors point out that the resolution of the observations is not enough to distinguish the inner structure of these clumps and that likely they contain smaller subclumps. Due to some challenges associated with the Near-Infrared Spectrograph Integral Field Unit data reduction, the FWHM of the simulated PSF for the Near-infrared Camera of JWST is about $0.065''$ at $2 \mu\text{m}$ (K band), obtaining SR of 80%. This corresponds to a spatial resolution of ~ 500 pc at this redshift². This size is primarily determined by the diffraction limit of the telescope.

In conclusion, E-ELT's HARMONI simulations show hints that this instrument, with LTAO supported by LGS, has a potentially higher spatial resolution and sensitivity than JWST and other ground-based telescopes with AO.

To highlight other advantages of LGS, we look at the data analysed by Scheiber et al.

²using a scale of $7.901 \text{ kpc}''$ obtained with the [Cosmological calculator](#) with a three-dimensional flat geometry of ΛCDM cosmological model with $H_0 = 69.6 \text{ kms}^{-1}\text{Mpc}^{-1}$, $\Omega_M = 0.286$, and $\Omega_\Lambda = 0.714$.

2018 [10]. It consists of 35 star-forming galaxies, the largest sample with deep AO-assisted near-infrared integral field spectroscopy at $z \sim 2$. The observations of the SINS/zC-SINF AO sample were carried out with SINFONI [67], mounted at the Cassegrain focus of the VLT UT4 telescope. The AO correction was performed in NGS or LGS mode. The choice of mode depended on the brightness of the reference star and its distance to the science target; 18 targets were observed in NGS mode and 15 in LGS mode. Figure 4.6 shows the distribution of the PSF FWHMs. Overall, there is no significant difference in FWHMs between the PSFs observed in NGS or LGS mode but the availability of LGS allowed almost to duplicate the size of the sample.

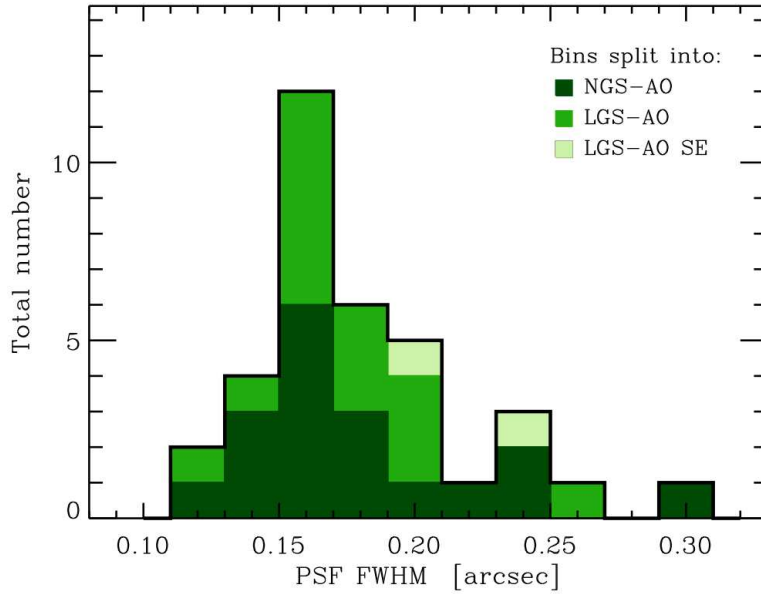


Figure 4.6: Histograms showing the distribution of values of the PSF FWHM of the observations of 35 star-forming galaxies. The AO modes varied between NGS and LGS. In general, the mean of the distribution of NGS and LGS FWHM is very similar. It is important to highlight that LGS allowed the galaxy sample to duplicate in size.

Chapter 5

Laboratory Testing of Ingot Wavefront Sensor

In this chapter, we shed light on the advances made on the testing of the Ingot Wavefront Sensor (I-WFS) on experimental setup at the INAF-Osservatorio Astronomico di Padova. This setup features a test bench designed to assess the performance of an optical layout mimicking the E-ELT system with an I-WFS.

Within this chapter, we detail the various components comprising the optical bench and outline the main procedures devised before the start of the six-month master's thesis. Subsequently, we elucidate the essential tests carried out and introduce novel methodologies that were developed. At the same time, we highlight adjustments made to the test bench itself. These modifications play a crucial role in the characterization, assessment, and prototyping of the I-WFS.

This segment concludes by enumerating potential directions for future investigation, aimed at further advancing our knowledge of the I-WFS.

5.1 Experimental Set-up: Test Bench

The test-bench setup comprises readily available components. It is specifically crafted to simulate the imaging of the LGS source onto the I-WFS, generating an image of three pupils on a dedicated camera with accurate sampling. Furthermore, the design strives to mirror the characteristics of the ELT as closely as possible. This includes:

- The ratio between the separation of the LLT and the entrance pupil diameter.
- The physical size of the image on the I-WFS prism.
- The telecentric image space on the I-WFS prism.
- The aspect ratio of the LGS (ratio of spot elongation to FWHM).

The optical layout, illustrated in Figure 5.1, is a 1:1 re-imaging relay, comprising the following elements:

1. An OLED screen, programmed with an Arduino, replicates the LGS. This SSD1306 monochrome OLED display¹ measures 128x64 pixels with a pixel size of 170 μm . It has

¹Datasheet available [here](#)

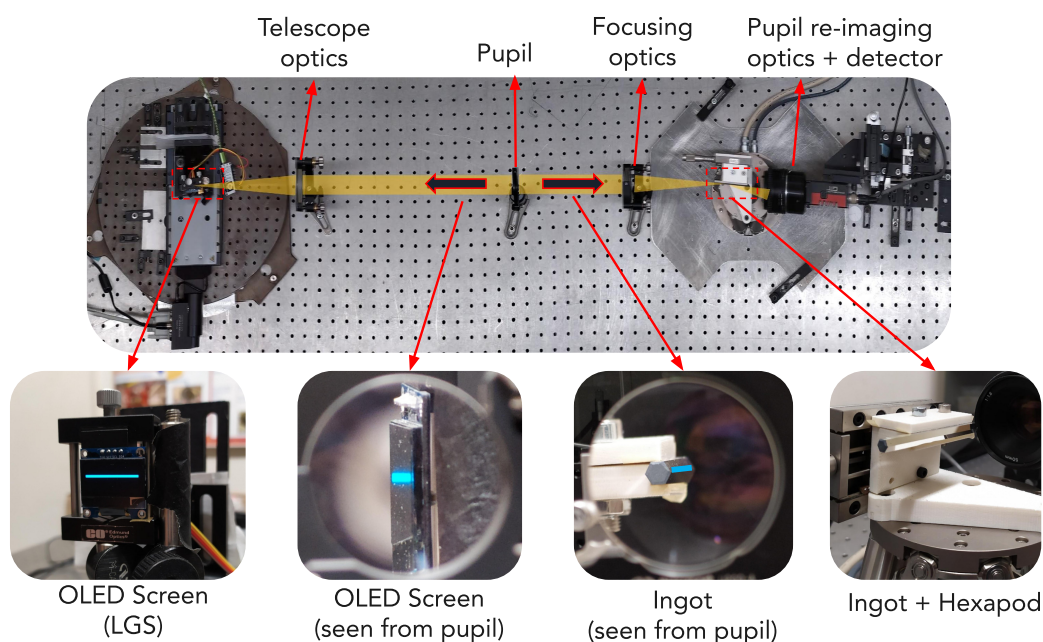


Figure 5.1: Top view of the optical bench setup used to test the ingot alignment procedure. Detailed images of the OLED Screen (seen face on and from the pupil) and of the Ingot (seen face on and from the pupil).

minimal background noise emission of black pixels, which distinguishes it from other display technologies.

2. A collimating achromatic doublet with a focal length of $f = 200$ mm for the incoming LGS light and another for refocusing the light onto the I-WFS prism.
3. A diaphragm acting as the aperture stop/pupil with a clear aperture of 25 mm. Positioned for image space telecentricity, it's at the focus of the camera doublet.
4. A pupil re-imager optics employing a wide-aperture $f = 50$ mm photographic objective.
5. The I-WFS, built from a hexagonal light pipe, often used for beam homogenization. The external faces were aluminized to obtain a reflective roof with a 120° apex angle, matching the ELT's requirement for proper pupil separation.
6. The camera, a Prosilica GT3300 from Allied Vision, equipped with an 8-megapixel CCD sensor featuring $5.5 \mu\text{m}$ pixels. To sample the pupil diameter, a 4×4 binning mode with ≈ 130 pixels is utilized.
7. The I-WFS prism is mounted on a H-811 Hexapod from Physik Instrumente, enabling precise movements in all six degrees of freedom for the I-WFS. The orientation of the I-WFS on the hexapod is shown in Figure 5.4.
8. In order to mitigate stray light effects, we added a black cover over the test bench.

Before entering into details regarding the work performed during the past six months, it is important to specify most of the methodologies that had already been developed, to which a few alterations have been added in this work. This encompasses the **pupil analysis procedure**, the **absolute alignment procedure**, and the **calibration procedure**. These

methods can be found described in more detail in Di Filippo et al. 2022 [88], Radhakrishnan Santhakumari et al. 2020 [13], and Simone Di Filippo's PhD thesis [6].

Pupil Analysis Procedure

The detector image, which must not be saturated, is analyzed in an autonomous Python script. Each pupil, of circular shape, is defined by an x position, a y position, and an r radius organized in an array such as: (x, y, r) . The coordinates are given according to the axes represented in Figure 5.2, and are given in the number of pixels of the camera. There are two possible settings, left for the user to choose when scanning the camera image to detect the positions of the pupils:

- Autodetection True: using a Canny-edge algorithm and Hough transform ([89, 90, 91]), the code is able to identify the position of the three pupils, fit them, and define the radii and the coordinates of the centers (in pixels).
- Autodetection False: a predefined set of coordinates and radii is used to define the pupil areas. The choice of coordinates is related to where the aligned pupils are expected to be. Up until now and with the current set-up, the following coordinates have been used:

$$\begin{aligned} A &= (431., 179., 131.) \\ B &= (293., 419., 131.) \\ C &= (570., 419., 131.) \end{aligned} \tag{5.1}$$

Autodetection False mode is also activated when, once in Autodetection True, the algorithm cannot detect exactly three pupils. If fewer than three pupils are detected, the system is most likely very far from the perfectly aligned position. More than three pupils can be detected, as sometimes the optics reveal strong ghost images. These should be discarded.

After obtaining the radii and coordinates of each pupil, the algorithm extracts the counts from the respective area and performs a rotation and flip to compensate for the effects introduced by the reflection from the Ingot prism. Once the pupils are located and aligned, they are used to calculate the signals S_x and S_y pixel-wise with Equations 3.11. The result obtained appears in Figure 5.2, with the three extracted pupils identified. An example of the S_x and S_y signals derived from an aligned position are shown in Figure 5.3.

Absolute Alignment Procedure

A fundamental step to perfect before any wavefront sensing can be done with the signals obtained from the pupils is to make sure the I-WFS is aligned with respect to the LGS source. In other words, the I-WFS must be placed on the optimal focal plane of the optical system, given by the Scheimpflug principle which was explained in Section 3.2. More precisely, as explained in Section 3.2, due to the requirement of having the pupils separated, the aligned position is actually tilted by $\omega = 0.3^\circ$ with respect to the optimal focal plane.

The aligned configuration corresponds to having three pupils equally illuminated and equidistant, as if placed on the corners of an equilateral triangle, as shown in Figure 5.2. By equally illuminated we mean that the total flux in each of them is 1/3 of the total. In reality, the pupil edges, especially in the central part of the detector, are unevenly illuminated

because of the geometry of the ingot. This translates into a specific pattern on the S_x and S_y signals as seen on Figure 3.1, which are not flat as in the case of an aligned P-WFS.

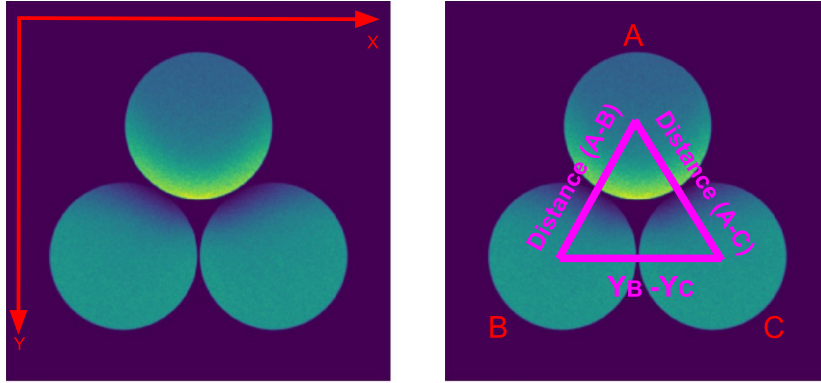


Figure 5.2: **Left:** Detector image of the three pupils' illumination on an aligned configuration, with the reference axis x and y depicted. **Right:** Identification of the A, B and C pupils and the three observables related to pixel distances: distance $A - B$, distance $A - C$ and vertical distance $Y_B - Y_C$. Images adapted from Kalyan et al. 2020 [13].

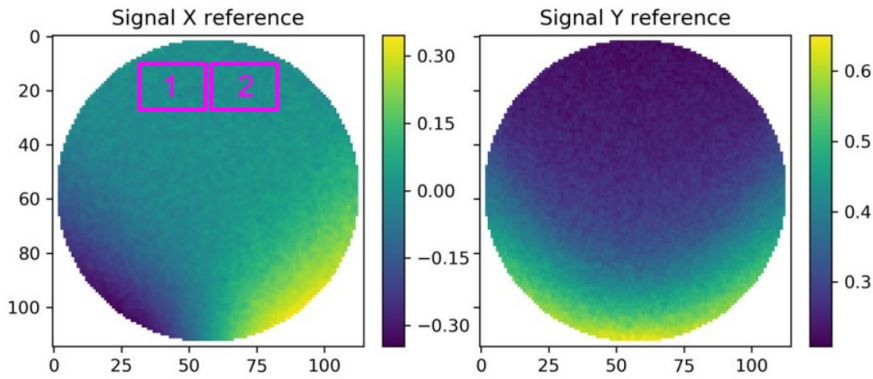


Figure 5.3: Signals S_x and S_y are calculated from the pupils using Equations 3.11 and are here displayed, for an aligned configuration. From the S_x signals, the observable $\overline{S_{x1}} - \overline{S_{x2}}$ is obtained using the two regions identified here. Moreover, the non uniform pattern of these signals is evident. Images adapted from Kalyan et al. 2020 [13].

The orientation of this pupil triangle with respect to the ingot's roof is demonstrated in Figure 3.13. It needs to be pointed out that in this image, the ingot is indeed a prism whereas in the current set-up, the prototype is a hexagonal pipe whose two fully exposed faces are used as reflecting surfaces. Figure 5.4 depicts the orientation of the hexagonal aluminized pipe, with its two reflecting surfaces, on the optical path. As a consequence, the triangle of pupils is tilted by 90° counterclockwise with respect to that of Figure 3.13.

In summary, the absolute alignment of the ingot is related to the relative position of the three pupils and to the distribution of light among them. The procedure of taking the ingot from a random position to the aligned position will be mentioned many times and is from now on called the alignment procedure. To reach that position, the ingot's position is adjusted on the optical path and rotated, in a coordinate system defined by X, Y, Z coordinates, and U, V, W angular coordinates (rotation around each axis, respectively). Accurate positioning is achieved by the hexapod stage where the ingot is placed, as shown in Figure 5.4, with its 6 degrees of freedom and precise movements of the order of microns.

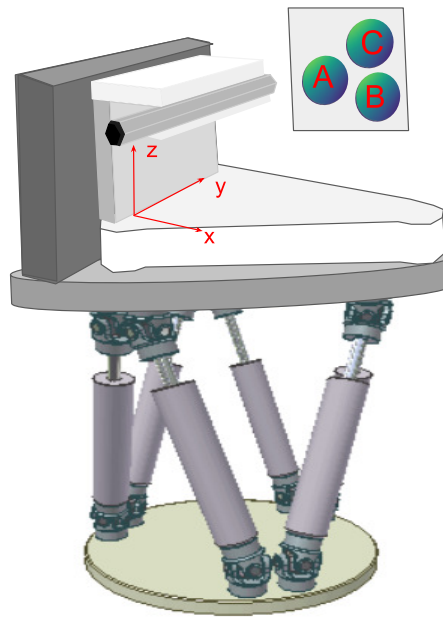


Figure 5.4: The ingot prism is held by a 3D printed structure, placed on an hexapod stage with 6 degrees of freedom. The coordinate axis (x, y, z) used to measure the positions of the hexapod throughout the rest of this thesis are depicted, with the origin defined internally on the hexapod program. The orientation of the three pupils of the image formed on the camera is clarified (the re-imaging optics is omitted for clearance).

To measure deviations from the aligned position, we established six distinct measurements concerning the positions and intensities of the pupils. These measurements are collectively referred to as observables. The reference configuration, as elucidated earlier, can be discerned by establishing a target value for each observable. Here follows a breakdown of each individual observable, accompanied by a visual explanation in Figure 5.2:

1. The difference between the flux of pupils C and B, normalized to the total flux of the three pupils:

$$\frac{C - B}{A + B + C}$$

2. The difference between the flux of transmitted pupil A and the sum of the fluxes of reflected pupils B and C, normalized to the total flux of the three pupils:

$$\frac{A - (B + C)}{A + B + C}$$

3. The distance between the centers of pupils A and B, given (in pixels) by

$$A - B = \sqrt{(X_A - X_B)^2 + (Y_A - Y_B)^2}$$

4. The distance between the centers of pupils A and C, given (in pixels) by

$$A - C = \sqrt{(X_A - X_C)^2 + (Y_A - Y_C)^2}$$

5. The vertical distance between the centers of pupils B and C, given by $Y_B - Y_C$, in pixels;

6. : $\overline{S_{x1}} - \overline{S_{x2}}$: The difference of the average value of S_x , computed on each pixel using Equation 3.11, in the two regions located on the top-left and top-right, identified by the numbers 1 and 2 (see Figure 5.3).

In the following Table 5.1, the target values for each observable that identify the aligned position are presented.

| Observable | Target Value |
|-----------------------------------------|--------------|
| Flux($C - B$)/($A + B + C$) | 0 |
| Flux($A - B - C$)/($A + B + C$) | -1/3 |
| Distance $A - B$ | 277 px |
| Distance $A - C$ | 277 px |
| Distance $Y_B - Y_C$ | 0 px |
| $\overline{S_{x1}} - \overline{S_{x2}}$ | 0 |

Table 5.1: Target values of each of the six observables, measured with the pupil data, that define the aligned position of the I-WFS.

In operational terms, this first alignment pertains to aligning the I-WFS with the telescope. This includes the initial alignment and any subsequent realignments needed to compensate for optical flexures or other movements. On the other hand, there exists a second alignment which focuses on correcting the LGS position on the sky. This correction accounts for variations in focus or jitters of the LGS. Practically speaking, these movements result in a shift of the LGS image on the I-WFS, causing changes in both flux and signals. It's important to highlight that alterations in the source's on-sky position do not lead to shifts in the positions of the pupils. The pupils' positions are solely influenced by the relative alignment between the I-WFS and the telescope.

Calibration Procedure: Interaction Matrix and Control Matrix

The alignment procedure is based on a linear approximation approach similar to that commonly used in AO closed-loop theory. Let's define a vector \vec{D} containing values of the six degrees of freedom of the hexapod and a vector \vec{O} containing values of the six observables. Actually, \vec{D} corresponds to corrections of the positions of the six degrees of freedom and \vec{O} to differences between the measured observables and the target values. To compute the necessary hexapod movement \vec{D} from a certain measured observables vector \vec{O} , a Control Matrix (CM) is used. Its behaviour is fully described by the knowledge of the optical Interaction Matrix (IM) [32]. This matrix has information regarding the variation of the six observables due to

misalignments of the ingot prism with respect to the optical axis of the system. It's a 6×6 matrix where the i^{th} column is an observables vector \vec{O} corresponding to a unit movement of the hexapod on the i^{th} degree of freedom. We have:

$$\vec{O} = IM \times \vec{D} \tag{5.2}$$

Thereafter, the IM is pseudo-inverted in order to produce the CM, and the following relation applies:

$$\vec{D} = CM \times \vec{O} \tag{5.3}$$

This operation lets us know about \vec{D} the corrections of the positions of the six degrees of freedom for a certain vector \vec{O} of differences between the measured observables and the target values.

The procedure to obtain these matrices is called the calibration procedure from now on. In this procedure, the measurement of the IM and the calculation of the CM are automated through a dedicated Python routine, which uses a first rough alignment, the "Home Position", as a starting point for the calibration of the IM. Finally, the CM is used to reconstruct the misalignments of the system with respect to the target position in an iterative procedure.

5.2 OLED Screen: Simulating the LGS

The OLED screen is being used to simulate the LGS, taking advantage of its 128×64 pixels, making up 128 columns and 64 rows. To define the image to be displayed on the screen, a bitmap written in a C# file is specified. A bitmap is a method by which a display space such as a graphics image is defined, detailing the information of each of its pixels (or bits).

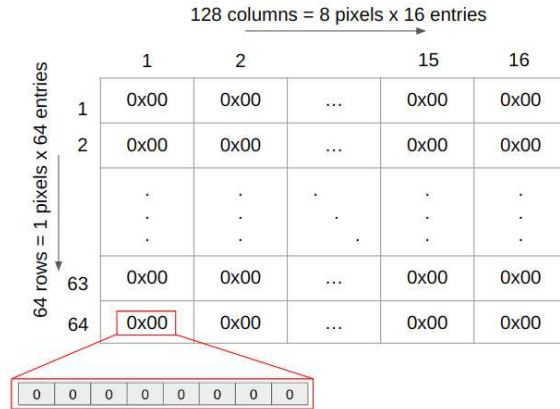


Figure 5.5: Schematic representation of the SSD1306 bitmap. It is a matrix of 16×64 entries, to illuminate the 128×64 pixels of the screen. Each entry consists of an hexadecimal number that controls the illumination of each group of eight adjacent pixels.

This bitmap consists of a matrix of 16×64 entries/bytes that are written in hexadecimal format, as illustrated in Figure 5.5. Each byte corresponds to 8 adjacent pixels. Hence, instead of 128 entries corresponding to the 128 columns, there are 16 entries, one for each set of 8 pixels in a row of the screen. Examples of possible entries are 0x00, for all pixels off and 0xFF for all on. To individually light up each of the 8 pixels, a byte 00000000 with

its 8 bits representing the 8 pixels from left to right needs to be converted to hexadecimal value, changing the corresponding pixel from 0 to 1. An example of this conversion is shown in Figure 5.6.

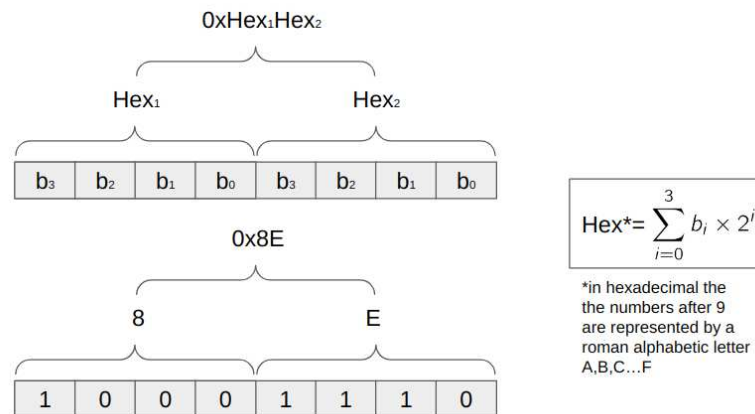


Figure 5.6: Each entry of the screen's bitmap is an hexadecimal number that controls the illumination of each group of eight adjacent pixels. To individually light up each of the 8 pixels, a byte 00000000 with its 8 bits representing the 8 pixels from left to right needs to be converted to hexadecimal value as illustrated here. The example of 8 pixels illuminated as 10001110 results in the entry 0x8E.

The bitmap required manual editing whenever a different source was needed on the screen. However, the operation of uploading the bitmap from the computer to the Arduino consumed approximately 40 seconds. As a result, this manual editing and uploading approach could not simulate real-time source changes effectively, which require faster speeds of the order of milliseconds. In light of this, our objective was to devise a faster method that could be seamlessly integrated into Python scripts.

On Figure 5.7, the steps of creating a OLED LGS source are illustrated. A total of eight integers are used to define the source, simply starting from the central pixel of the screen:

1. Vertical shift, **VS**: displacement of the centre of the source, in terms of number of rows, relative to the centre of the screen (1 row = 1 pixels). Negative integers signify movements towards the bottom of the screen, and positive integers signify movements to the top.
2. Thickness upwards, **TU**: number of extra rows above the centre of the source
3. Thickness downwards, **TD**: number of extra rows below the centre of the source
4. Horizontal shift, **HS**: displacement of the centre of the source, in terms of the number of columns (1 column = 8 pixels). Negative integers signify movements to the left, and positive integers signify movements to the right.
5. Length leftwards, **LL**: number of extra columns to the left of the centre of the source
6. Length rightwards, **LR**: number of extra columns to the right of the centre of the source

7. Discontinuities, **#D**: number of interruptions of the source's length, placed randomly along its extension. Each discontinuity corresponds to a vertical column switched off. $\#D \in 0, \dots, 7$
8. Contrast, **C**: a number $C \in 0, \dots, 255$ that indicates the brightness of the display.

A string command with the full characteristics of the source is then composed of: **VS, TU, TD, HS, LL, LR, #D, C**. This string is defined within the Python script on the computer and sent to the Arduino via a communication port that is kept open. The PySerial library² allows this communication to be made easily. The Arduino code takes these integers and fills an empty bitmap accordingly, immediately changing the screen display to the desired source. In addition, reverse communication is also possible. To know which source is currently on the screen, the Arduino can send a string with the source characteristics to the computer.

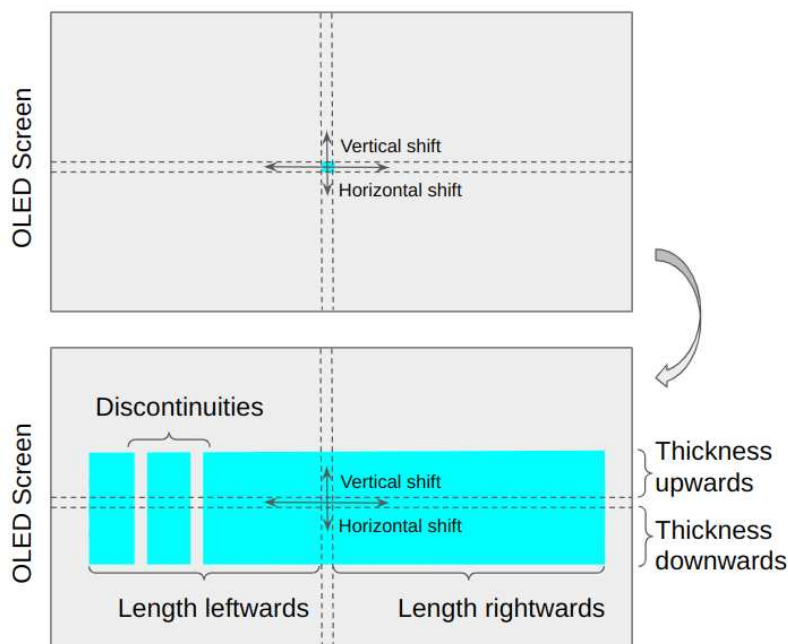


Figure 5.7: Representation of the settings required to define a LGS source on the OLED Screen. **Top**: Start with defining the vertical shift VS and horizontal shift HS of the centre of the LGS with respect to the centre of the screen. **Bottom**: Choose the length in columns to be added to the left LE and right LR, the thickness in rows to be added to the top TU and bottom TD and the number of vertical discontinuities $\#D$ to be added across the length of the LGS.

We will frequently mention a **standard source** which represents the most basic configuration: (0, 2, 2, 0, 7, 7, 0, 255). This source spans 128 columns and has a height of 5 rows. Typically, the system's reference position is established by aligning it with this source. Furthermore, the calibration process is predominantly conducted while this source is displayed on the screen.

At first glance, it looks like an overcomplicated procedure to define a source but, I would like to point that the advantage of this definition is that it can replicate all sorts of LGS changes and movements on sky: vertical changes of the centroid of the sodium layer, enlargement of the laser beacon due to seeing, decrease of the altitude of the highest edge of the sodium layer, increase of the altitude of the lowest edge of the layer.

²Available [here](#)

Nonetheless, there exists a significant limitation with this monochrome OLED display. The contrast setting is uniformly applied to the entire screen, leading to a reduction or increase in its overall brightness across all active pixels. Consequently, it is unable to replicate the density profile of sodium atoms, which would require distinct pixel brightness levels. Despite this drawback, for the subsequent alignment tests, this limitation does not pose an impediment, and thus, this screen configuration is retained.

5.2.1 Trial Alignments

Continuing from the ongoing work, we proceeded to assess the robustness of the automated alignment procedure. This was facilitated by the newly implemented in-script approach for altering the source displayed on the OLED screen. Initially, we focused on testing a single modification to the source configuration, which involved adjusting the source position perpendicularly to the optical axis, using the **VS** parameter.

Alignment of the I-WFS for different vertical shifts of the source

Given the approximate telecentric nature of the system, we anticipated that a movement of the source by one row (approximately 0.21 mm) would correspond to an analogous shift of the I-WFS along the Z axis. In other words, allowing the system to find the aligned position should result in a final (x, y, z) position that predominantly reflects a shift in the Z coordinate. The other coordinates of the aligned position should remain relatively constant.

The test procedure unfolded as follows: we displayed sources with varying VS values, spanning from -7 to $+7$, on the screen in random order. For each source, we initiated the alignment process, setting a fixed number of iterations $I_{max} = 10$. This meant that starting from the home position, the hexapod, coupled with the ingot, executed incremental movements to converge to a position where the observables matched the target values for the aligned position. The (X, Y, Z) positions were recorded at each iteration and visualized through plots, one for each coordinate axis. The ensuing plots illustrate the progression of each of the (X, Y, Z) positions during the alignment process for different sources, starting with the Z axis in Figure 5.8.

Beginning with the Z axis analysis, our focus was on comparing the final positions of each VS configuration at the last iteration with that of the standard source (VS=0, whose final position is identified on Figure 5.8 with a dashed line). As previously mentioned, a VS change of 1 is anticipated to correspond to a Z axis shift approximately equal to the height of one row on the screen. We evaluated the linearity of the alignment by fitting a linear function to the final values of $Z - Z_{\text{standard source}}$.

$$Z - Z_{\text{standard source}} = a \times VS + b \quad (5.4)$$

The fitted linear function parameters were determined as $a = -0.172$ mm and $b = -0.012$ mm. The data fit is depicted in Figure 5.9. Notably, the parameter a aligns with expectations, indicating that each increment of VS by 1 corresponds to a Z shift of -0.172 mm, effectively the height of one row. The standard deviation of this dataset from the linear fit stands at $\sigma = 0.018$ mm.

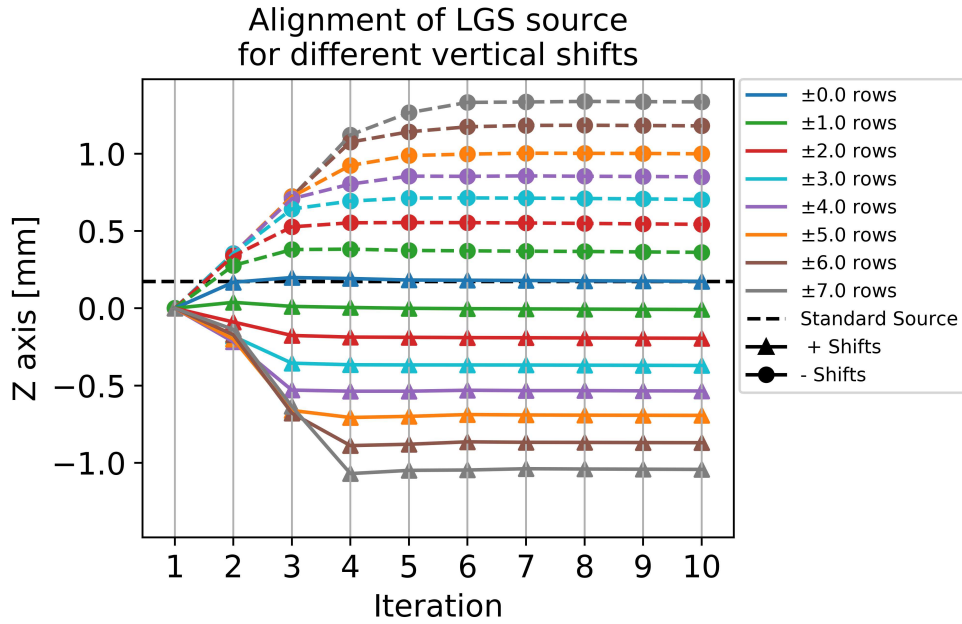


Figure 5.8: Plot depicts the progression of the Z position of the hexapod/ingot during the alignment process when different sources are placed on the screen. The y-axis represents the position on the Z axis of the hexapod, in mm, while the x-axis displays the iteration when that position was achieved. Each colour represents a source with different values of VS: positive VS are shown with continuous lines and triangular scatter points, while negative VS are represented with dashed lines and circular scatter points. The final position of the standard source $Z_{standard}$ ($VS = 0$) is highlighted.

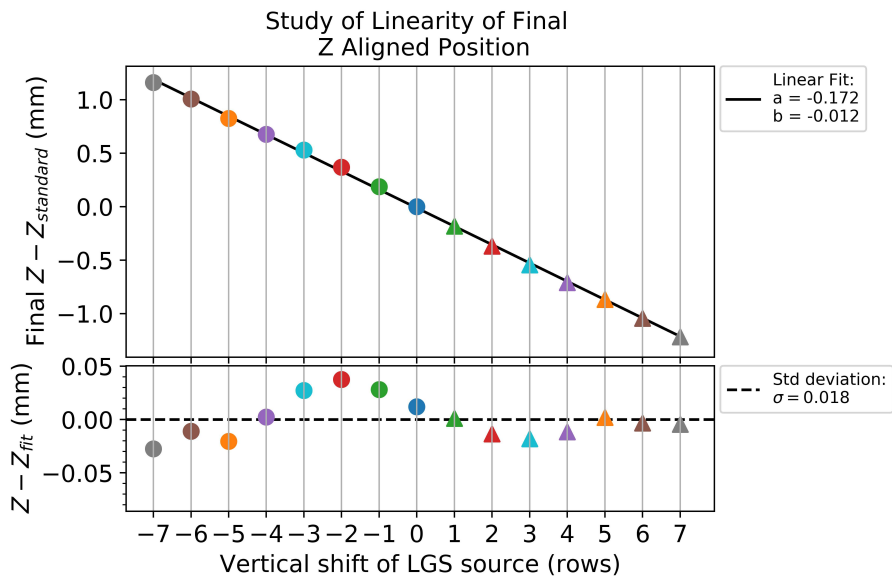


Figure 5.9: The data from Figure 5.8 is used. The x-axis displays the VS of the LGS source. The y-axis represents the Z axis position of the hexapod, in mm, at the end of the alignment with each source, relative to $Z_{standard}$. **Top:** Linear fit performed to the data with best fit parameters $a = -0.172\text{mm}$ and $b = -0.012\text{mm}$. **Bottom:** The residuals of the fit have a standard deviation of $\sigma = 0.018\text{mm}$.

Shifting our focus to the Y axis, a review of Figure 5.10 reveals that the hexapod consistently starts at the home position ($Y=0$) and, after a few iterations, moves to higher Y values, accumulating a $\Delta Y \approx 15$ mm shift for the source with $VS=+7$ rows. It subsequently reverses direction and approaches the aligned position. This phenomenon, termed Y overshoot, stems from the ingot's higher sensitivity on the y axis whenever there is a flux change in the pupils. Moreover, this hints at a degeneracy between the observables and the coordinates as the Y axis should be mostly related to horizontal movements rather than vertical movements of the source.

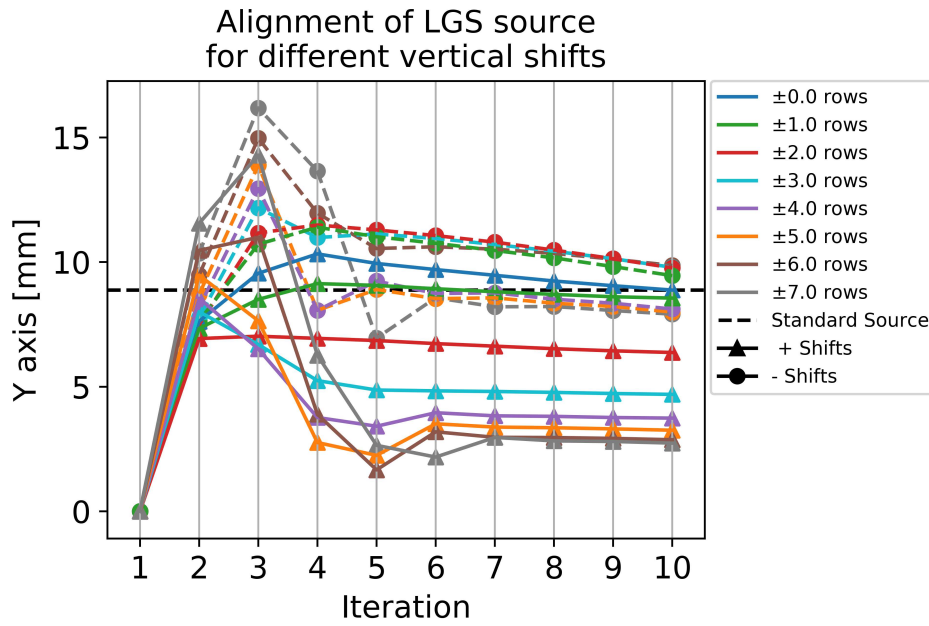


Figure 5.10: Plot depicts the progression of the Y position of the hexapod/ingot during the alignment process when different sources are placed on the screen. The y-axis represents the position on the Y axis of the hexapod, in mm, while the x-axis displays the iteration when that position was achieved. Each colour represents a source with different values of VS: positive VS are shown with continuous lines and triangular scatter points, while negative VS are represented with dashed lines and circular scatter points. The final position of the standard source $Y_{standard}$ ($VS = 0$) is highlighted.

Moving ahead, we proceeded to analyze the positions of each VS configuration at the last iteration relative to the standard source ($VS=0$, whose final position is identified on Figure 5.10 with a dashed line), this time in relation to the Y axis. We again applied a linear fit, this time to the final values of $Y - Y_{standard\ source}$.

$$Y - Y_{standardsource} = a \times VS + b \quad (5.5)$$

The fitted linear function parameters were determined as $a = -0.509$ mm and $b = -1.943$ mm, and the data fit is shown in Figure 5.11. The parameter a significantly deviates from zero, the expected value, and the standard deviation from the linear fit is high ($\sigma = 1.457$ mm), indicative of a non-flat relation. These trends cannot be attributed to simple tilts of the components because of the asymmetric pattern they reveal.

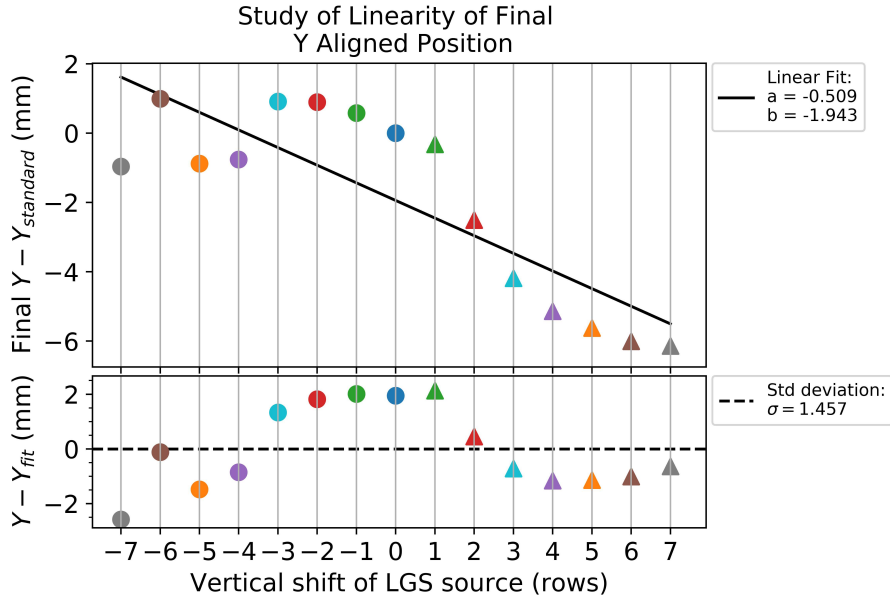


Figure 5.11: The data from Figure 5.10 is used. The x-axis displays the VS of the LGS source. The y-axis represents the Y axis position of the hexapod, in mm, at the end of the alignment with each source, relative to $Y_{standard}$. **Top:** Linear fit performed to the data with best fit parameters $a = -0.509$ mm and $b = -1.943$ mm. **Bottom:** The residuals of the fit have a standard deviation of $\sigma = 1.457$ mm.

Finally, we extended this analysis to the X axis alignment, as depicted in Figure 5.12. This analysis revealed hexapod movements of a smaller magnitude, approximately $\Delta X \approx 0.40$ mm, but final X positions that are not the same for sources with different VS, as would be expected.

Analyzing the positions of each VS configuration at the last iteration in relation to the standard source (VS=0, whose final position is labeled with a dashed line on Figure 5.12), we expected them to remain unchanged for different VS values. We again performed a linear fit, this time to the final values of $X - X_{standard\ source}$.

$$X - X_{standard\ source} = a \times VS + b \quad (5.6)$$

The fitted linear function parameters were determined as $a = -0.030$ mm and $b = -0.060$ mm, and the data fit is shown in Figure 5.13. The parameter a is smaller than the one found on the Y axis, and the standard deviation from the linear fit is relatively low ($\sigma = 0.049$ mm). However, non-symmetric deviations from the linear fit persist, following a pattern akin to the Y axis deviations.

An initial hypothesis investigated was the differential illumination of screen rows, caused by OLED pixel wear. Was the changing brightness of the screen rows affecting the aligned position? To verify this, we simulated vertical shifts by physically moving the screen stage while keeping the standard source on the screen. An analysis of the alignments, just as the one we just made, revealed the behaviours we were expecting: linear z movement and practically constant x and y positions for different vertical movements of the screen. More details about these test are presented in the next sections. This ruled out the illumination hypothesis, as a constant row was illuminated, eliminating brightness variation. The effect exists but is not determinant of the alignment position. Additionally, total screen brightness should not affect observables since fluxes are normalized.

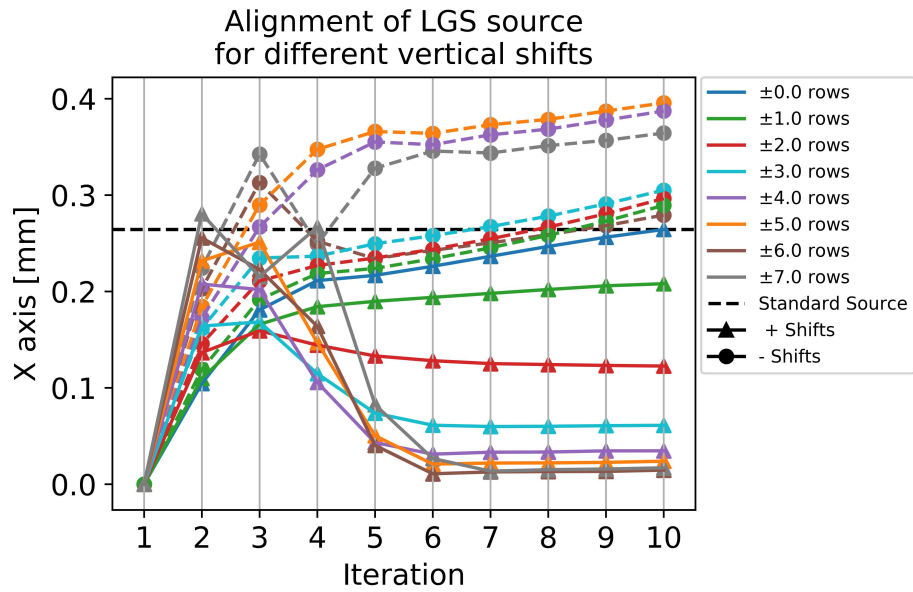


Figure 5.12: Plot depicts the progression of the X position of the hexapod/ingot during the alignment process when different sources are placed on the screen. The y-axis represents the position on the X axis of the hexapod, in mm, while the x-axis displays the iteration when that position was achieved. Each colour represents a source with different values of VS: positive VS are shown with continuous lines and triangular scatter points, while negative VS are represented with dashed lines and circular scatter points. The final position of the standard source $X_{standard}$ ($VS = 0$) is highlighted.

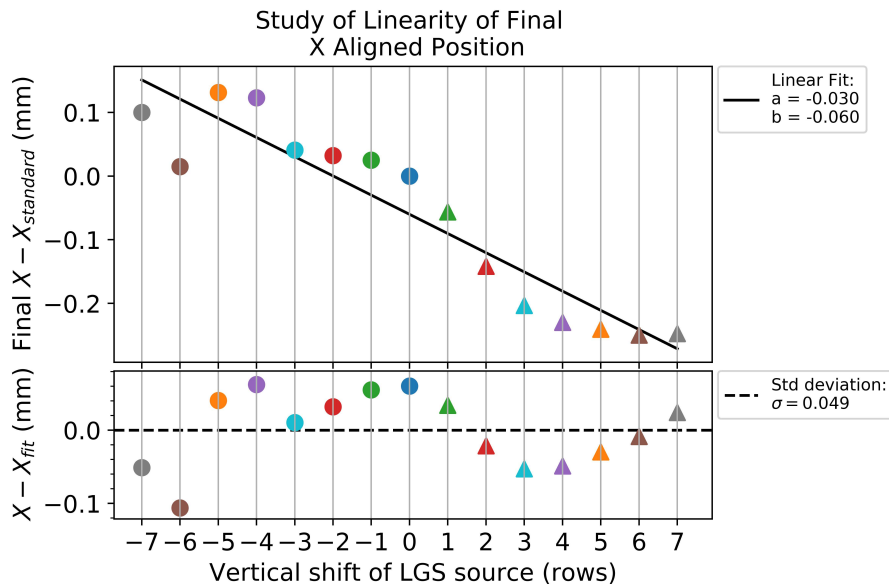


Figure 5.13: The data from Figure 5.12 is used. The x-axis displays the VS of the LGS source. The y-axis represents the X axis position of the hexapod, in mm, at the end of the alignment with each source, relative to $X_{standard}$. **Top:** Linear fit performed to the data with best fit parameters $a = -0.030$ mm and $b = -0.060$ mm. **Bottom:** The residuals of the fit have a standard deviation of $\sigma = 0.049$ mm.

Another factor related to the screen itself likely influenced the symmetry of vertical shifts. Later we discovered that indeed the screen's side profile, as viewed from the pupil, was not homogeneous, as shown in Figure 5.14 (left). Illuminating different rows introduced sources with distinct vertical displacement and side profiles. Consequently, the aligned position also varied on the X-Y plane of the ingot. To mitigate this inhomogeneity, a black non-reflective tape was applied to cover most of the screen's side, achieving homogeneity while minimizing lateral profile size. The image of the covered side profile of the screen is shown on Figure 5.14 (right).

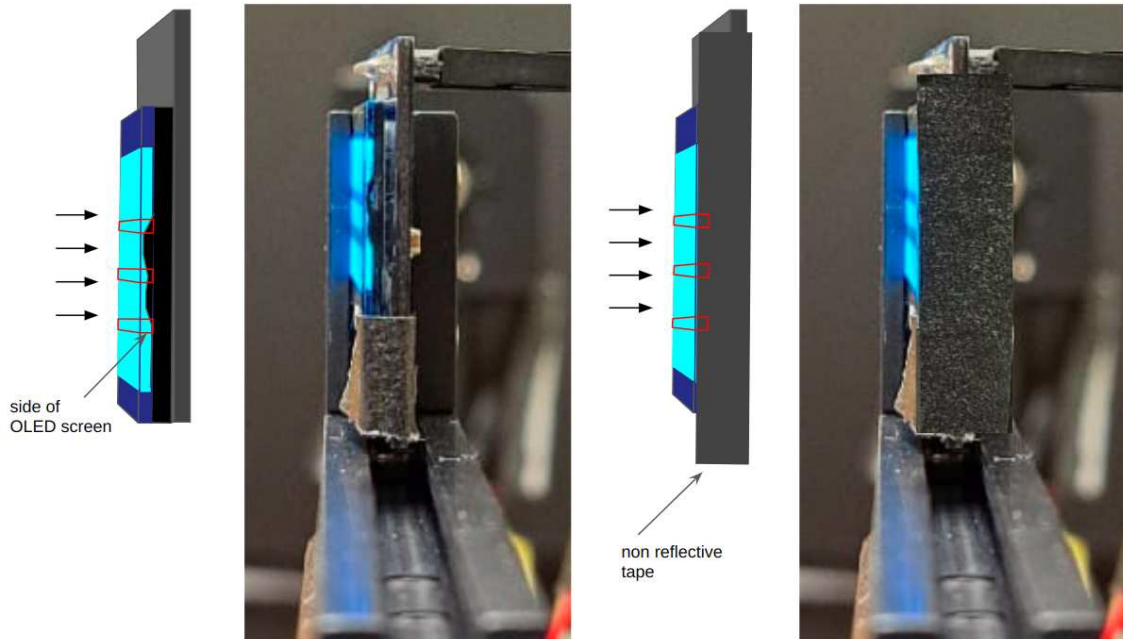


Figure 5.14: **Left:** OLED screen side as seen from the pupil. The side of the screen is covered with a black material in a non uniform way. Different rows of the screen reveal different side profiles, as highlighted by the red boxes. **Right:** A black non-reflective tape was applied to cover most of the screen's side. Different rows of the screen now reveal similar and very thin side profiles, as highlighted by the red boxes. Arrows indicate the front face of the screen.

Repeating the routine alignments with sources that have different vertical positions, the progression of each of the (X, Y, Z) positions during the alignment process for different sources are shown in Figures 5.15, 5.17, 5.19.

Beginning with the Z axis analysis, we again compared the final positions of each VS configuration at the last iteration with that of the standard source ($VS=0$, whose final position is identified on Figure 5.15 with a dashed line). As previously mentioned, a VS change of 1 is anticipated to correspond to a Z axis shift approximately equal to the height of one row on the screen.

The fitted linear function parameters were determined as $a = -0.176$ mm and $b = 0.571$ mm. The data fit is depicted in Figure 5.16. Notably, the parameter a aligns with expectations, indicating that each increment of VS by 1 corresponds to a Z shift of -0.176 mm, effectively the height of one row. The standard deviation of this dataset from the linear fit stands at $\sigma = 0.043$ mm, slightly bigger than the previous analysis. The residuals of the linear fit, plotted on the bottom of the same figure, show the same asymmetric pattern present until now.

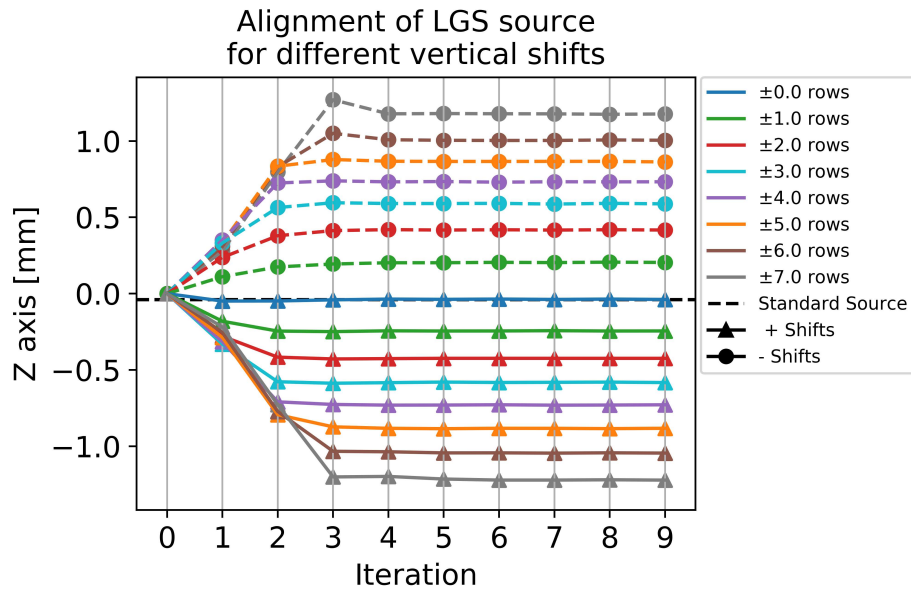


Figure 5.15: Plot depicts the progression of the Z position of the hexapod/ingot during the alignment process when different sources are placed on the screen. The y-axis represents the position on the Z axis of the hexapod, in mm, while the x-axis displays the iteration when that position was achieved. Each colour represents a source with different values of VS: positive VS are shown with continuous lines and triangular scatter points, while negative VS are represented with dashed lines and circular scatter points. The final position of the standard source $Z_{standard}$ ($VS = 0$) is highlighted.

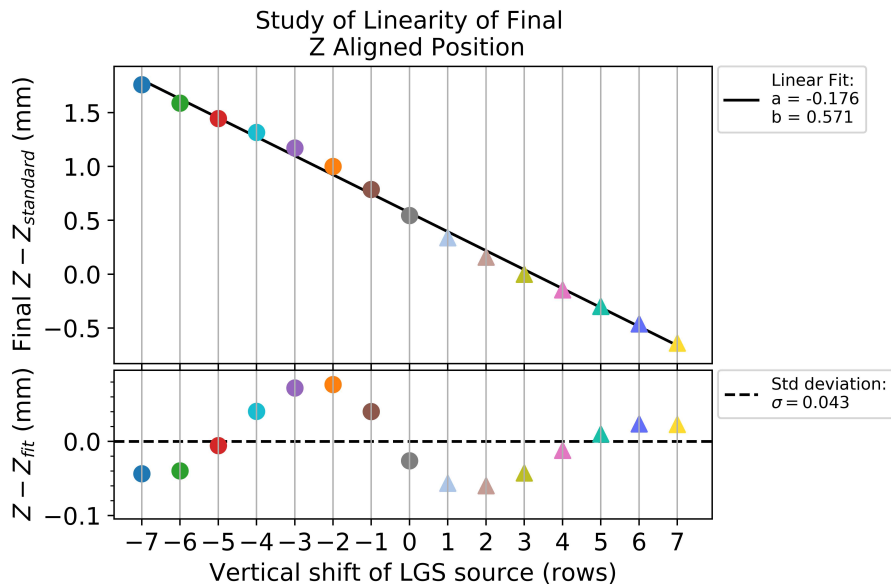


Figure 5.16: The data from Figure 5.15 is used. The x-axis displays the VS of the LGS source. The y-axis represents the Z axis position of the hexapod, in mm, at the end of the alignment with each source, relative to $Z_{standard}$. **Top:** Linear fit performed to the data with best fit parameters $a = -0.176$ mm and $b = 0.571$ mm. **Bottom:** The residuals of the fit have a standard deviation of $\sigma = 0.043$ mm.

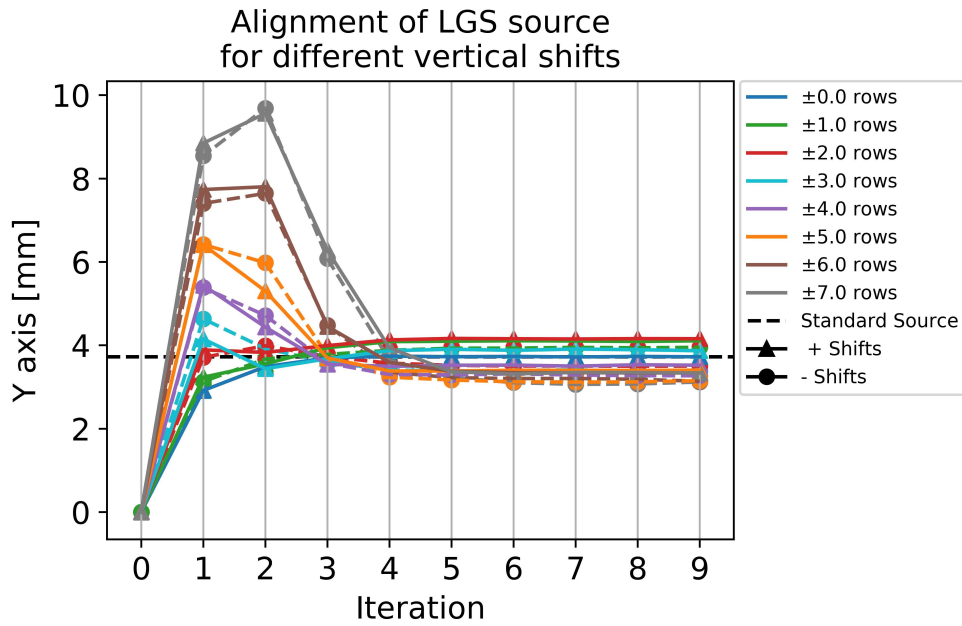


Figure 5.17: Plot depicts the progression of the Y position of the hexapod/ingot during the alignment process when different sources are placed on the screen. The y-axis represents the position on the Y axis of the hexapod, in mm, while the x-axis displays the iteration when that position was achieved. Each colour represents a source with different values of VS: positive VS are shown with continuous lines and triangular scatter points, while negative VS are represented with dashed lines and circular scatter points. The final position of the standard source $Y_{standard}$ ($VS = 0$) is highlighted.

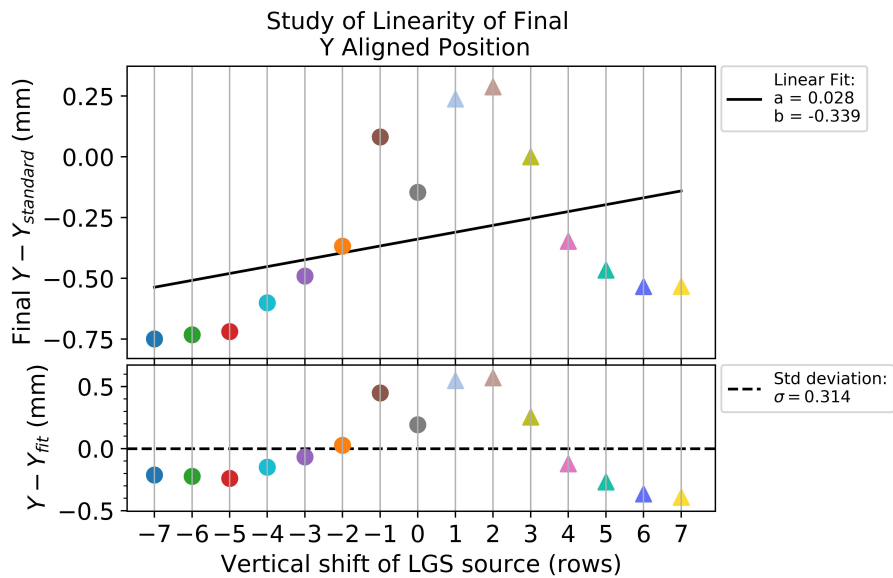


Figure 5.18: The data from Figure 5.17 is used. The x-axis displays the VS of the LGS source. The y-axis represents the Y axis position of the hexapod, in mm, at the end of the alignment with each source, relative to $Y_{standard}$. **Top:** Linear fit performed to the data with best fit parameters $a = 0.028$ mm and $b = -0.339$ mm. **Bottom:** The residuals of the fit have a standard deviation of $\sigma = 0.314$ mm.

Shifting our focus to the Y axis, a review of Figure 5.17 reveals a Y overshoot of $\Delta Y \approx 10$ mm shift for the source with $VS=+7$ rows. This effect was not eliminated when the screen was covered as it is a consequence of the intrinsic sensitivity and degeneracy of the observables and coordinates axis. One effect we do notice is that the span of the final y positions has decreased relative to the previous study, from ~ 7.5 mm to ~ 1 mm.

Moving ahead, we proceeded to analyze the positions of each VS configuration at the last iteration relative to the standard source ($VS=0$, whose final position is again identified on Figure 5.17 with a dashed line). We again applied a linear fit whose parameters were determined as $a = 0.028$ mm and $b = -0.339$ mm, and the data fit is shown in Figure 5.18. The parameter a 's deviation from zero has been significantly reduced and the standard deviation from the linear fit ($\sigma = 0.314$ mm) too. We highlight the presence of the asymmetric pattern on the residuals of the fit.

Finally, we extended this analysis to the X axis alignment, as depicted in Figure 5.19. This analysis revealed hexapod movements of a smaller magnitude, approximately $\Delta X \approx 0.40$ mm, as before.

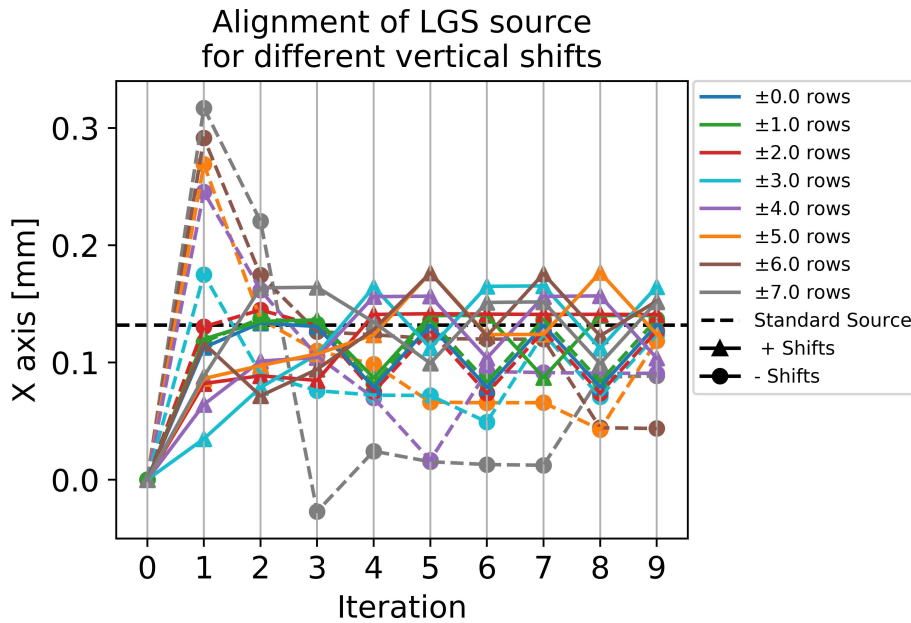


Figure 5.19: Plot depicts the progression of the X position of the hexapod/ingot during the alignment process when different sources are placed on the screen. The y-axis represents the position on the X axis of the hexapod in millimetres, while the x-axis displays the iteration when that position was achieved. Each colour represents a source with different values of VS: positive VS are shown with continuous lines and triangular scatter points, while negative VS are represented with dashed lines and circular scatter points. The final position of the standard source ($VS = 0$) is highlighted.

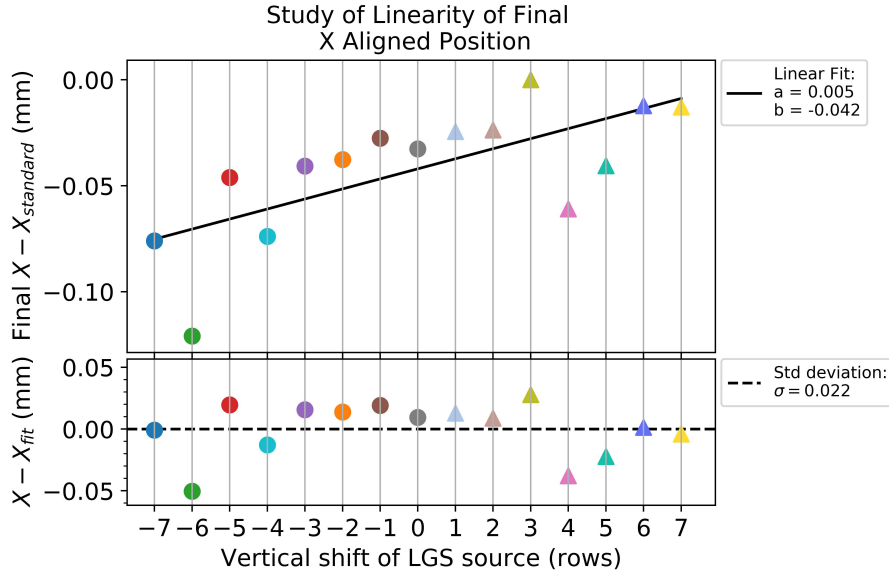


Figure 5.20: The data from Figure 5.19 is used. The x-axis displays the VS of the LGS source. The y-axis represents the X axis position of the hexapod, in mm, at the end of the alignment with each source, relative to $X_{standard}$. **Top:** Linear fit performed to the data with best fit parameters $a = 0.005$ mm and $b = -0.042$ mm. **Bottom:** The residuals of the fit have a standard deviation of $\sigma = 0.022$ mm.

Analyzing the positions of each VS configuration at the last iteration in relation to the standard source (VS=0, whose final position is labeled with a dashed line on Figure 5.19), we expected them to remain unchanged for different VS values. We again performed a linear fit whose parameters were determined to be $a = 0.005$ mm and $b = -0.042$ mm, and the data fit is shown in Figure 5.20. The parameter a is smaller than the one found on the Y axis, and the standard deviation from the linear fit is relatively low ($\sigma = 0.022$ mm). Moreover, both these quantities have been reduced with the introduction of the screen side cover, revealing that indeed the inhomogeneities were affecting the alignment.

To summarise the results, we show in Table 5.2 the fit parameters from before and after the screen was covered to correct for inhomogeneities. We have concluded that the side profile of the LGS has an effect on the aligned position in the Y and X axis of the ingot and have managed to reduced this screen's impact on the results. After corrections, the ingot's alignment behaves as expected: vertical shifts are linearly related to the Z axis position, whereas X and Y axis positions are relatively independent from vertical shifts of the source.

However, the Y overshoot behaviour and the asymmetric trend in the residuals have not been eliminated nor reduced, as they are not related to the screen's characteristics. The first one derives from the intrinsic hypersensitivity of the Y axis to changes of the flux in the pupils and degeneracy between some observables. The asymmetric pattern could be related to the lack of precision of the current alignment algorithm. To amend this last point, we aimed at developing a new alignment procedure that could reach more precise aligned conditions.

| | Before Tape (mm) | After Tape (mm) |
|-------------|------------------|------------------|
| X_{ingot} | $a = -0.030$ | $a = 0.005$ |
| | $b = -0.060$ | $b = -0.042$ |
| | $\sigma = 0.049$ | $\sigma = 0.022$ |
| Y_{ingot} | $a = -0.509$ | $a = 0.028$ |
| | $b = -1.943$ | $b = -0.339$ |
| | $\sigma = 1.457$ | $\sigma = 0.314$ |
| Z_{ingot} | $a = -0.172$ | $a = -0.176$ |
| | $b = -0.012$ | $b = 0.571$ |
| | $\sigma = 0.018$ | $\sigma = 0.043$ |

Table 5.2: Parameters a and b obtained from the linear fits of the current section, together with the standard deviation σ of the fit. The values of these parameters before and after the OLED screen was covered with tape are displayed side by side for easier comparison.

5.3 New Alignment Procedure

The initial alignment procedure was governed by a "for" loop structure. To comprehend the modifications introduced into the alignment process, we provide additional elaboration on the former approach. Starting with a misaligned system, the hexapod is, before anything else, moved to the Home position. This position is predefined on the system. Then, using the pupil extraction algorithm, the observables of the three pupils of the ingot are calculated. Next, using the CM, resulting from an initial calibration with the standard source, the necessary corrections to the hexapod's position are computed. This sequence constitutes the first iteration of the alignment process. These steps are iterated upon until the maximum number of iterations, as set by the user, is reached. Subsequently, the system records the final positions of the hexapod and the observables of the ingot in that particular configuration. The steps of this process are better illustrated in Figure 5.21.

The main issue associated with this procedure is that the alignment routine ended once the specified number of iterations was completed, regardless of the attained final position and observable values of the three pupils. This approach occasionally led to the system oscillating around the aligned position without converging. Moreover, there were instances where the system was in close proximity to the aligned position, only to diverge from it and continue until the maximum iteration count was reached.

To address these challenges and to develop a potentially faster routine, the conventional "for" loop has been replaced with a "while" loop. Within this new approach, the alignment process continues running as long as the observables fall outside a predefined range of acceptable values for the aligned position. Figure 5.22 aims at illustrating the different steps of the process, which we now also further detail:

1. Starting with a misaligned system, perform an initial movement of the hexapod, constituting the "zero" iteration.
2. Employ the extraction algorithm to compute the observables of the three pupils of the ingot.
3. Compare these observables with predefined boundaries.
 - a. If they fall within these boundaries, the configuration is recognised as aligned, and the loop terminates.
 - b. If not, the CM is utilised to calculate a new position for the hexapod, which then moves to that position.
4. Continue this procedure while consistently checking against the predefined boundaries.
5. If alignment hasn't been achieved after 15 iterations, execute a new calibration, obtaining a CM, this time utilizing the current source displayed on the Screen. This generated CM is temporary and is solely used for the ongoing alignment process. Furthermore, this step is performed only once.
6. If 15 additional iterations using the new temporary CM still fail to achieve alignment, the system exits the loop and is flagged as misaligned.

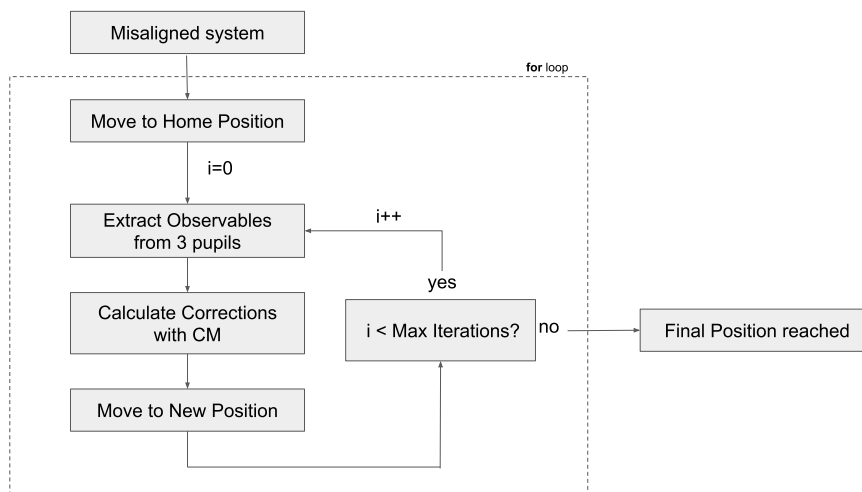


Figure 5.21: Steps of the alignment performed with a "for" loop are detailed.

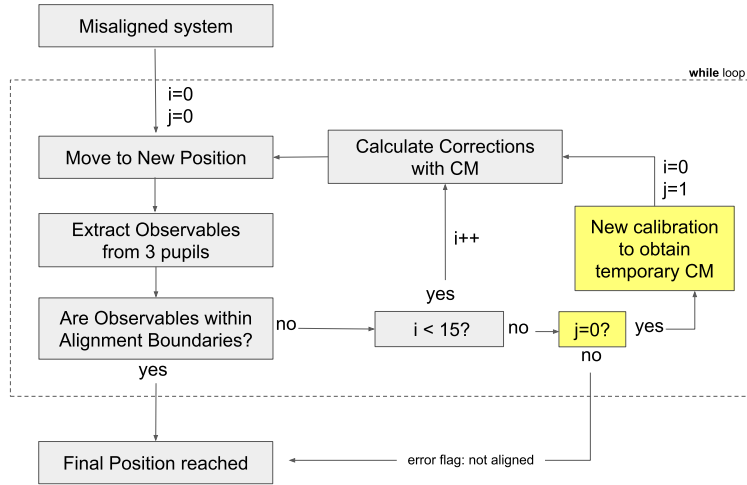


Figure 5.22: Steps of the alignment performed with a "while" loop are detailed.

The selection of boundaries for the aligned position needs a comprehensive analysis of typical aligned positions' variance. To accomplish this, the initial "for" loop with $l_{max} = 10$ is employed, collecting the final aligned positions and observables from 194 sources that exhibited slight variations. For each observable, histograms portraying the frequency distribution of obtained values around the target value are plotted (Figure 5.23). To determine the mean value μ and standard deviation σ of each observable, a gaussian function $f(x; \mu, \sigma)$ is fitted to the values of the observable x . The outcome of these adjustments are presented in Table 5.3.

$$f(x; \mu, \sigma) = \frac{1}{\sigma\sqrt{2\pi}} e^{-\frac{(x-\mu)^2}{2\sigma^2}} \quad (5.7)$$

Taking a closer look at the distribution of values, we can see that the observables linked to distances consistently fall within the range of about ± 1 pixel from the intended value. Smaller values don't align with physical reality due to the camera's precision being exactly 1 pixel. Among the 194 tests conducted, hardly any aligned positions went beyond the 1-pixel threshold. This strongly suggests that it's logical to set the boundary for accepting an aligned position precisely at ± 1 pixel.

Shifting our focus to the observables tied to flux and counts, things get more complex. It's important to note that these values are expressed as percentages. The initial observable quantifies how much more light the reflected pupil C has in comparison to pupil B. The distribution of values is centered around 0, indicating equal flux between pupils, but with a standard deviation of 0.58. One particular instance stands out, where $\text{Flux}(C - B) \sim 7.5\%$. However, this seems more like an outlier resulting from random errors rather than a reflection of alignment quality. A similar pattern emerges with $\text{Flux}(A - (B + C))$, displaying a broader distribution centered around -33.45% . This observable reflects the ratio of transmitted to reflected light. Although $\sigma = 1.35$, most counts are closely clustered around the average value. This implies that even though 68.27% of alignments fall within $\sigma = 1.35$, most runs achieve even more precise alignments, very close to the target value. This same trend is also observed in the histogram for $\overline{S_{x1}} - \overline{S_{x2}}$.

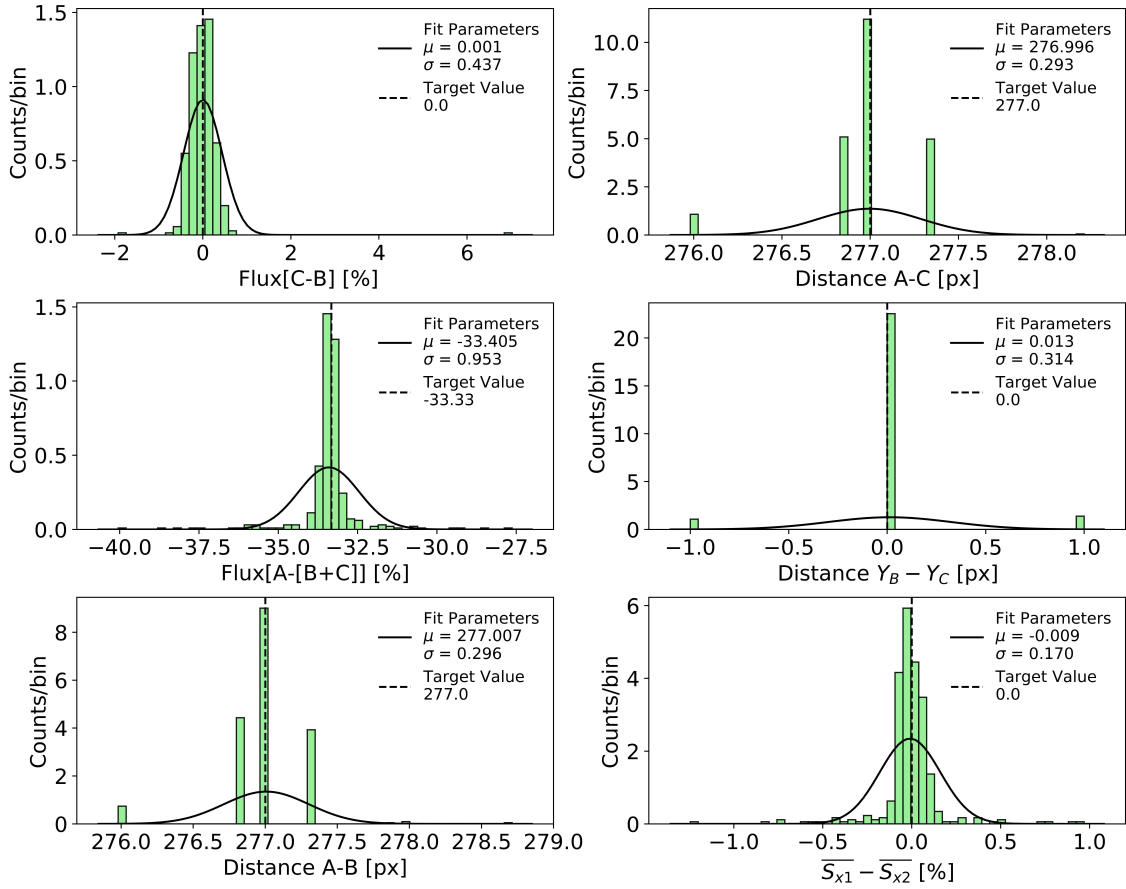


Figure 5.23: The final values of the observables obtained at the end of each of the 194 alignments (with "for" loop, $l_{max} = 10$) are displayed in six histograms. Each histogram shows the distribution of values around the target value of each observable. The gaussian function 5.7 is fitted to the histograms and the best fit parameters are shown both here and on Table 5.3.

When it comes to setting the boundaries, we could potentially consider using these σ values. However, our objective is to devise a more accurate alignment method. Consequently, our boundaries should be even stricter than σ , ensuring a meaningful transition to a "while" loop.

After meticulously excluding certain outliers from the distribution by establishing limits beyond which random errors in the procedure might occur, we conducted new gaussian fits, presented on Figure 5.24. This enabled us to calculate new means and sigmas. These updated values and the chosen limits are also presented in Table 5.3.

Here, we have a practical distribution that showcases the actual alignment capabilities our system can achieve. The boundaries we set should generally be narrower than σ , except for the case of distance where values smaller than 1 pixel aren't physically meaningful. We can choose to make these boundaries tighter or looser depending on the scenario. In this context, we've decided on tighter boundaries for the second and sixth observables, while the first observable has a boundary larger than σ . This decision stems from the realization that the first observable is particularly reliant on the y axis position, which we've discovered is highly sensitive. Further constriction could potentially hinder successful convergence. The final selection of boundaries for each observable is as follows:

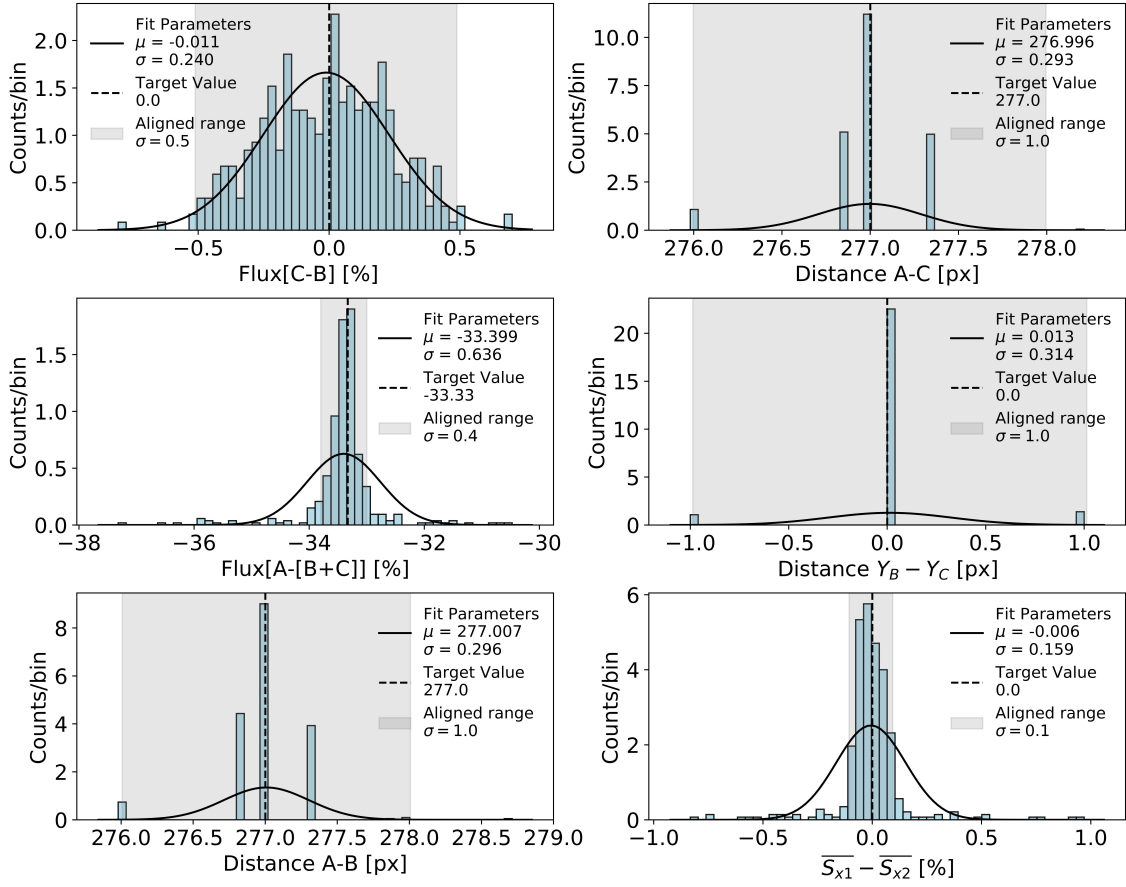


Figure 5.24: After defining limits to each observable and removing some outliers, the study of the distribution of aligned values can be repeated. Each histogram shows the distribution of values around the target value of each observable, which can now be compared to the boundaries of the aligned range. The gaussian function 5.7 is fitted to the histograms and the best fit parameters are shown both here and on Table 5.3.

| Observable | μ | σ | μ_{new} | σ_{new} | Limits | Boundary width |
|---------------------------------------------|--------|----------|-------------|----------------|----------------|----------------|
| Flux($C - B$) (%) | 0.03 | 0.58 | 0.00 | 0.25 | $[-1.5, 1.5]$ | 0.5 |
| Flux($A - B - C$) (%) | -33.45 | 1.35 | -33.44 | 0.91 | $[-37.5, -30]$ | 0.4 |
| Distance $A - B$ (px) | 277.01 | 0.40 | 277.01 | 0.40 | $[275, 279]$ | 1 |
| Distance $A - C$ (px) | 277.01 | 0.40 | 277.01 | 0.40 | $[275, 279]$ | 1 |
| Distance $Y_B - Y_C$ (px) | 0.01 | 0.41 | 0.01 | 0.41 | $[-2, 2]$ | 1 |
| $\overline{S_{x1}} - \overline{S_{x2}}$ (%) | -0.01 | 0.24 | 0.01 | 0.22 | $[-1, 1]$ | 0.1 |

Table 5.3: Parameters μ and σ obtained from the gaussian fits of histograms in Figures 5.23. The limits defined to rule out outliers are specified, together with the new parameters μ_{new} and σ_{new} obtained from the gaussian fits of histograms in Figures 5.24. The final boundaries of each observable that define the aligned range are here also specified.

Regarding the efficiency of the method, we can analyse the time that was needed to reach alignment and subdivide it into the different steps of the methods. This comparison is shown in Figure 5.25, with one run of each cycle. The times chosen to be plotted represent the following steps of the procedures:

1. Take Frame: the camera records 3 images of 1500 ms each, and averages them;
2. Detect Pupils: pupils coordinates and counts are extracted;
3. Get Observables: use pupils information to obtain observables and for the "while" loop, compare these with the boundaries;
4. Calculate movements and move hexapod: use CM to calculate necessary movements and make hexapod move.

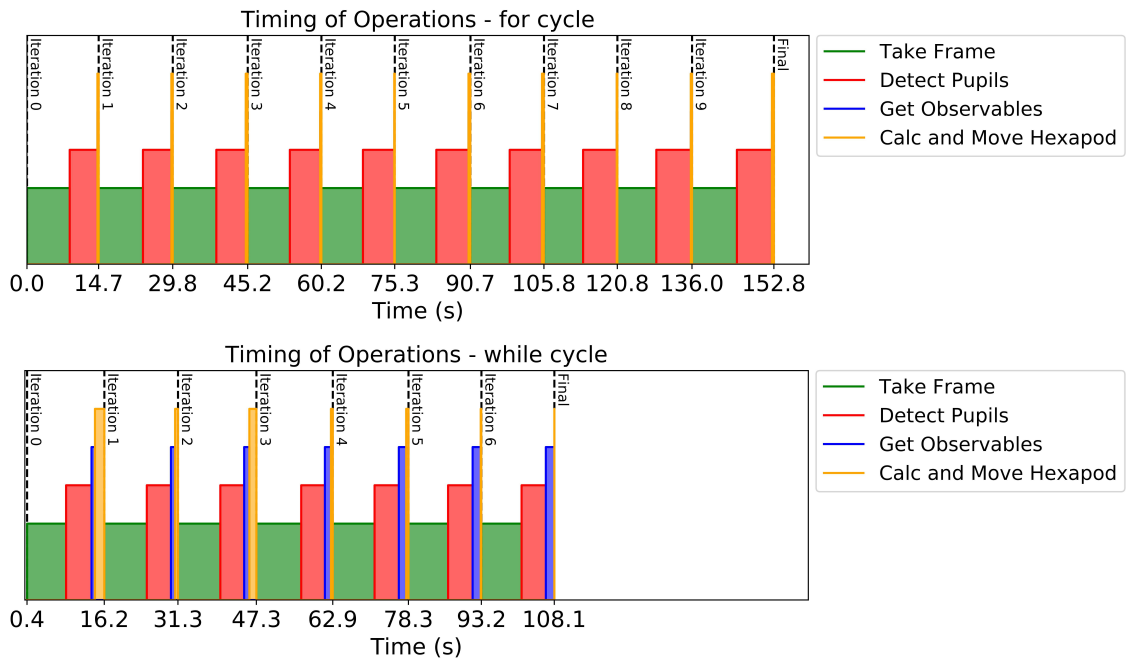


Figure 5.25: The duration of the two alignment cycles is compared by registering the time interval between iterations. Each iteration is further divided in four operations: Take Frame, Detect Pupils, Get Observables, Calculate Movements and Move Hexapod. To each operation corresponds a step with a height that carries no meaning other than to aid visualisation.

Although in Figure 5.25 each iteration of the while cycle took longer, the number of iterations was reduced from 10 to 7. Furthermore, the third operation "Get Observables" (shown in blue) consistently takes longer in the while cycle, while it is barely relevant on the for cycle when compared to the other steps. This is because of the verification that is made at every single iteration to check if the observables have reached the desired boundaries.

5.3.1 Continuation: Robustness of the Alignment

After the above mentioned modifications were incorporated, we continued to test the robustness of the automatised alignment procedure, taking advantage now of the in-script method of changing the source on the OLED screen, the while condition for Alignment and the OLED screen covering to obtain homogenous side profiles of the source. In particular, the following variations of the source were tested:

1. Shifts of the source perpendicular to the optical axis, using the **VS** parameter;
2. Shifts of the source parallel to the optical axis, using the **HS** parameter;

Besides the alignments that were performed by changing the LGS on the screen, we simulated vertical and horizontal shifts by physically moving the screen stage while keeping the standard source on the screen. As shown in Figure 5.26, the OLED screen is mounted on a stage that can be moved vertically and horizontally with great precision.

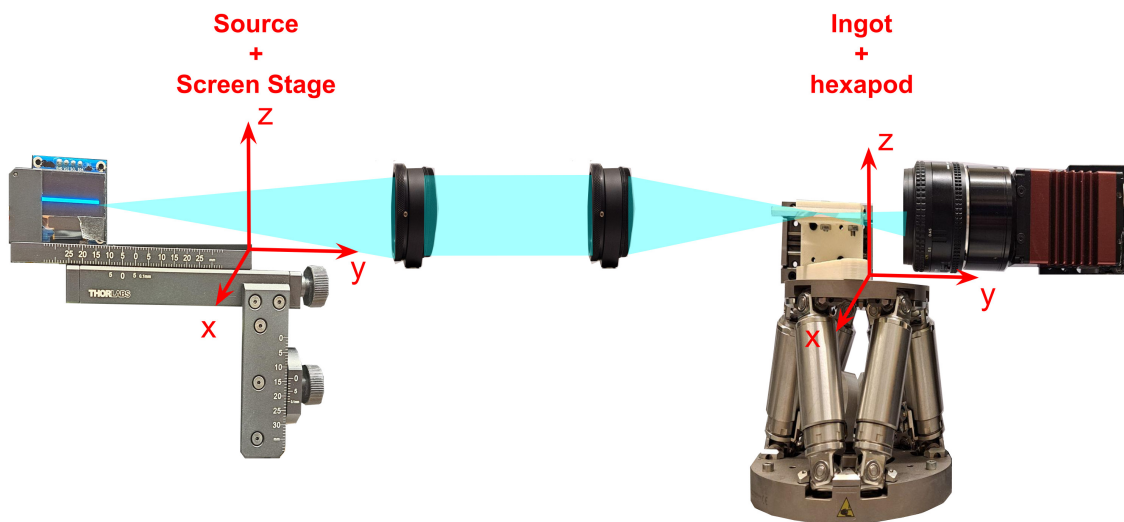


Figure 5.26: The two important coordinate axis are illustrated in this schematic representation. The source position is specified by $(X, Y, X)_{source}$, and it can be changed by altering the parameters of the OLED Screen bitmap or by physically moving the screen stage with the horizontal and vertical scales here shown. On the other end, the ingot, attached to the hexapod, has a position defined by $(X, Y, Z)_{ingot}$. For simplicity, the Scheimpflug plane inclinations aren't displayed here.

The goal is to compare the two sets of alignments given by the moving screen and the changing source, as they should be equivalent. This extra test is useful to rule out other irregularities of the screen such as slight inclinations relative to the optical axis. In the following three graphs, we show the final aligned position in each of the three X,Y,Z coordinate axis. Each alignment data point corresponds to the average of five alignments performed in the same configuration, with the "while" loop, and the error bars correspond to the standard deviation of the final positions.

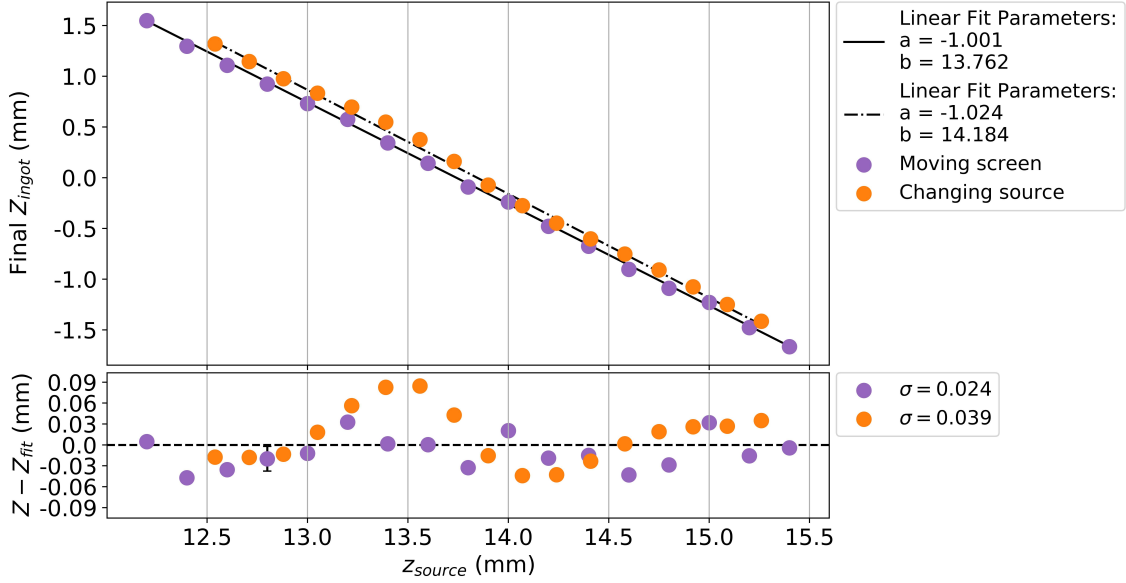


Figure 5.27: Results from two sets of alignments performed with "while" loop are plotted, for sources with different vertical shifts. Vertical shifts of the source, corresponding to a Z_{source} , were achieved by moving the screen vertically (purple dots) or by illuminating different rows of the screen (orange dots), now kept fixed. The x-axis displays the Z_{source} , in mm. The y-axis represents the final Z axis position of the ingot, in mm. **Top:** Linear fits performed to both sets of data, with best fit parameters $a = -1.001$ and $b = 13.762$ mm (moving screen) and $a = -1.024$ and $b = 14.184$ mm (changing source). **Bottom:** The residuals of the fits have a standard deviation of $\sigma = 0.024$ mm and $\sigma = 0.039$ mm, respectively.

Starting with vertical shifts, data points in orange correspond to sources with different VS parameter whereas purple data points correspond to a standard source on a screen that was displaced vertically. Each value of VS was converted to a physical vertical distance by using $1_{row} = 0.170$ mm. We evaluated the linearity of the alignment by fitting linear functions to the final values of Z for the moving screen data and the changing source data.

$$Z_{ingot} = a \times Z_{source} + b \quad (5.8)$$

The fitted linear function parameters and standard deviations of the residuals are displayed on the Table 5.4. The data fits are depicted in Figure 5.27. The parameter a is expected to be -1 for an optical layout with 1:1 magnification and notably it is $a = -1.001$ when the screen is moved and slightly smaller $a = -1.024$ when the source is changed.

Repeating a similar analysis to the Y positions, we quickly noticed a non linear trend of the data, both with a changing source and a moving screen. On the one hand, the changing source trend is similar to those already found in previous tests, related to the non-homogeneity of the screen. On the other hand, the moving screen seems to indicate that the best focus position has a field curvature. Field curvature describes the optical aberration in which a flat object normal to the optical axis cannot be brought properly into focus on a flat image plane. We evaluated the curvature of the aligned positions by fitting a second order function to the final values of Z for the moving screen data.

$$Y_{ingot} = a^2 \times Z_{source} + b \times Z_{source} + c \quad (5.9)$$

The best fit function parameters were determined to be $a = 0.105 \text{ mm}^{-1}$, $b = -2.881$ and $c = 20.995 \text{ mm}$, with standard deviations of $\sigma = 0.019 \text{ mm}$. These values are displayed on Table 5.4. The data fit is depicted in Figure 5.28. The parameter a should dictate the field curvature and was compared with ray-tracing simulations, $a_{simulations} = 0.0415 \text{ mm}^{-1}$. This indicates that the polynomial trend is only partially due to optical aberrations. Other optical effects, for now unknown, are contributing to it.

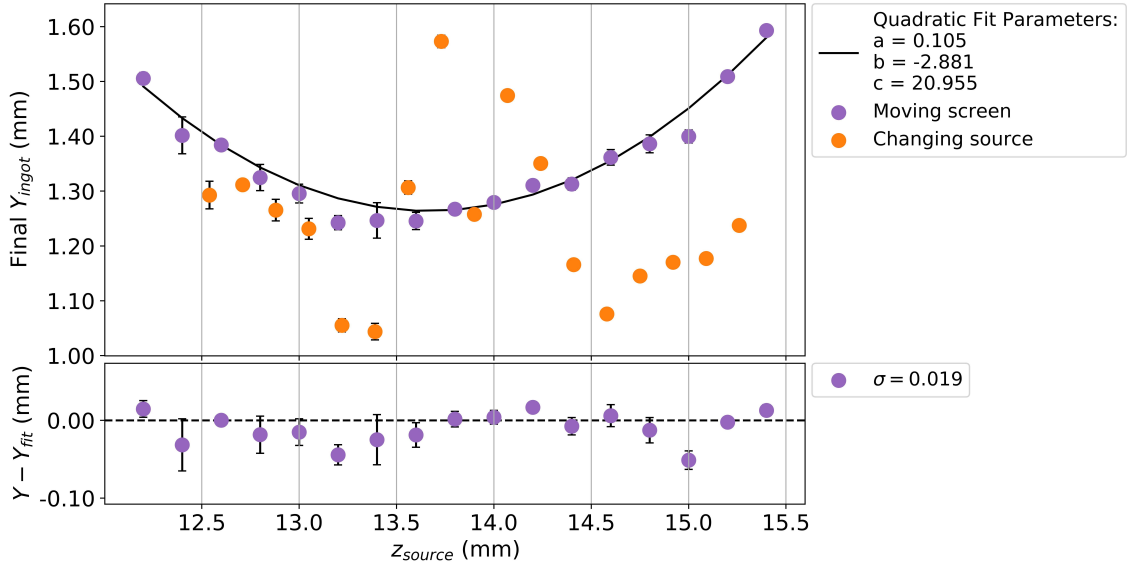


Figure 5.28: Results from two sets of alignments performed with "while" loop are plotted, for sources with different vertical shifts. Vertical shifts of the source, corresponding to a Z_{source} , were achieved by moving the screen vertically (purple dots) or by illuminating different rows of the screen (orange dots), now kept fixed. The x-axis displays the Z_{source} , in mm. The y-axis represents the final Y axis position of the ingot, in mm. **Top:** Quadratic fit performed to the moving screen data, with best fit parameters $a = 0.105 \text{ mm}^{-1}$, $b = -2.881$ and $c = 20.955 \text{ mm}$. **Bottom:** The residuals of the fit have a standard deviation of $\sigma = 0.019 \text{ mm}$.

Moving on to the x axis, we evaluated the linearity of the alignment by fitting linear functions to the final values of X for the moving screen data and the changing source data.

$$X_{ingot} = a \times Z_{source} + b \quad (5.10)$$

The fitted linear function parameters and standard deviations of the residuals are displayed on the Table 5.4. The data fits are depicted in Figure 5.29. The parameter a is expected to be 0, as the x coordinate of the ingot should be independent of the vertical movement of the source, unless the screen plane itself is tilted with respect to the optical axis. From the fits it was found to be $a = 0.031$ when the screen is moved and slightly smaller $a = 0.016$ when the source is changed. The inclination of the screen seems to be present but is very small and this linear fit can be used to correct for the positions obtained in future alignments.

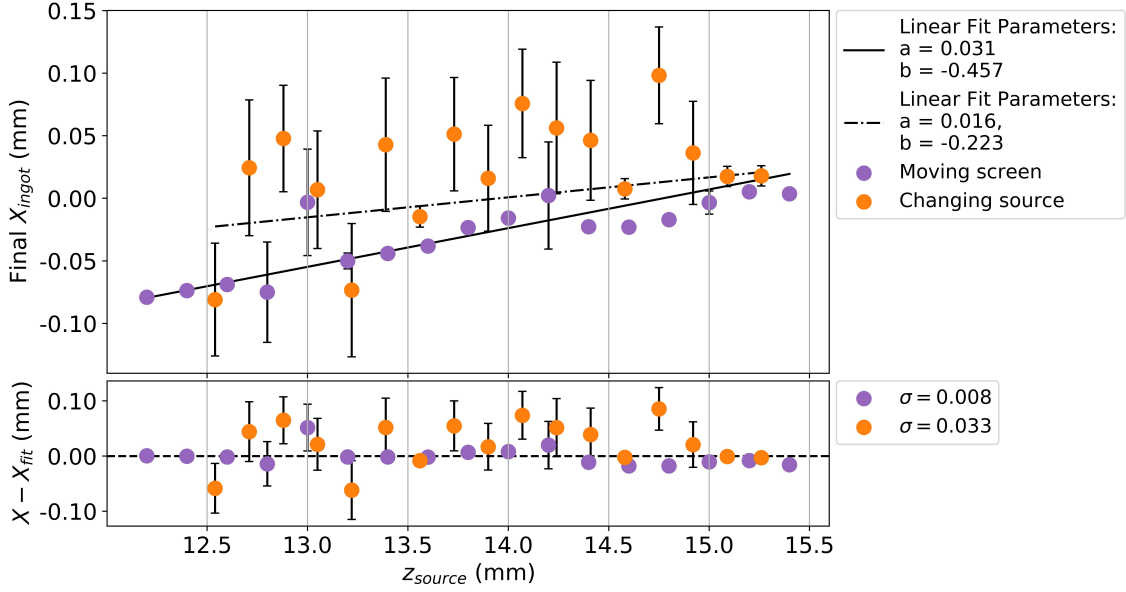


Figure 5.29: Results from two sets of alignments performed with "while" loop are plotted, for sources with different vertical shifts. Vertical shifts of the source, corresponding to a Z_{source} , were achieved by moving the screen vertically (purple dots) or by illuminating different rows of the screen (orange dots), now kept fixed. The x-axis displays the Z_{source} , in mm. The y-axis represents the final X axis position of the ingot, in mm. **Top:** Linear fits performed to both sets of data, with best fit parameters $a = 0.031$ and $b = -0.457$ mm (moving screen) and $a = 0.016$ and $b = -0.223$ mm (changing source). **Bottom:** The residuals of the fits have a standard deviation of $\sigma = 0.008$ mm and $\sigma = 0.033$ mm, respectively.

Next, we analyse the alignment for horizontal shifts (along the optical axis) of the LGS. Once again, data points in orange correspond to sources with different HS parameter whereas purple data points correspond to a standard source on a screen that was displaced horizontally along the optical axis. Each value of HS was converted to a physical horizontal distance by using 1 column = 0.170 mm. We evaluated the linearity of the alignment by fitting linear functions to the final values of Z for the moving screen data and the changing source data.

$$Z_{ingot} = a \times y_{source} + b \quad (5.11)$$

The fitted linear function parameters and standard deviations of the residuals are displayed on the Table 5.4. The data fits are depicted in Figure 5.30. The parameter a is expected to be 0 for sources perfectly aligned with the optical axis. Horizontal movements of the source shouldn't affect the z coordinate of the aligned position unless the screen is tilted and the source is not strictly parallel. In fact, we found that $a = -0.001$ when the screen is moved and $a = 0.010$ when the source is changed, revealing a very small inclination.

Regarding the y coordinates, we evaluated the linearity of the alignment by fitting linear functions to the final values of Y for the moving screen data and the changing source data.

$$Y_{ingot} = a \times y_{source} + b \quad (5.12)$$

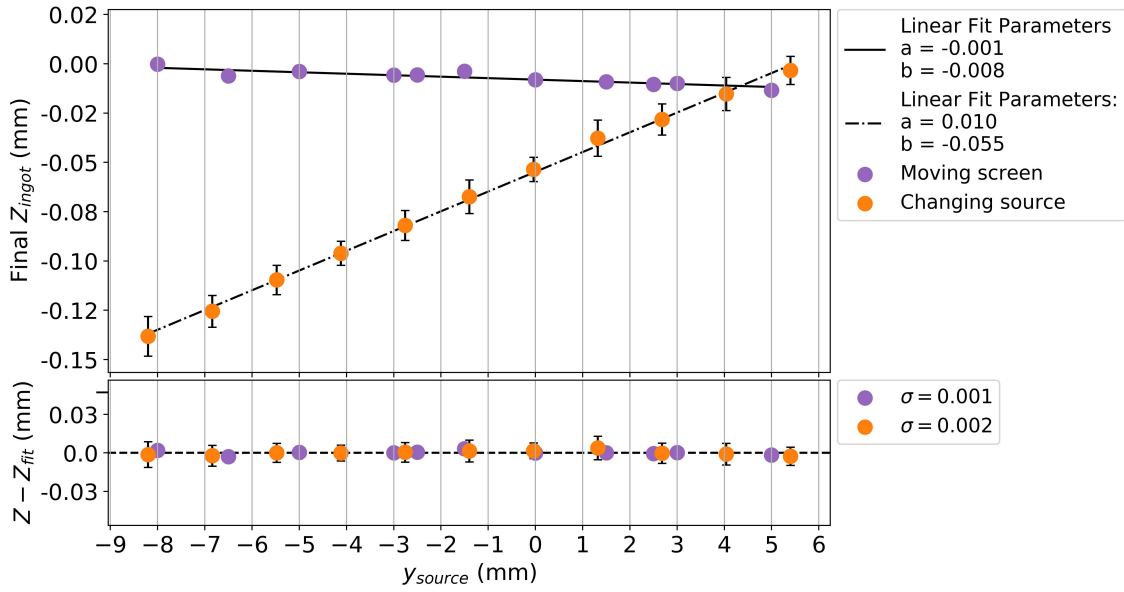


Figure 5.30: Results from two sets of alignments performed with "while" loop are plotted, for sources with different horizontal shifts. Horizontal shifts of the source, corresponding to a y_{source} , were achieved with movements the screen parallel to the optical axis (purple dots) or by illuminating different columns of the screen (orange dots), now kept fixed. The x-axis displays the y_{source} , in mm. The y-axis represents the final Z axis position of the ingot, in mm. **Top:** Linear fits performed to both sets of data, with best fit parameters $a = -0.001$ and $b = -0.008$ mm (moving screen) and $a = 0.010$ and $b = -0.055$ mm (changing source). **Bottom:** The residuals of the fits have a standard deviation of $\sigma = 0.001$ mm and $\sigma = 0.002$ mm, respectively.

The fitted linear function parameters and standard deviations of the residuals are displayed on the Table 5.4. The data fits are depicted in Figure 5.31. The parameter a is expected to be 1 for a optical layout with magnification 1:1 and notably it is $a = 0.932$ when the screen is moved and slightly smaller $a = 0.899$ when the source is changed.

Finally, regarding the x axis, we evaluated the linearity of the alignment by fitting linear functions to the final values of X for the moving screen data and the changing source data.

$$X_{ingot} = a \times y_{source} + b \quad (5.13)$$

The fitted linear function parameters and standard deviations of the residuals are displayed on the Table 5.4. The data fits are depicted in Figure 5.32. The parameter a is expected to be 0, as the x coordinate of the ingot should be independent of the horizontal movement of the source, unless the screen plane or linear stage holding the screen itself is tilted with respect to the optical axis. From the fits it was found to be $a = 0.015$ when the screen is moved and slightly smaller $a = 0.034$ when the source is changed. The first value corresponds to an inclination of the linear stage of the screen and the second to the inclination of the screen itself, on the linear stage. Both of them are very small and these linear fits can be used to correct for the positions obtained in future alignments.

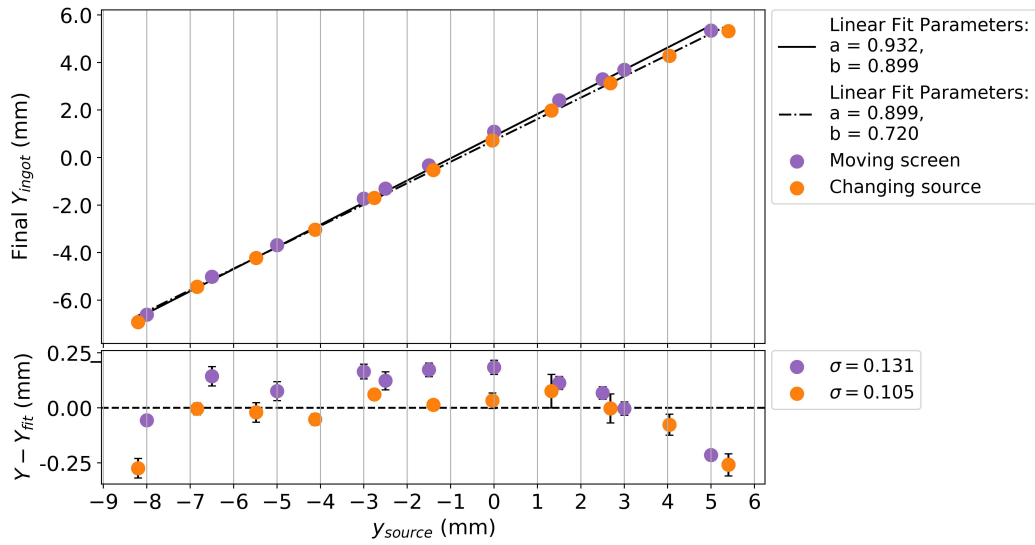


Figure 5.31: Results from two sets of alignments performed with "while" loop are plotted, for sources with different horizontal shifts. Horizontal shifts of the source, corresponding to a y_{source} , were achieved with movements the screen parallel to the optical axis (purple dots) or by illuminating different columns of the screen (orange dots), now kept fixed. The x-axis displays the y_{source} , in mm. The y-axis represents the final Y axis position of the ingot, in mm. **Top:** Linear fits performed to both sets of data, with best fit parameters $a = 0.932$ and $b = 0.899$ mm (moving screen) and $a = 0.899$ and $b = 0.720$ mm (changing source). **Bottom:** The residuals of the fits have a standard deviation of $\sigma = 0.131$ mm and $\sigma = 0.105$ mm, respectively.

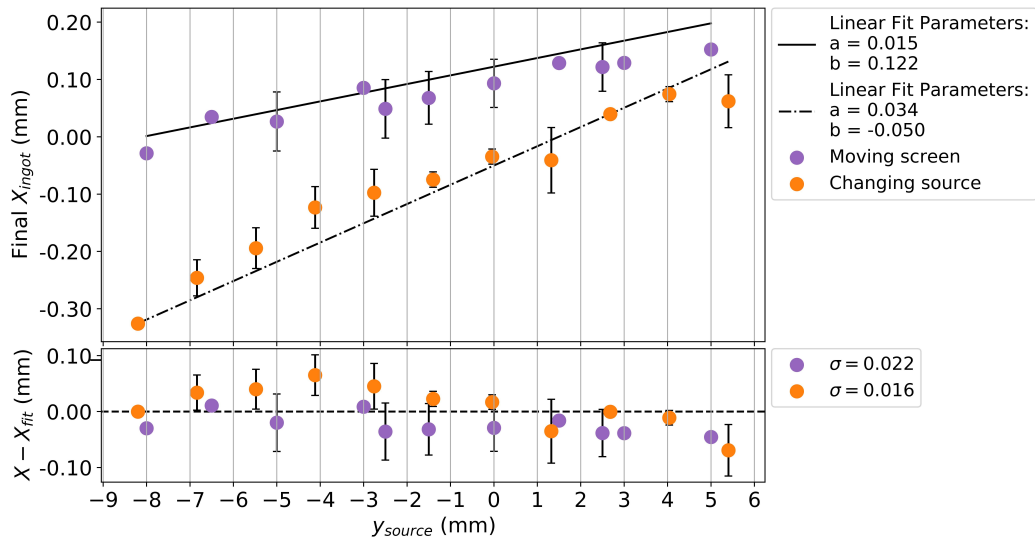


Figure 5.32: Results from two sets of alignments performed with "while" loop are plotted, for sources with different horizontal shifts. Horizontal shifts of the source, corresponding to a y_{source} , were achieved with movements the screen parallel to the optical axis (purple dots) or by illuminating different columns of the screen (orange dots), now kept fixed. The x-axis displays the y_{source} , in mm. The y-axis represents the final X axis position of the ingot, in mm. **Top:** Linear fits performed to both sets of data, with best fit parameters $a = 0.015$ and $b = 0.122$ mm (moving screen) and $a = 0.034$ and $b = -0.050$ mm (changing source). **Bottom:** The residuals of the fits have a standard deviation of $\sigma = 0.022$ mm and $\sigma = 0.016$ mm, respectively.

| | Vertical Movements z_{source} | | Horizontal Movements y_{source} | |
|-------------|---------------------------------|---------------------|-----------------------------------|---------------------|
| | Moving screen | Changing source | Moving screen | Changing source |
| | $a = 0.031$ | $a = 0.016$ | $a = 0.015$ | $a = 0.034$ |
| X_{ingot} | $b = -0.457$ mm | $b = -0.223$ mm | $b = -0.034$ mm | $b = -0.050$ mm |
| | $\sigma = 0.008$ mm | $\sigma = 0.033$ mm | $\sigma = 0.022$ mm | $\sigma = 0.016$ mm |
| | $a = 0.105$ mm ⁻¹ | - | $a = 0.932$ | $a = 0.899$ |
| Y_{ingot} | $b = -2.881$ | - | $b = 0.899$ mm | $b = 0.720$ mm |
| | $c = 20.955$ mm | - | - | - |
| | $\sigma = 0.019$ mm | - | $\sigma = 0.131$ mm | $\sigma = 0.105$ mm |
| | $a = -1.001$ | $a = -1.024$ | $a = -0.001$ | $a = 0.010$ |
| Z_{ingot} | $b = 13.762$ mm | $b = 14.184$ mm | $b = -0.008$ mm | $b = -0.055$ mm |
| | $\sigma = 0.024$ mm | $\sigma = 0.039$ mm | $\sigma = 0.001$ mm | $\sigma = 0.002$ mm |

Table 5.4: The best fit parameters resultant from the plots of Figures 5.27, 5.28, 5.29 (for vertical movements) and Figures 5.30, 5.31, 5.32 (for horizontal movements) are displayed.

From the values of the slopes of the linear fits, we can calculate the inclination of the screen and sources with respect to the optical axis by using $\theta = \arctan(a)$. Figure 5.33 should be consulted for a better illustration of the angles in question. The angles α, β, γ shown always refer to the inclination of the screen relative to the centre of the optical path but analogous angles α', β', γ' can be thought of related to the linear stage holding the screen in relation to the center of the optical path.

The values of these angles are $\alpha' = 1.77^\circ$ (linear stage) $\alpha = 0.92^\circ$ (screen), $\beta' = 0.86^\circ$ (linear stage), $\beta = 1.94^\circ$ (screen). Finally, the tilt of the plane of the screen that makes the different LGS not parallel to the optical axis is around $\gamma = 0.57^\circ$ while the horizontal stage holding the screen seems to only be tilted by $\gamma' = 0.06^\circ$.

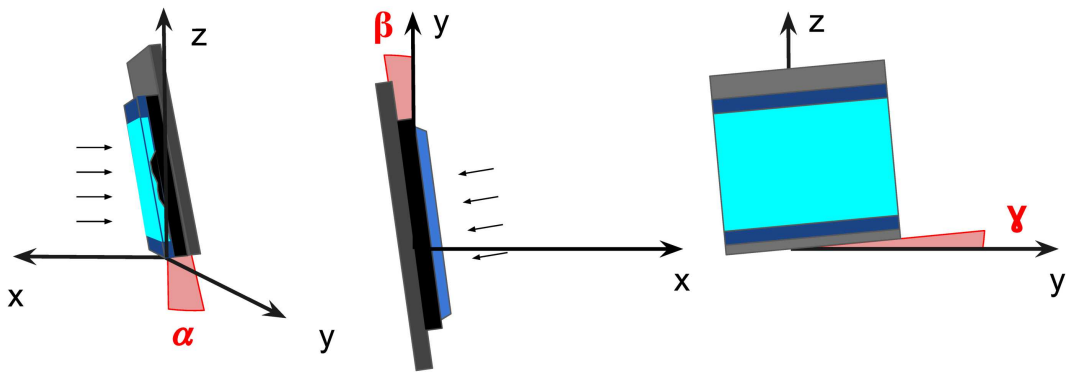


Figure 5.33: The inclination of the screen relative to the (X,Y,Z) reference system is illustrated. Black arrows indicate the front face of the OLED Screen. **Left:** Tilt of screen plane by $\alpha = 0.92^\circ$. **Middle:** Tilt of the screen plane by $\beta = 1.94^\circ$. **Right:** Tilt of the screen by $\gamma = 0.57^\circ$.

5.4 Quasi Closed-Loop Situation: Control Loop

As explained on Chapter 3, AO systems usually work on a closed-loop arrangement. The WFS measures residual aberrations of the incoming light, after passing through a DM which continuously receives commands from the RTC to adapt its shape and reduce the sensed aberrations. Up until this point on the laboratory experiments, we haven't dealt with aberrations correlated with Zernike polynomials and the alignment procedure mentioned until now is only a relative alignment of the I-WFS to the best focal plane of the optical system. We've characterised the movements of the ingot to reach the aligned position when the source's characteristics change, sequentially, *i.e.* one change of the source is followed by the command to start alignment.

We are now interested in developing a routine which automatically detects misalignments of the system and immediately proceeds to align it. In particular, the goal is to keep the I-WFS always aligned, as the source's characteristics change sporadically in time. Since closed-loop is scientifically not the correct definition of this, we created a routine that has been named Control Loop. Here are some of its functions:

- The alignment of the system is being controlled by continuously taking images (every 1.5 seconds) and checking if the pupils are aligned, *i.e.*, confirming whether the observables of the pupils in the most recent frame fall outside the alignment boundaries.
- The alignment procedure ("while" loop) is started if the system isn't aligned.
- On the contrary, if the system is aligned, we continue to monitor the observables every 1.5 seconds.
- In parallel, the source's characteristics are being changed at random times. The minimum time can be adjusted to increase the frequency of the changes.
- (As alternative to the above sentence) It is also possible to include a condition that only changes the source when the previous alignment is finished.

It is possible to monitor the alignment of the system by looking at the time evolution of each of the six observables. To highlight how misaligned the system is, it is more relevant to plot the relative difference of each observable from the target value: $O - O_{targetvalue}/\sigma$, where σ is the width of the alignment range of each observable. This quantity is therefore measured in units of σ . Each plot gathers a lot of information, which we deconstruct in Figure 5.34 in:

1. Black dots: control dots spaced by 1.5 seconds in between, informing about the aligned status of the observables. $|\sigma > 1|$ corresponds to misalignment.
2. Red crosses: the instants where the OLED Screen is changed. Accompanying the red crosses there is a label on the top of the graph with the sources characteristics: (VS,total thickness: $TU + TD + 1$,total length: $LL + LR + 1$,#D).
3. Colored dots: when the control loop signals the system as misaligned, the alignment procedure is activated. At the end of the alignment, the observables are recorded.

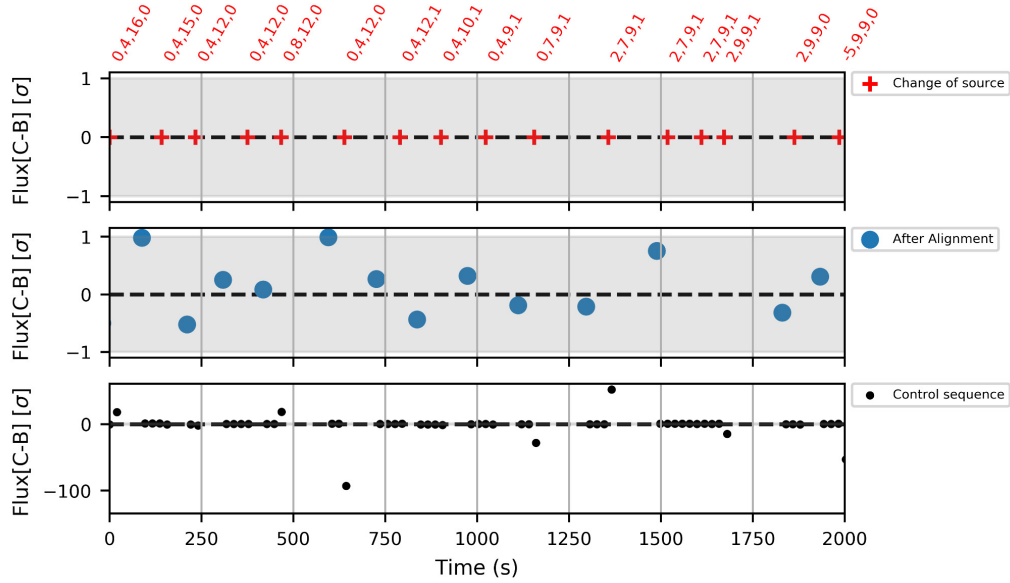


Figure 5.34: To monitor the alignment of the system, plots of the time evolution of each observable can be created. On the y-axis the values of the relative difference of each observable from the target value are shown: $O - O_{targetvalue}/\sigma$, where σ is the width of the alignment range. Here only the Flux $[C - B]$ is displayed as example. **Top:** Red crosses to mark the instants where the OLED Screen is changed, with respective LGS characteristics. **Middle:** Colored dots with the observables at the end of the alignment. **Bottom:** Black dots spaced by 1.5 seconds in between to control the alignment status.

All of this information can be put together in a single plot for each observable, as shown in Figure 5.35. The time evolution of the value of the observable can be followed and the alignment of the system can be controlled. However, the aligned range is sometimes not visible because the misaligned control dots fall very outside of it. If we look closer inside the aligned range, we can see better the stability of the alignment.

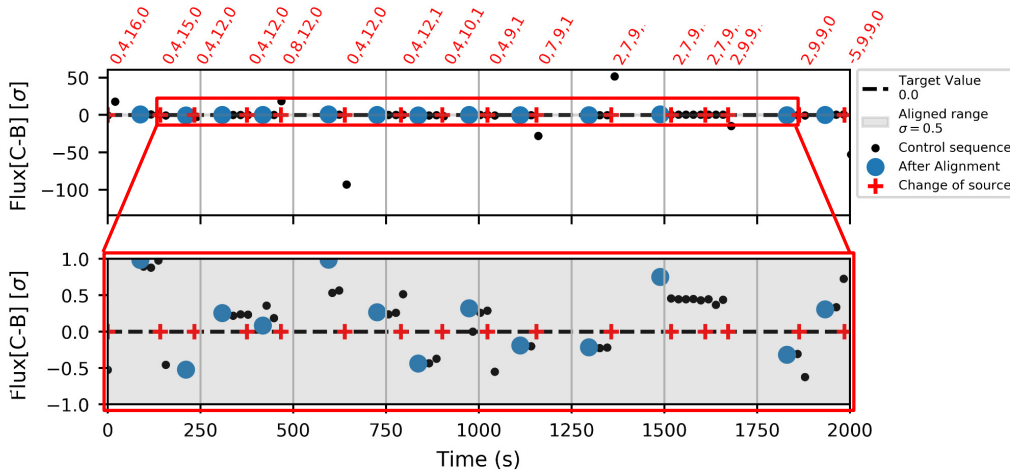


Figure 5.35: **Top:** All the data relative to the control of the alignment of the system, as a function of time, for Flux $[C - B](\sigma)$. $|\sigma| > 1$ corresponds to misalignment. **Bottom:** Y-axis restricted to the 1σ boundary, for better visualisation.

We have put this process to the test by applying in a random way the following variations of the source:

1. Shifts of the source perpendicular to the optical axis, using the **VS** parameter;
2. Shifts of the source parallel to the optical axis, using the **HS** parameter;
3. Changes of thickness of the source, using the **TU+TD** parameters;
4. Changes of length of the source, using the **LL+LR** parameters;
5. Introduction of discontinuities along the length of the source, using **#D** parameter.

In Figures 5.36,5.37 we represent one example of the control loop keeping the system aligned as the source is changed, in a total run time of 6000 seconds. The source was changed roughly every two minutes and after proceeding to align the ingot, the system was always found within the aligned position limits.

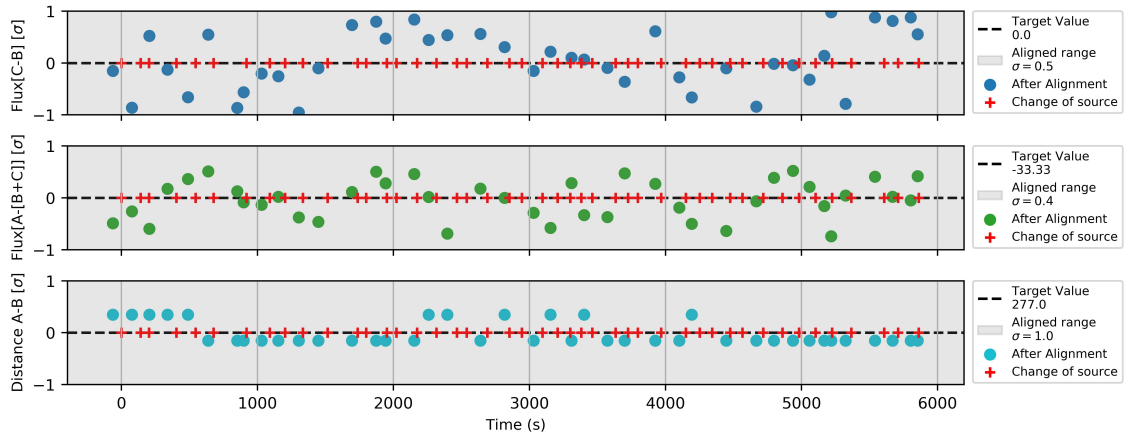


Figure 5.36: Control Loop example run, lasting for a total of 6000 seconds, as random variations of the source were introduced. Black dots and source labels were omitted. Here, the observables $\text{Flux}[C - B]$, $\text{Flux}[A - [B + C]]$ and $\text{Distance } A - B$ evolution is registered, measured in σ .

With this control method, we were able to test the stability of the alignment for sources with the following range of changes and their equivalent change on sky:

1. Vertical shift of ± 8 rows, corresponding to $\pm 3''$ on sky;
2. Maximum reduction of LGS extension of 69% with respect to the standard source;
3. Thickness reduction of 80% and increase of 120%, compared to the standard source;
4. Up to 4 discontinuities along the length of the LGS.

When exploring the limits of alignment, we came to the realisation that the hexapod has a very small dynamic range. As a consequence, before the ingot is able to reach an aligned position, most often the system reaches a position out of limits because of the previously mentioned overshoot. To explore the real limitations of the I-WFS, this behaviour needs to be corrected for.

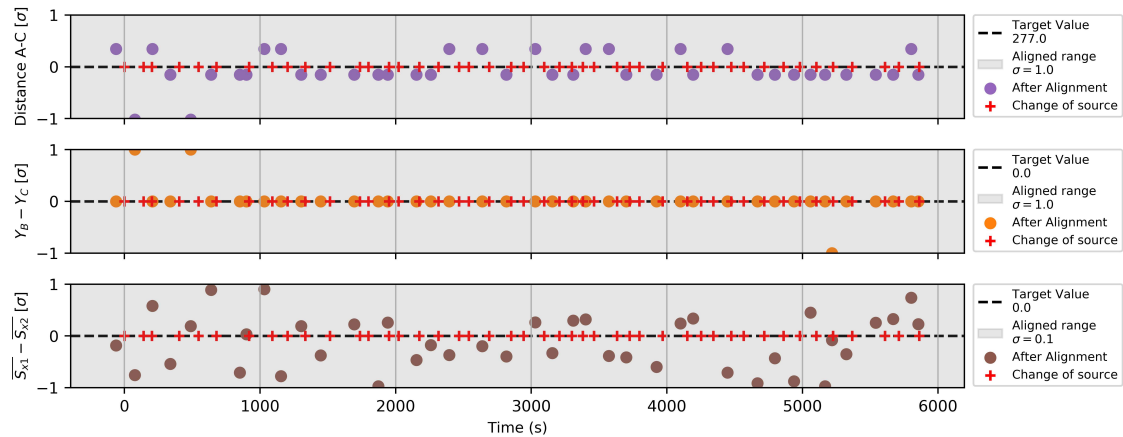


Figure 5.37: Control Loop example run, lasting for a total of 6000 seconds, as random variations of the source were introduced. Black dots and source labels were omitted. Here, the observables Distance A – C, $[Y_B - Y_C]$ and $\overline{S_{x1}} - \overline{S_{x2}}$ evolution is registered, measured in σ .

5.5 Search Algorithm

When the ingot experiences significant misalignment, it may lead to a situation where only one or two pupils become illuminated. A critical consideration is whether the ingot can recover from these scenarios, as they could realistically occur during telescope operations.

As of now, the answer remains negative. In either of these scenarios, the ingot’s sensitivity along the y-axis tends to cause predominant adjustments along that axis, often leading to overshooting and moving beyond permissible limits.

To address this challenge, our goal is to develop an algorithm that can effectively transition from a configuration with only one illuminated pupil to a state in which the system is capable of initiating the alignment process without going out of bounds.

This undertaking is part of a broader initiative to create a system capable of detecting light even in cases where the prism initially lacks any illumination. This process essentially involves a search procedure, which we term the search algorithm.

Beginning with an absence of illuminated pupils, the objective is to advance through a sequence: from 0 pupils to 1 pupil, then from 2 to 3 and ultimately to achieve a viable alignment setup.

To commence, it is essential to ascertain the physical limitations governing the hexapod’s movement:

- Along the x-axis: Movement is constrained within a range of 17 mm to -15 mm;
- Along the y-axis: Movement is restricted within the range of 5 mm to -6 mm;
- Along the z-axis: The allowable range is 18 mm to -12 mm;

The proposed strategy involves primarily restricting the initial movement to the x-z plane. This approach aims to direct light onto select reflective pupils. Subsequently, once an adequate amount of light is reflected, resulting in satisfactory counts on the B and C pupils, the system is then guided to introduce movement along the y-axis. This secondary movement serves the purpose of achieving a transmitted light ratio of 1/3.

5.5.1 First step: from Zero to One Illuminated Pupil

In cases where both the reflected and transmitted pupils lack any illumination, the ingot and the camera find themselves significantly distant from the LGS image. It becomes imperative to reposition them in a manner that enables the prism and camera to intersect at least a portion of the LGS image, until light appears on the transmitted pupil. This positioning can be achieved with adjustments confined to movement within the x-z plane, even before any light interacts with the prism.

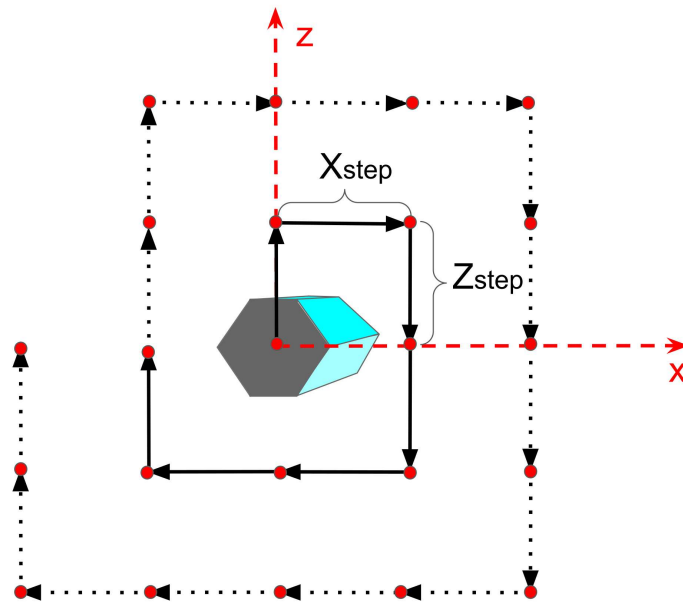


Figure 5.38: The search algorithm scan follows a specific direction on the x-z plane, taking steps of size X_{step} and Z_{step} . The light intensity of the pupils at each location is recorded. At each level of the scan, the systems looks to maximise the search criterion. If on the first level (continuous arrows) no maximum is found, it moves on to the second level expanding the search radius (dotted arrows), and so on.

Starting from the existing configuration, a systematic scan of the surrounding area is initiated. In essence, both the ingot and the camera maneuver around the initial position while recording the light intensity of the pupils at each location. The direction of this movement is exemplified in Figure 5.38. The incremental movement step should be smaller than the size of the prism to ensure that the optimal focus is not missed. The dimensions of the search area progressively expand until any positive change in the flux of the pupil A becomes discernible. At this point, the search shifts to the new position where the flux in pupil A was maximized, and the process is repeated. Throughout this exploration, the ingot consistently moves in the direction that maximizes the absolute flux in pupil A. This iterative procedure concludes once a local maximum is identified. This particular configuration marks the point at which the LGS image is entirely transmitted without undergoing reflection.

As of the present moment, practical testing of this algorithmic phase is unfeasible. Achieving the condition of having no light on the pupils would necessitate moving the screen or camera away from the optical path, which is not currently viable.

Despite this limitation, the search algorithm effectively operates, granting users the flexibility to select various criteria/observables to maximize, along with the corresponding step size.

5.5.2 Second step: from One to Three Illuminated Pupils

Upon achieving complete light transmission, the movement within the x-z plane should persist until adequate light is reflected from the ingot prism. The search algorithm follows the same principle of maximizing a measurable quantity until a local maximum/mimimum is identified. However, during the process of selecting the quantity to maximize, we encountered a wide array of local maxima from different measurements. No single observable emerged as a clear indicator that would consistently guide us toward the aligned position.

An illustrative contour plot, shown in Figure 5.39, depicts the initial exploration of the entire x-z plane within a region of -5 mm to 5 mm, centered at zero. The values of the total counts in pupils A, B and C, their sum $A+B+C$, the sum of the counts in the reflected pupils $B+C$ and the absolute value of $B - C/(A + BpC)$ were recovered with a spatial resolution of 0.1 mm. This exploration revealed distinct regions:

1. Negative x values and the entire z range from -5mm to 5mm correspond to configurations where only the transmitted pupil is illuminated.
2. Values close to the origin and below, ie, $x \approx 0$ and $z < 0$ correspond to light mostly on pupil B, increasing as z decreases. Beyond a certain z value, light once again bypasses the prism, resulting in complete transmission.
3. Symmetrical behavior unfolds for positive z values, corresponding to light on the C pupil.
4. Higher x values and the complete z range exhibited irregular values that defied straightforward explanation.

Notably, examining the total counts in pupils $A + B + C$ revealed a region where the counts were not constant, contrary to expectations. Additionally, the normalized difference $B - C$ exhibited unexpected behavior in the last region, with isolated peaks and valleys.

The irregular behavior observed for specific values of x and z stemmed from the infrastructure supporting the ingot, intermittently obstructing the light path, as illustrated in Figure 5.40 (a). To address this, we opted to shield that problematic region with tape, as displayed in (b). However, this mitigation didn't entirely eliminate the anomalous signals in pupils B and C. Subsequently, we recognized that some light was reflecting off the small faces of the hexagonal pipe, introducing unexpected reflected light when complete transmission was anticipated (c). Consequently, we chose to completely obstruct light from reaching those two faces by covering them as shown in (d).

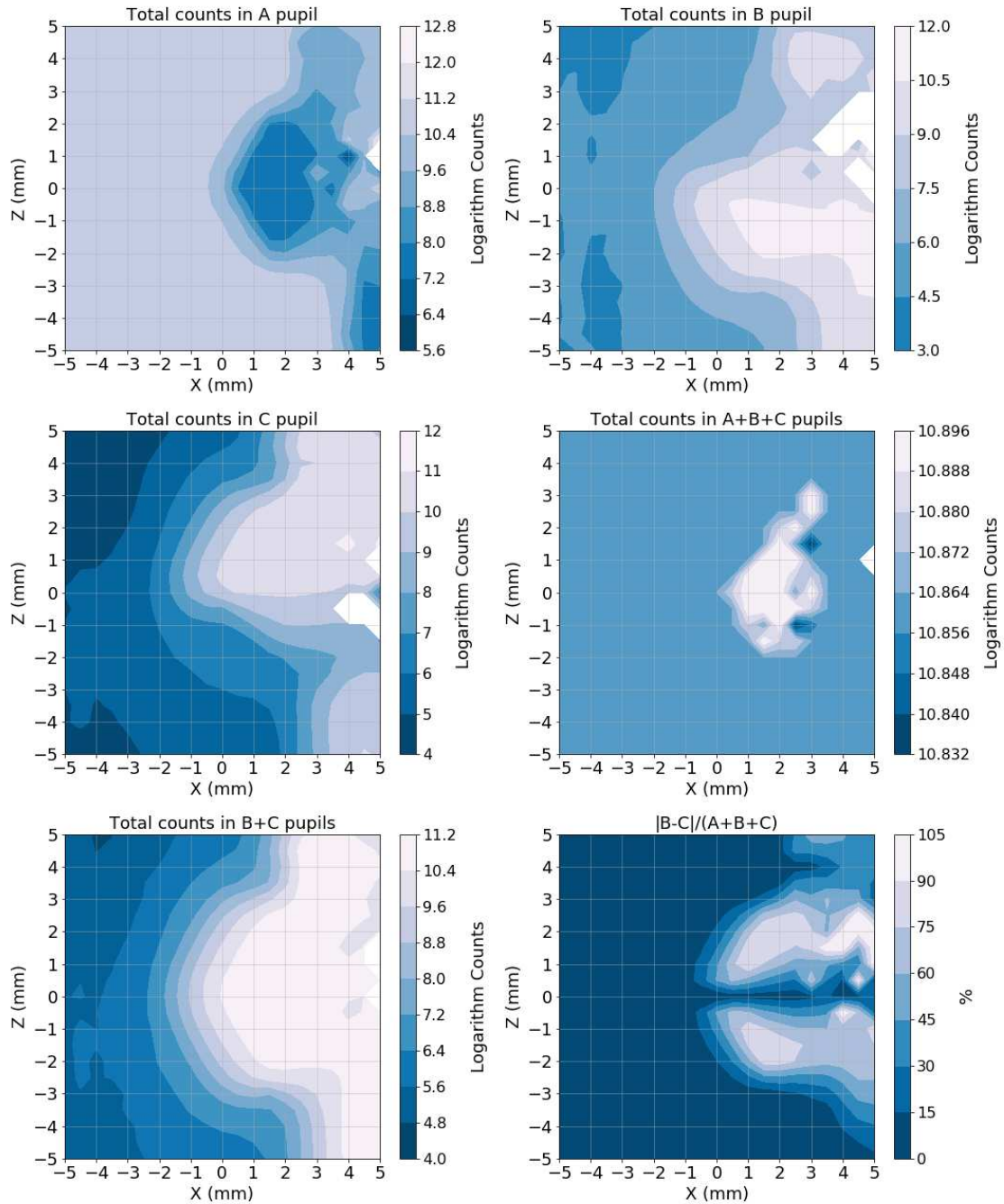


Figure 5.39: Contour plots show the scan performed on the x-z plane, with a resolution of 0.1 mm, revealing the logarithmic counts of the following quantities: **Top Left:** Total counts on pupil A; **Top Right:** Total counts on pupil B; **Middle Left:** Total counts on pupil C; **Middle Right:** Total counts on the three pupils A+B+C; **Bottom Left:** Total counts on the reflected pupils B+C; **Bottom Right:** Absolute value of the normalised flux difference between reflected pupils $|B - C|/(A + B + C)$.

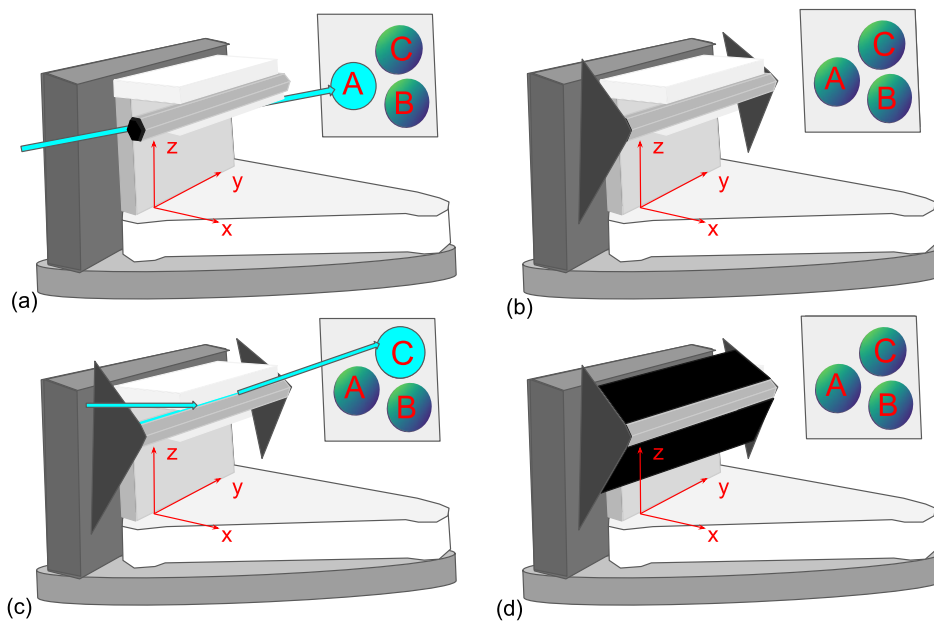


Figure 5.40: **(a)** The structure holding the ingot prism was vignetting the image at certain positions, revealing unexpected secondary maxima of the flux in pupil A; **(b)** The space between the ingot and the structure was covered with tape to remove the irregular vignetting, blocking light from passing in between; **(c)** The top and bottom surfaces of the ingot prism have a reflective nature that is not predicted on the ingot design. Hence, unexpected flux on the reflected pupils B and C was giving rise to secondary maxima on the B+C counts at certain positions; **(d)** The ingot's top and bottom faces were covered with tape, leaving only the two side faces uncovered.

After revisiting the x-z plane scan with the modifications in place, the behavior aligned with expectations. The new contour plots are presented in Figure 5.41. The four regions persisted as follows:

1. Negative x values and the entire z range from -5 mm to 5 mm correspond to configurations where only the transmitted pupil is illuminated.
2. Values $x > 0$ and $z < 0$ correspond to light mostly on pupil B, increasing as z decreases. Beyond a certain z value, light once again bypasses the prism, resulting in an increase in reflected light.
3. Symmetrical behavior unfolds for positive z values, corresponding to light on the C pupil.
4. Visible on the $|B - C|$ plot, $x > 0$ and $z = 0$ corresponds to a region where B and C are equally illuminated and still some light is transmitted to pupil C.

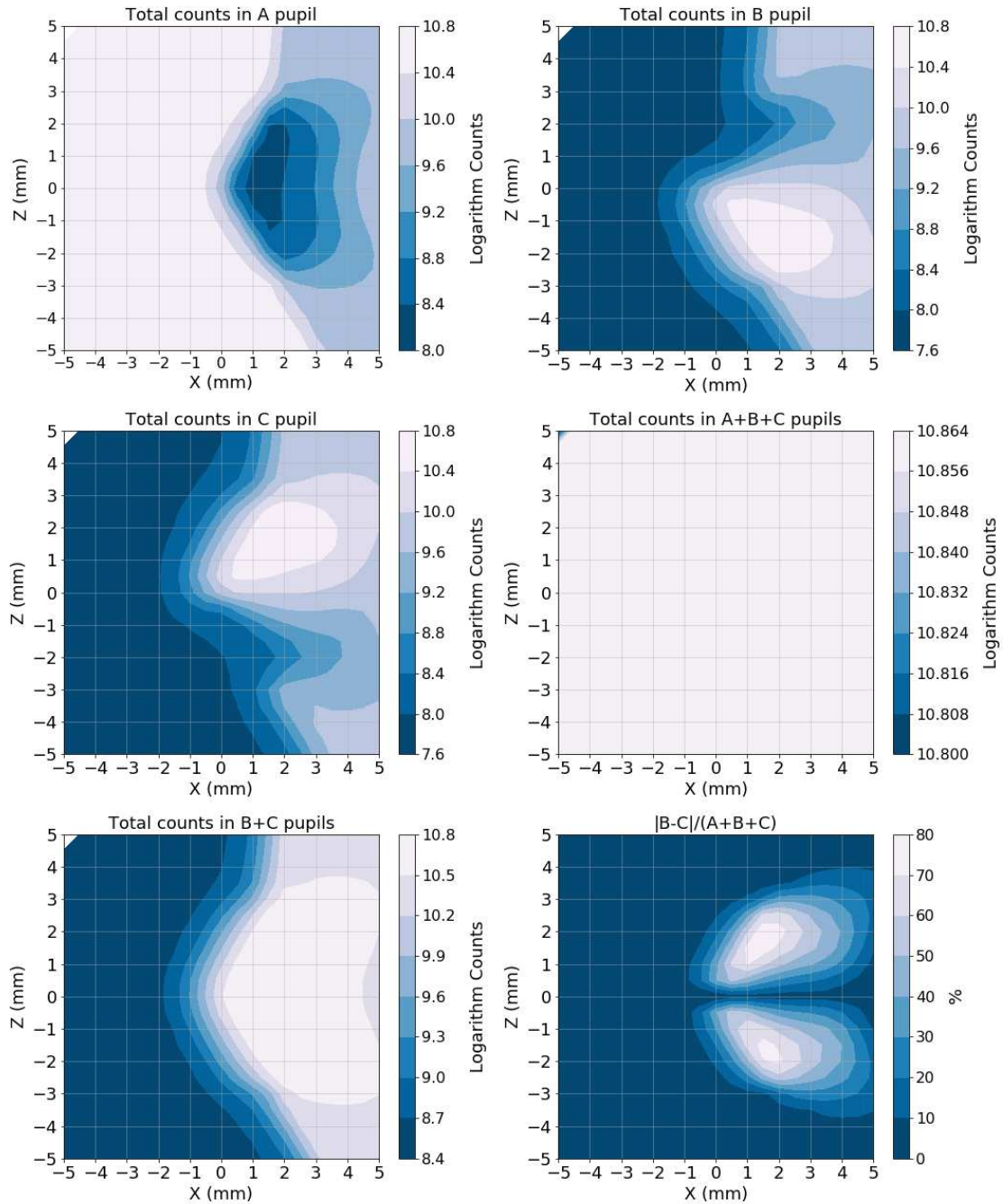


Figure 5.41: Contour plots show the scan performed on the x-z plane, with a resolution of 0.1 mm, revealing the logarithmic counts of the following quantities: **Top Left:** Total counts on pupil A; **Top Right:** Total counts on pupil B; **Middle Left:** Total counts on pupil C; **Middle Right:** Total counts on the three pupils A+B+C; **Bottom Left:** Total counts on the reflected pupils B+C; **Bottom Right:** Absolute value of the normalised flux difference between reflected pupils $|B - C|/(A + B + C)$.

This data is instrumental in selecting a measurement that can guide the system to a region from which the alignment procedure can smoothly resume, without encountering conflicts. To aid in this determination, we superimposed the range of positions where successful alignment occurs, using the standard source, over the values of pupil A and the absolute value of $|B - C|$, as showcased in Figure 5.42.

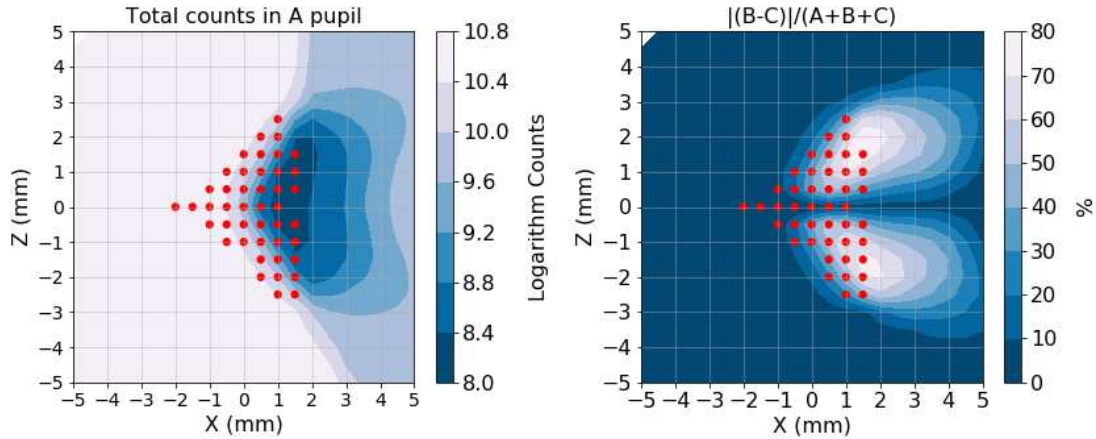


Figure 5.42: Scan of the x-z plane showing the counts in pupil A and the values of $|B - C|/(A + B + C)$. Due to the hexapod's limited range of motion and the observable's degeneracy (mainly the Y overshoot), the alignment of the I-WFS can only be successful if it starts on the area covered with red dots.

Two potential strategies await testing:

1. Minimizing the counts in pupil A to reach the absolute minimum region.
2. Maximizing the value of $|B - C|/(A + B + C)$ to reach one of the two local maxima.

Though untested, these possibilities are viable candidates for advancing the system. The same routine employed earlier is anticipated to be effective in these cases.

5.5.3 Insights for Prototyping

We conclude this section by highlighting the significance of the ingot prism's shape. Several modifications were necessary for the current prototype, largely due to its hexagonal prism composition, featuring two fully exposed reflecting faces and two partially exposed ones. A future prototype crafted from a pyramidal prism should alleviate this concern. However, these tests underscore the importance of ensuring that only two surfaces contribute to reflection, while guaranteeing the obstruction-free configuration of the prism-holding infrastructure. While some degree of vignetting due to the infrastructure might persist, it should be well understood and managed.

5.6 New OLED Screen

The currently employed screen, as detailed in Section 5.2, lacks the capability to adjust the brightness of individual pixels. This functionality, however, is of significant interest for our purposes, as it would enable the simulation of the LGS's profile along its extent. The LGS

beacon's luminosity is not uniform due to the varying density of sodium atoms at different altitudes. This variability is both spatial, corresponding to the LGS's spatial distribution, and temporal, as the LGS intensity changes over time. To comprehend the implications of these fluctuations on the stability of the I-WFS alignment, we are motivated to devise a method for simulating the LGS profile on a screen.

We have identified an OLED screen with capabilities similar to the one currently in use. Unlike the existing monochrome screen, this version features a 16-level greyscale. This means that each pixel on the OLED screen can be assigned a distinct greyscale or brightness value within a range of 0 to 16. The specific model we are considering is the 1.5-inch OLED SSD1327 Module with 16-bit greyscale, boasting a resolution of 128×128 pixels. Each pixel occupies dimensions of 0.19×0.19 mm and is separated by 0.21 mm from its neighboring pixels.

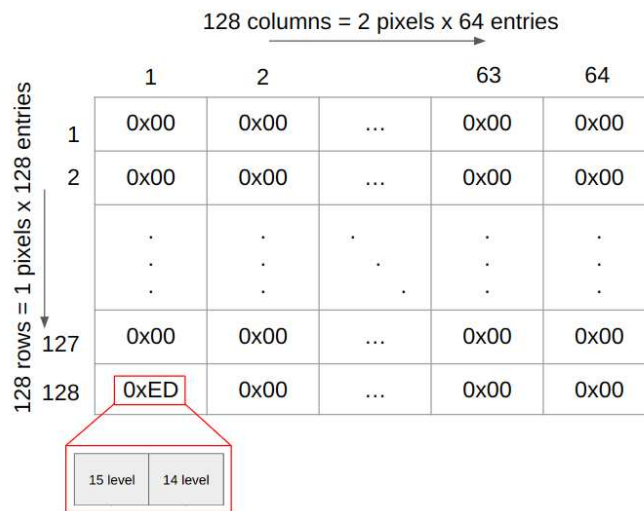


Figure 5.43: Schematic representation of the SSD1327 bitmap. It is a matrix of 64×128 entries, to illuminate the 128×128 pixels of the screen. Each entry consists of an hexadecimal number that controls the brightness level (0 – 16) of each pair of adjacent pixels.

Regarding this screen's bitmap, it consists of a matrix of 64×128 entries/bytes that are written in hexadecimal format, as illustrated in Figure 5.43. Each byte corresponds to 2 adjacent pixels. Hence, instead of 128 entries corresponding to the 128 columns, there are 64 entries, one for each pair of pixels in a row of the screen. To set the brightness of each pixel, a level of grey between 0 and 16 must be chosen, and that integer must be converted to hexadecimal value. An example of this conversion is shown in Figure 5.44.

Using this advanced screen, our future work involves replicating sodium layer profiles. This includes following authentic profiles obtained at the 6 metre Large Zenith Telescope in Canada [92]. Using LIDAR technology (Laser Imaging Detection and Ranging), information regarding the sodium density at different altitudes can be obtained [93]. This method consists in measuring the time between the emission of laser pulses tuned to excite the sodium atoms and the detection of the backscattered signals, which will provide insight into the altitude and density of the impacted atoms. With the high resolution LIDAR system installed at the Large Zenith Telescope, several sodium profiles were obtained after careful data treatment and analysis.

The data set comprises a total of 16 cases, obtained throughout the month of July

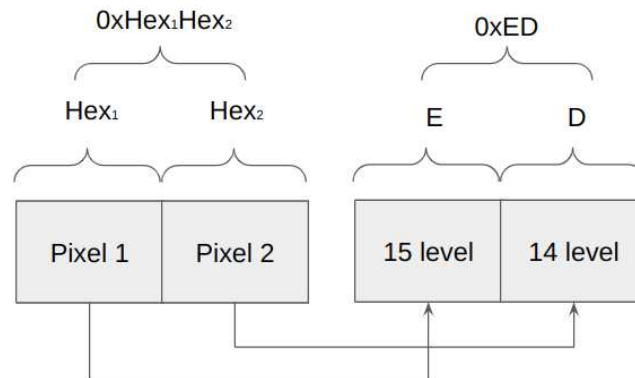


Figure 5.44: Each entry of the screen's bitmap is a hexadecimal number that controls the brightness level of each pair of adjacent pixels. To choose the brightness of each pair, a hexadecimal value equivalent to the two grey scale levels is written on the bitmap, as illustrated here. The example of two pixels with 15 and 14 grey scale level results in the entry $0xED$.

2010, with each case consisting of 30 profiles. These profiles result from 10-second time integrations and offer a vertical resolution of 126.5 metres. The data set encompasses 198 height levels, starting from the lowest altitude bin of 80 km. In the Appendix A, we include samples from three distinct cases, each drawn from separate nights, with three profiles superimposed for ease of reference.

To commence the process of replicating these profiles on the OLED screen, we will need to map the 198 height levels onto the screen's 128 pixels. This transformation inevitably leads to some loss of resolution. Alternatively, an approach involving the arrangement of two screens side by side could potentially yield a total extension of 256 pixels. Furthermore, considering that the counts per bin reach a maximum value of 6000, it will be necessary to convert these counts into the 16-level greyscale. This discretization further downscales the resolution of the LGS profile replication across the screen.

5.7 Future Work

The research described so far has provided valuable insights into the alignment and simulation of this LGS and I-WFS system, shedding light on various aspects of the setup's performance and limitations. Just like any scientific pursuit, there are many paths to explore and improve upon in pushing this experiment forward. This chapter discusses potential routes for future research.

Enhancing Experimental Setup

To ensure the precision and reliability of the experimental setup, it is imperative to address existing technical challenges and shortcomings. The immediate task at hand involves rectifying the issues observed with the current setup, such as the screen anomalies and ingot prism holding structure effects, to which temporary fixes have been applied. This could entail replacing the problematic screen with a more suitable alternative (the new OLED screen) and designing a custom 3D-printed capsule for the ingot prism.

Systematic Analysis of Alignment

A deeper investigation into systematic mistakes during alignment procedures is needed. Focusing on specific movements that weren't so deeply explored yet, it is possible to uncover patterns that may have been overlooked. By meticulously analyzing alignment data, it becomes feasible to pinpoint recurring errors and devise strategies to mitigate them.

Accurate Replication of Source Size Ratios

Recently, we found out that the size ratio of our LGS in the set up wasn't replicating the real size of the LGS relative to the ELT aperture. To do that, we would need a much longer OLED screen, or more than one placed side by side. By comprehensively understanding the size ratios of LGS and devising strategies to replicate them faithfully in our setup, we can better simulate real-world conditions. This adjustment is vital for achieving results that accurately reflect the behavior of LGS under various scenarios, contributing to a more comprehensive understanding of their performance in AO systems.

Application of Search Algorithm

With a well-developed search algorithm in place, our immediate focus shifts to determining the most suitable alignment criteria for efficient movement towards the aligned position. By defining this criteria among the two current possibilities, we can perform random misalignments and put the method to the test to assess its efficiency.

Real-time Sodium Profile Simulation

Integrating the OLED screen and sodium profile simulation into real-time experiments is a significant step toward replicating a real AO system. By converting sodium profiles into the greyscale format compatible with the OLED screen, we can dynamically replicate real-world scenarios and study the resulting effects on alignment stability.

Integration of Deformable Lens (DL)

The incorporation of a DL into the setup presents a valuable opportunity to explore controlled aberrations. This device, with its ability to apply low-order known aberration terms, offers new insights into the system's response to controlled distortions. Characterizing the sensitivity and linearity of the system under known aberrations can provide valuable information for further refining alignment procedures and enhancing the overall robustness of the system.

Continued Evolution of the Setup

The proposed future evolution of the setup involves integrating additional components such as DMs, P-WFS, and SH-WFS. By conducting rigorous comparisons between different WFS options, we can gain a comprehensive understanding of their respective strengths and limitations in real-world applications.

On-Sky Testing

In the long run, we plan to bring the I-WFS to other testing facilities such as the ESO Wendelstein Laser Guide Star Unit (WLGSU), which is providing the artificial stars to the AO module installed at the William Herschel Telescope, and hence being able do on-sky testing of this wavefront sensor.

Chapter 6

Conclusions

Over the past six months, our dedicated efforts have been centered on characterising and advancing the Ingot Wavefront Sensor concept originally envisioned by Ragazzoni [20] and further refined by the AO Group at the INAF-Osservatorio Astronomico di Padova. This innovative sensor design, rooted in the Scheimpflug principle, holds the potential to address long-standing challenges inherent to LGS in classical WFSs, such as the SH-WFS and P-WFS.

At the core of the I-WFS lies the Scheimpflug principle. The image of the LGS created by the LLT, that is extended on a plane in the sky, has a conjugate optimal focal plane. Here, a sensor can be placed such as to sense the full 3D focal volume of the LGS. This approach aims to alleviate persistent issues associated with existing WFSs, including image defocus and LGS elongation on different subapertures, thereby unlocking the full potential of LGS in AO systems.

The sensor architecture, comprised of a prism with reflective surfaces creating two reflective pupils and a transmitted pupil, has been meticulously tailored to align with the specifications of the E-ELT. Great attention has been paid to the precise positioning of the LLT, telescope entrance pupil dimensions, and aspect ratio of the LGS image.

My involvement in this project has encompassed practical work in a laboratory setting, where a test bench is assembled and designed to replicate the conditions of the E-ELT. Within this controlled environment, we have refined and perfected essential procedures associated with the I-WFS.

We have successfully implemented an efficient and versatile algorithm for manipulating the LGS source on a screen. This capability enables us to accurately simulate several source variations, including changes in thickness, length, and on-sky movement.

The transition from a "for" loop to a "while" loop in the alignment procedure has yielded substantial benefits. It has led to a significant reduction in random fluctuations and improved overall efficiency. This adjustment has optimised the number of iterations required to achieve alignment.

Using several tests, we have rectified and corrected limitations within the test bench elements, particularly addressing the issue of an uneven side profile on the screen. Furthermore, we have identified and quantified systematic errors stemming from screen tilts and field curvature.

We have developed a quasi-closed loop algorithm, called control loop, that autonomously monitors and realigns the I-WFS. This algorithm has proven highly effective in maintaining alignment, in the presence of the following sporadic and random LGS changes: vertical shifts

of ± 8 rows, corresponding to $\pm 3''$ on the sky; maximum reduction of LGS extension by 69% compared to a standard source; reduction of the thickness by 80% and increase by 120% compared to a standard source; adding up to 4 discontinuities along the length of the LGS.

In addition to these accomplishments, the ongoing development of a search algorithm represents another crucial point of our work. This algorithm is designed to locate the image focus and achieve alignment, even from highly misaligned configurations. Testing for this search algorithm is a priority in our ongoing research.

Finally, with the choice and acquisition of a new OLED screen, we have taken a significant step forward by enabling the possibility of implementing real sodium profiles into our simulated LGS. This advancement brings us closer to replicating real-world conditions in our testing environment.

As we continue to explore, innovate and refine this WFS, following the future steps described in Section 5.7, we keep as ultimate goal obtaining an accurate description of the I-WFS performance and its comparison with other classical wavefront sensors. Depending on the results of that complete study, this sensor could be the key to achieving the full potential of LGS AO systems on the ELTs that are expected in the next decades.

Bibliography

- [1] R. R. Parenti, *Lincoln Laboratory Journal* **5**, 93 (1992).
- [2] J. W. Hardy, *Adaptive Optics for Astronomical Telescopes* (1998).
- [3] S. E. Egner, *Multi-conjugate adaptive optics for LINC-NIRVANA : Laboratory tests of a ground-layer adaptive optics system and vertical turbulence measurements at Mt. Graham*, Ph.D. thesis, Ruprecht-Karls University of Heidelberg, Germany (2006).
- [4] M. Bergomi, *Pyramid Wavefront Sensors for Astronomy and for the Human Eye*, [Ph.D. thesis](#), Padova, Italy (2013).
- [5] V. Viotto (Universita degli Studi di Padova, Padova, Italy, 2012).
- [6] S. Di Filippo, *The Ingot Wavefront Sensor: Dealing with extended sources in Astronomy*, [Ph.D. thesis](#), Padova, Italy (2022).
- [7] M. Lombini, L. Schreiber, E. Diolaiti, and F. Cortecchia, *mnras* **510**, 3876 (2022).
- [8] E. Portaluri, V. Viotto, R. Ragazzoni, C. Arcidiacono, D. Greggio, K. K. Radhakrishnan Santhakumari, M. Bergomi, S. Di Filippo, J. Farinato, and D. Magrin, in *Society of Photo-Optical Instrumentation Engineers (SPIE) Conference Series*, Society of Photo-Optical Instrumentation Engineers (SPIE) Conference Series, Vol. 11448 (2020) p. 114483I.
- [9] C. Mancini, N. M. F. Schreiber, A. Renzini, G. Cresci, E. K. S. Hicks, Y. Peng, D. Vergani, S. Lilly, M. Carollo, L. Pozzetti, G. Zamorani, E. Daddi, R. Genzel, C. Maraston, H. J. McCracken, L. Tacconi, N. Bouché, R. Davies, P. Oesch, K. Shapiro, V. Mainieri, D. Lutz, M. Mignoli, and A. Sternberg, *The Astrophysical Journal* **743**, 86 (2011).
- [10] N. M. F. Schreiber, A. Renzini, C. Mancini, R. Genzel, N. Bouché, G. Cresci, E. K. S. Hicks, S. J. Lilly, Y. Peng, A. Burkert, C. M. Carollo, A. Cimatti, E. Daddi, R. I. Davies, S. Genel, J. D. Kurk, P. Lang, D. Lutz, V. Mainieri, H. J. McCracken, M. Mignoli, T. Naab, P. Oesch, L. Pozzetti, M. Scodreggio, K. S. Griffin, A. E. Shapley, A. Sternberg, S. Tacchella, L. J. Tacconi, S. Wuyts, and G. Zamorani, *The Astrophysical Journal Supplement Series* **238**, 21 (2018).
- [11] S. Zieleniewski, N. Thatte, S. Kendrew, R. C. W. Houghton, A. M. Swinbank, M. Tecza, F. Clarke, and T. Fusco, *453*, 3754 (2015), [arXiv:1508.04441 \[astro-ph.IM\]](#) .

- [12] A. Vayner, N. L. Zakamska, Y. Ishikawa, S. Sankar, D. Wylezalek, D. S. N. Rupke, S. Veilleux, C. Bertemes, J. K. Barrera-Ballesteros, H.-W. Chen, N. Diachenko, A. D. Goulding, J. E. Greene, K. N. Hainline, F. Hamann, T. Heckman, S. D. Johnson, H. X. G. Lim, W. Liu, D. Lutz, N. Lutzgendorf, V. Mainieri, R. McCrory, G. Murphree, N. P. H. Nesvadba, P. Ogle, E. Sturm, and L. Whitesell, *arXiv e-prints*, [arXiv:2303.06970](https://arxiv.org/abs/2303.06970) (2023), [arXiv:2303.06970 \[astro-ph.GA\]](https://arxiv.org/abs/2303.06970) .
- [13] K. K. Radhakrishnan Santhakumari, D. Greggio, M. Bergomi, S. Di Filippo, V. Viotto, E. Portaluri, C. Arcidiacono, M. Dima, L. Lessio, L. Marafatto, T. Furieri, S. Bonora, and R. Ragazzoni, in *Society of Photo-Optical Instrumentation Engineers (SPIE) Conference Series*, Society of Photo-Optical Instrumentation Engineers (SPIE) Conference Series, Vol. 11448 (2020) p. 1144860.
- [14] J. Kepler, G. Galilei, and J. Pena, *Ioannis Kepleri ... Dioptrice seu Demonstratio eorum quae visui : praemissae epistolae Galilaei de iis, quae post editionem nuncii & visibilibus propter conspicienda non ita pridem inventa accidunt siderii ope perspicilli, nova & admiranda in coelo deprehensa sunt; item examen praefationis Ioannis Penae ... in optica Euclidis, de usu optices in philosophia* (1611).
- [15] I. Newton, *Opticks: or, A Treatise of the Reflexions, Refractions, Inflexions and Colours of Light* (William Innys, London, 1704).
- [16] G. E. Hale, *pasp* **27**, 235 (1915).
- [17] G. E. Hale, W. S. Adams, and F. H. Seahes, *Mount Wilson Observatory Annual Report* **5**, 127 (1933).
- [18] H. W. Babcock, *Publications of the Astronomical Society of the Pacific* **65**, 229 (1953).
- [19] V. P. Linnik, in *European Southern Observatory Conference and Workshop Proceedings*, European Southern Observatory Conference and Workshop Proceedings, Vol. 48 (1994) p. 535.
- [20] R. Ragazzoni, E. Portaluri, V. Viotto, M. Dima, M. Bergomi, F. Biondi, J. Farinato, E. Carolo, S. Chinellato, D. Greggio, M. Gullieuszik, D. Magrin, L. Marafatto, and D. Vassallo, *arXiv e-prints*, [arXiv:1808.03685](https://arxiv.org/abs/1808.03685) (2018), [arXiv:1808.03685 \[astro-ph.IM\]](https://arxiv.org/abs/1808.03685) .
- [21] J. Herschel, *Treatises on Physical Astronomy, Light and Sound Contributed to the Encyclopaedia Metropolitana* (R. Griffin, 1899).
- [22] G. B. Airy, *Transactions of the Cambridge Philosophical Society* **5**, 283 (1835).
- [23] H. Kragh, *Substantia* **2**, 7–18 (2018).
- [24] E. K. Smith and S. Weintraub, *Proceedings of the IRE* **41**, 1035 (1953).
- [25] O. Reynolds, *Philosophical Transactions of the Royal Society of London* **174**, 935 (1883), <https://royalsocietypublishing.org/doi/pdf/10.1098/rstl.1883.0029> .
- [26] L. Andrews, *Field Guide to Atmospheric Optics*, Field Guides (SPIE Press, 2019).

BIBLIOGRAPHY

- [27] J. Jiménez, *Arbor : Ciencia, Pensamiento y Cultura* **178** (2004), [10.3989/arbor.2004.i704.550](https://doi.org/10.3989/arbor.2004.i704.550).
- [28] A. Kolmogorov, *Akademiia Nauk SSSR Doklady* **30**, 301 (1941).
- [29] A. N. Kolmogorov, *Akademiia Nauk SSSR Doklady* **32**, 16 (1941).
- [30] A. N. Kolmogorov, *Journal of Fluid Mechanics* **13**, 82 (1962).
- [31] V. I. Tatarski, R. A. Silverman, and N. Chako, *Physics Today* **14**, 46 (1961).
- [32] *Adaptive Optics in Astronomy* (Cambridge University Press, 1999).
- [33] D. L. Fried, *J. Opt. Soc. Am.* **55**, 1427 (1965).
- [34] D. P. Greenwood and D. L. Fried, *J. Opt. Soc. Am.* **66**, 193 (1976).
- [35] R. Racine and B. L. Ellerbroek, in *Adaptive Optical Systems and Applications*, Vol. 2534, edited by R. K. Tyson and R. Q. Fugate, International Society for Optics and Photonics (SPIE, 1995) pp. 248 – 257.
- [36] K. Strehl, *Astronomische Nachrichten* **158**, 89 (1902).
- [37] J. W. Hardy, J. E. Lefebvre, and C. L. Koliopoulos, *J. Opt. Soc. Am.* **67**, 360 (1977).
- [38] B. Platt and R. V. Shack, *Journal of refractive surgery* **17 5**, S573 (2001).
- [39] R. Ragazzoni, *Journal of Modern Optics* **43**, 289 (1996).
- [40] R. J. Noll, *J. Opt. Soc. Am.* **66**, 207 (1976).
- [41] W. Southwell, *J. Opt. Soc. Am.* **70**, 998 (1980).
- [42] R. Tyson, *Principles of Adaptive Optics* (Academic Press, 1998).
- [43] J. M. Beckers, *Annual Review of Astronomy and Astrophysics* **31**, 13 (1993), <https://doi.org/10.1146/annurev.aa.31.090193.000305> .
- [44] D. L. Fried, *J. Opt. Soc. Am.* **72**, 52 (1982).
- [45] F. Rigaut and E. Gendron, *aap* **261**, 677 (1992).
- [46] J. Benedict, Rittig, J. B. Breckinridge, and D. L. Fried, *Journal of the Optical Society of America A* **11**, 257 (1994).
- [47] R. Foy and A. Labeyrie, *aap* **152**, L29 (1985).
- [48] L. A. Thompson and C. S. Gardner, in *Active telescope systems*, Society of Photo-Optical Instrumentation Engineers (SPIE) Conference Series, Vol. 1114, edited by F. J. Roddier (1989) pp. 184–190.
- [49] W. Happer, G. J. MacDonald, C. E. Max, and F. J. Dyson, *Journal of the Optical Society of America A* **11**, 263 (1994).
- [50] D. Steck, *Sodium D Line Data* (2003).

- [51] C. S. Gardner, D. G. Voelz, J. Sechrist, C. F., and A. C. Segal, *jgr* **91**, 13659 (1986).
- [52] C. S. Gardner, B. M. Welsh, and L. A. Thompson, *IEEE Proceedings* **78**, 1721 (1990).
- [53] T. Pfrommer and P. Hickson, *aap* **565**, A102 (2014).
- [54] V. Viotto, E. Portaluri, C. Arcidiacono, R. Ragazzoni, M. Bergomi, S. Di Filippo, M. Dima, J. Farinato, D. Greggio, D. Magrin, and L. Marafatto, in *Adaptive Optics Systems VI*, Society of Photo-Optical Instrumentation Engineers (SPIE) Conference Series, Vol. 10703, edited by L. M. Close, L. Schreiber, and D. Schmidt (2018) p. 107030V.
- [55] L. Schreiber, E. Diolaiti, C. Arcidiacono, T. Pfrommer, R. Holzlohner, M. Lombini, and P. Hickson, in *Adaptive Optics Systems IV*, Vol. 9148, edited by E. Marchetti, L. M. Close, and J.-P. Véran, International Society for Optics and Photonics (SPIE, 2014) p. 91486Q.
- [56] L. Schreiber, M. Lombini, I. Foppiani, E. Diolaiti, J.-M. Conan, and E. Marchetti, in *Adaptive Optics Systems*, Society of Photo-Optical Instrumentation Engineers (SPIE) Conference Series, Vol. 7015, edited by N. Hubin, C. E. Max, and P. L. Wizinowich (2008) p. 70151O.
- [57] Bardou, Lisa, Gendron, Éric, Rousset, Gérard, Gratadour, Damien, Basden, Alastair, Bonaccini Calia, Domenico, Buey, Tristant, Centrone, Mauro, Chemla, Fanny, Gach, Jean-Luc, Geng, Deli, Hubert, Zoltán, Laidlaw, Douglas J., Morris, Timothy J., Myers, Richard M., Osborn, James, Reeves, Andrew P., Townson, Matthew J., and Vidal, Fabrice, *A&A* **649**, A158 (2021).
- [58] J. M. Beckers, in *Very Large Telescopes and their Instrumentation, Vol. 2*, European Southern Observatory Conference and Workshop Proceedings, Vol. 30 (1988) p. 693.
- [59] F. Rigaut, in *European Southern Observatory Conference and Workshop Proceedings*, European Southern Observatory Conference and Workshop Proceedings, Vol. 58 (2002) p. 11.
- [60] E. Marchetti, R. Brast, B. Delabre, R. Donaldson, E. Fedrigo, C. Frank, N. Hubin, J. Kolb, M. L. Louarn, J.-L. Lizon, S. Oberti, R. Reiss, C. Soenke, S. Tordo, A. Baruffolo, P. Bagnara, A. Amorim, and J. Lima, in *Adaptive Optics: Analysis and Methods/Computational Optical Sensing and Imaging/Information Photonics/Signal Recovery and Synthesis Topical Meetings on CD-ROM* (Optica Publishing Group, 2007) p. AMA2.
- [61] B. Neichel, F. Vidal, F. Rigaut, E. Rodrigo Carrasco, G. Arriagada, A. Serio, P. Pessev, C. Winge, M. van Dam, V. Garrel, C. Araujo, M. Boccas, V. Fesquet, R. Galvez, G. Gausachs, J. Luhrs, V. Montes, C. Moreno, W. Rambold, C. Trujillo, C. Urrutia, and T. Vucina, *arXiv e-prints*, arXiv:1401.2009 (2014), arXiv:1401.2009 [astro-ph.IM]
- [62] T. Scheimpflug, "Improved method and apparatus for the systematic alteration or distortion of plane pictures and images by means of lenses and mirrors for photography and for other purposes," (1904), gB Patent No.1196, US Patent No. 751,347.

- [63] J. Carpentier, ““improvements in enlarging or like cameras,” (1901), gB Patent No.1139.
- [64] R. Ragazzoni, V. Viotto, E. Portaluri, M. Bergomi, D. Greggio, S. Di Filippo, K. Radhakrishnan, G. Umbriaco, M. Dima, D. Magrin, J. Farinato, L. Marafatto, C. Arcidiacono, and F. Biondi, [arXiv e-prints](#) , [arXiv:2012.07560](#) (2020), [arXiv:2012.07560 \[astro-ph.IM\]](#) .
- [65] P. Wizinowich, [Publications of the Astronomical Society of the Pacific](#) **125**, 798 (2013).
- [66] M. E. Kasper, J. Charton, B. Delabre, R. Donaldson, E. Fedrigo, G. Hess, N. N. Hubin, J.-L. Lizon, M. Nylund, C. Soenke, and G. Zins, in [Advancements in Adaptive Optics](#), Society of Photo-Optical Instrumentation Engineers (SPIE) Conference Series, Vol. 5490, edited by D. Bonaccini Calia, B. L. Ellerbroek, and R. Ragazzoni (2004) pp. 1071–1078.
- [67] F. Eisenhauer, R. Abuter, K. Bickert, F. Biancat-Marchet, H. Bonnet, J. Brynnel, R. D. Conzelmann, B. Delabre, R. Donaldson, J. Farinato, E. Fedrigo, R. Genzel, N. N. Hubin, C. Iserlohe, M. E. Kasper, M. Kissler-Patig, G. J. Monnet, C. Roehrl, J. Schreiber, S. Stroebele, M. Tecza, N. A. Thatte, and H. Weisz, in [Instrument Design and Performance for Optical/Infrared Ground-based Telescopes](#), Society of Photo-Optical Instrumentation Engineers (SPIE) Conference Series, Vol. 4841, edited by M. Iye and A. F. M. Moorwood (2003) pp. 1548–1561, [arXiv:astro-ph/0306191 \[astro-ph\]](#) .
- [68] Y. Clénet, P. Baudoz, R. Davies, E. Tolstoy, and K. Leschinski, in [SF2A 2019 conference](#), Proceedings of SF2A 2019 conference (Nice, France, 2019).
- [69] C. Arcidiacono, E. Portaluri, M. Gullieuszik, M. Cantiello, F. Annibali, P. Ciliegi, G. Agapito, C. Plantet, and L. Busoni, in [Adaptive Optics Systems VIII](#), Vol. 12185, edited by L. Schreiber, D. Schmidt, and E. Vernet, International Society for Optics and Photonics (SPIE, 2022) p. 121855P.
- [70] L. Busoni, G. Agapito, C. Plantet, G. Carlà, S. Oberti, M. Bonaglia, T. Lapucci, M. Xompero, C. Arcidiacono, Z. Hubert, P. Rabou, B. Salasnich, A. Baruffolo, I. Foppiani, G. Pariani, M. Munari, D. Magrin, M. Riva, and P. Ciliegi, in [Adaptive Optics Systems VIII](#), Society of Photo-Optical Instrumentation Engineers (SPIE) Conference Series, Vol. 12185, edited by L. Schreiber, D. Schmidt, and E. Vernet (2022) p. 121854R.
- [71] S. Ramsay, P. Amico, N. Bezawada, F. Biancat Marchet, P. Caillier, M. Cirasuolo, R. Conzelmann, R. Dorn, S. Egner, C. Frank, E. George, F. Gonte, J. C. González Herrera, P. Hammersley, C. Haupt, D. Ives, G. Jakob, F. Kerber, B. Koehler, S. Oberti, C. Schmid, J. Schimpelsberger, U. Seemann, R. Siebenmorgen, R. Tamai, and J. Vernet, in [Ground-based and Airborne Instrumentation for Astronomy VIII](#), Society of Photo-Optical Instrumentation Engineers (SPIE) Conference Series, Vol. 11447, edited by C. J. Evans, J. J. Bryant, and K. Motohara (2020) p. 114471U.
- [72] A. Costille, A. Bonnefoi, E. Renault, W. Ceria, K. Dohlen, B. Neichel, Z. Hubert, J.-J. Correia, T. Moulin, S. M. Mendoza, T. Fusco, P. Vola, F. Pedreros, P. Jouve, K. El Hadi, S. Barboza, R. Rohloff, F. Müller, F. Clarke, H. Schnetler, D. Melotte,

- and N. Thatte, in *SPIE Astronomical Telescopes + Instrumentation 2022* (Montréal, Canada, 2022).
- [73] P. Jouve, F. P. Bustos, A. Costille, B. Neichel, T. Fusco, and K. Dohlen, in *Adaptive Optics Systems VIII*, Vol. 12185, edited by L. Schreiber, D. Schmidt, and E. Vernet, International Society for Optics and Photonics (SPIE, 2022) p. 121854M.
- [74] N. A. Thatte, D. Melotte, B. Neichel, D. Le Mignant, I. Bryson, F. Clarke, V. Ferraro-Wood, T. Fusco, O. Gonzalez, H. Schnetler, M. Tecza, S. Wilson, A. Álvarez Urueña, H. A. Vilaseca, S. Arribas, G. J. Carracedo Carballale, A. Crespo, A. Estrada Piqueras, M. García García, C. Martínez Martín, M. Pereira Santaella, *et al.*, in *Ground-based and Airborne Instrumentation for Astronomy IX*, Society of Photo-Optical Instrumentation Engineers (SPIE) Conference Series, Vol. 12184, edited by C. J. Evans, J. J. Bryant, and K. Motohara (2022) p. 1218420.
- [75] S. Ramsay, P. Amico, N. Bezawada, M. Cirasuolo, F. Derie, S. Egner, E. George, F. Gonté, J. C. González Herrera, P. Hammersley, C. Haupt, J. Heijmans, D. Ives, G. Jakob, F. Kerber, B. Koehler, V. Mainieri, A. Manescau, S. Oberti, P. Padovani, C. Peroux, R. Siebenmorgen, R. Tamai, and J. Vernet, in *Advances in Optical Astronomical Instrumentation 2019*, Society of Photo-Optical Instrumentation Engineers (SPIE) Conference Series, Vol. 11203, edited by S. C. Ellis and C. d’Orgeville (2020) p. 1120303.
- [76] T. Bertram, O. Absil, P. Bizenberger, W. Brandner, F. Briegel, F. Cantalloube, B. Carlomagno, M. C. Cárdenas Vázquez, M. Feldt, A. M. Glauser, T. Henning, S. Hippler, A. Huber, N. Hurtado, M. A. Kenworthy, M. Kulas, L. Mohr, V. Naranjo, P. Neureuther, A. Obereder, R.-R. Rohloff, S. Scheithauer, I. Shatokhina, R. Stuik, and R. van Boekel, in *Adaptive Optics Systems VI*, Society of Photo-Optical Instrumentation Engineers (SPIE) Conference Series, Vol. 10703, edited by L. M. Close, L. Schreiber, and D. Schmidt (2018) p. 1070314.
- [77] B. Brandl, F. Bettonvil, R. van Boekel, A. Glauser, S. Quanz, O. Absil, A. Amorim, M. Feldt, P. Ho, M. Meyer, and More Authors, *The Messenger* **182**, 22 (2021).
- [78] C. Plantet, B. Neichel, G. Agapito, L. Busoni, C. M. Correia, T. Fusco, M. Bonaglia, and S. Esposito, *Journal of Astronomical Telescopes, Instruments, and Systems* **8**, 021509 (2022).
- [79] F. Vidal, M. Rozel, V. Deo, F. Ferreira, A. Sevin, E. Gendron, Y. Clénet, D. Gratadour, G. Rousset, and R. Davies, in *Proceedings of the AO4ELT6 conference* (2019) pp. 401–PG7Z–251.
- [80] Y. Clénet, T. Buey, E. Gendron, S. Karkar, F. Vidal, M. Cohen, F. Chapron, A. Sevin, S. Thijs, S. Taburet, B. Borgo, J.-M. Huet, A. Blin, O. Dupuis, J. Gaudemard, F. Ferreira, J. Raffard, F. Chemla, V. Lapeyrère, V. Deo, A. Bertrou-Cantou, N. Galland, S. Guieu, E. Meyer, *et al.*, in *Adaptive Optics Systems VIII*, Vol. 12185, edited by L. Schreiber, D. Schmidt, and E. Vernet, International Society for Optics and Photonics (SPIE, 2022) p. 121854S.
- [81] A. Costille, A. Bonnefoi, E. Renault, W. Ceria, K. Dohlen, B. Neichel, Z. Hubert, J.-J. Correia, T. Moulin, S. M. Mendoza, T. Fusco, P. Vola, F. Pedreros, P. Jouve,

- K. El Hadi, S. Barboza, R. Rohloff, F. Müller, F. Clarke, H. Schnetler, D. Melotte, and N. Thatte, in *SPIE Astronomical Telescopes + Instrumentation 2022* (Montréal, Canada, 2022).
- [82] T. Fusco, G. Agapito, B. Neichel, S. Oberti, C. M. Correia, P. Haguenuer, C. Plantet, F. P. Bustos, Z. Ke, A. Costille, P. Jouve, L. Busoni, and S. Esposito, *Journal of Astronomical Telescopes, Instruments, and Systems* **8**, 021514 (2022).
- [83] G. Fiorentino, M. Bellazzini, P. Ciliegi, G. Chauvin, S. Douté, V. D’Orazi, E. Maiorano, F. Mannucci, M. Mapelli, L. Podio, P. Saracco, and M. Spavone, “Maory science cases white book,” (2019), [arXiv:1712.04222 \[astro-ph.IM\]](https://arxiv.org/abs/1712.04222) .
- [84] K. Grisdale, N. Thatte, J. Devriendt, M. Pereira-Santaella, A. Slyz, T. Kimm, Y. Dubois, and S. K. Yi, *Monthly Notices of the Royal Astronomical Society* **501**, 5517 (2021).
- [85] G. Fiorentino, M. Bellazzini, M. Spera, N. B. Sabha, M. Mapelli, L. Schreiber, M. Dall’Ora, L. Inno, M. Patti, V. F. Braga, M. Lombini, E. Diolaiti, F. Cortecchia, C. Arcidiacono, C. Plantet, and G. Agapito, *Monthly Notices of the Royal Astronomical Society* **494**, 4413 (2020), <https://academic.oup.com/mnras/article-pdf/494/3/4413/33156133/staa869.pdf> .
- [86] P. Madau and M. Dickinson, *Annual Review of Astronomy and Astrophysics* **52**, 415 (2014).
- [87] A. Zanella, E. L. Floc’h, C. M. Harrison, E. Daddi, E. Bernhard, R. Gobat, V. Strazzullo, F. Valentino, A. Cibinel, J. S. Almeida, M. Kohandel, J. Fensch, M. Behrendt, A. Burkert, M. Onodera, F. Bournaud, and J. Scholtz, *Monthly Notices of the Royal Astronomical Society* **489**, 2792 (2019).
- [88] S. Di Filippo, D. Greggio, M. Bergomi, K. Kumar Radhakrishnan Santhakumari, E. Portaluri, C. Arcidiacono, V. Viotto, R. Ragazzoni, M. Dima, L. Marafatto, J. Farinato, and D. Magrin, in *Adaptive Optics Systems VIII*, Society of Photo-Optical Instrumentation Engineers (SPIE) Conference Series, Vol. 12185, edited by L. Schreiber, D. Schmidt, and E. Vernet (2022) p. 121854V, [arXiv:2209.12921 \[astro-ph.IM\]](https://arxiv.org/abs/2209.12921) .
- [89] J. Canny, *IEEE Transactions on Pattern Analysis and Machine Intelligence* **PAMI-8**, 679 (1986).
- [90] Y. Xie and Q. Ji, *Object recognition supported by user interaction for service robots* **2**, 957 (2002).
- [91] S. van der Walt, J. L. Schönberger, J. Nunez-Iglesias, F. Boulogne, J. D. Warner, N. Yager, E. Gouillart, T. Yu, and the scikit-image contributors, *PeerJ* **2**, e453 (2014).
- [92] T. Pfrommer and P. Hickson, *J. Opt. Soc. Am. A* **27**, A97 (2010).
- [93] T. Pfrommer, P. Hickson, and C.-Y. She, *Geophysical Research Letters* **36** (2009), <https://doi.org/10.1029/2009GL038802>, <https://agupubs.onlinelibrary.wiley.com/doi/pdf/10.1029/2009GL038802> .

Appendix A

Sodium Layer Profiles

Authentic profiles were obtained at the 6 metre Large Zenith Telescope in Canada [92] using LIDAR technology [93]. With the high resolution LIDAR system installed at the Large Zenith Telescope, several sodium profiles were obtained after careful data treatment and analysis.

The data set comprises a total of 16 cases, obtained throughout the month of July 2010, with each case consisting of 30 profiles. These profiles are the result of 10-second time integrations and offer a vertical resolution of 126.5 metres. The data set encompasses 198 height levels, starting from the lowest altitude bin of 80 km.

These are covering some of the usual profiles which are usually classified as: gaussian, single top-hat, double layer of top-hat shape, etc; and some unusual ones too (strong wavy pattern in the vertical distribution, existence of a secondary sodium layer at higher altitude than the usual peak in the mesosphere, as well as a narrow single-peak case, etc). Figures A.1, A.2 and A.3 are three of these cases (showing three 10-second time integration profiles superimposed), each drawn from separate nights.

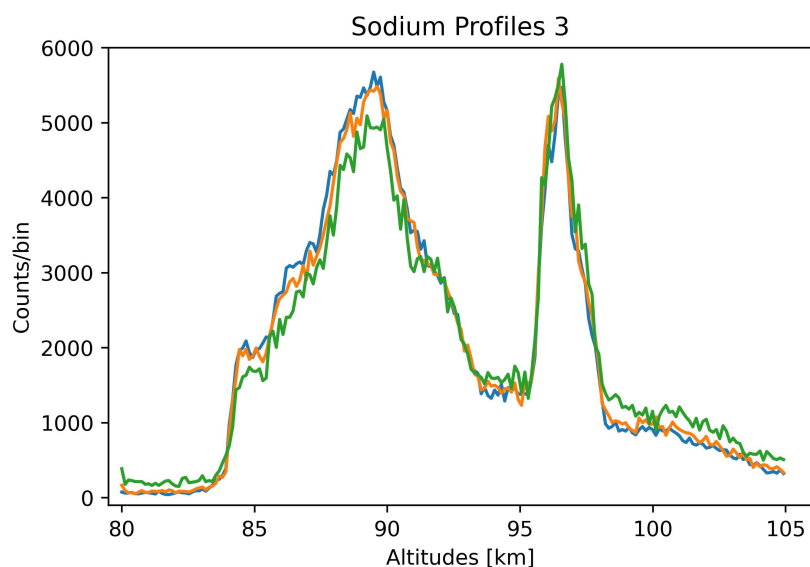


Figure A.1: Taken on 28 July 2010 and identified as an unusual shape, this profile shows a secondary sodium layer (relatively strong). The y axis shows the photon counts per altitude bin (with 126.5 metres width) at median altitude (in km) represented on the x axis.

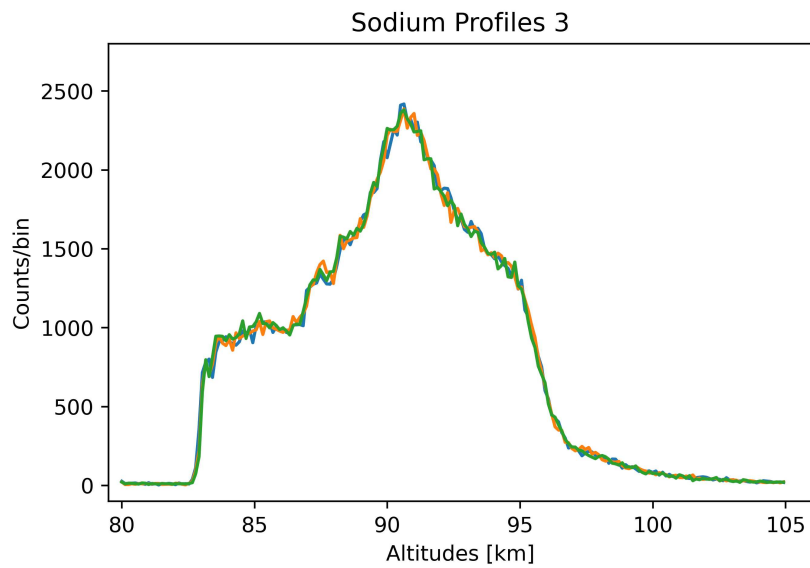


Figure A.2: Taken on 16 July 2010, this profile was described as having a narrow peak on the upper half and a top hat on the lower. The y axis shows the photon counts per altitude bin (with 126.5 metres width) at median altitude (in km) represented on the x axis.

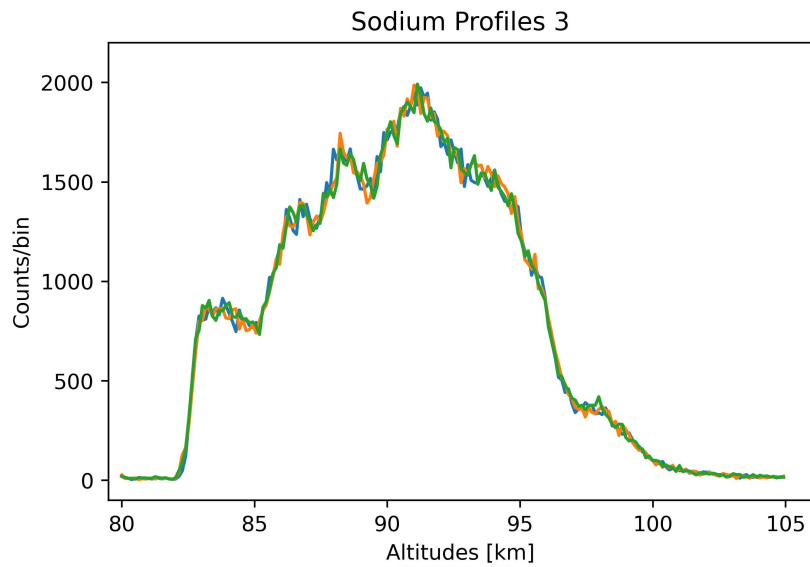


Figure A.3: Taken on 16 July 2010, this profile was classified as a typical wavy pattern. The y axis shows the photon counts per altitude bin (with 126.5 metres width) at median altitude (in km) represented on the x axis.

